GEOMETRIC AND ELECTROCHEMICAL CHARACTERISTICS OF LITHIUM ION BATTERIES

A Thesis

Submitted to the Faculty

of

Purdue University

by

Huixiao Kang

In Partial Fulfillment of the

Requirements for the Degree

of

Master of Science in Mechanical Engineering

May 2017

Purdue University

Indianapolis, Indiana

THE PURDUE UNIVERSITY GRADUATE SCHOOL
STATEMENT OF THESIS APPROVAL

Dr. Likun Zhu, Chair

Department of Mechanical Engineering

Dr. Jing Zhang

Department of Mechanical Engineering

Dr. Yongzhu Fu

Department of Mechanical Engineering

Approved by:

Dr. Jie Chen

Head of the Departmental Graduate Program

For
my parents
and
husband

ACKNOWLEDGMENTS

This work was supported by the US National Science Foundation under Grant No. 1335850 and used resources of the Advanced Photon Source, a U.S. Department of Energy (DOE) Office of Science User Facility operated for the DOE Office of Science by Argonne National Laboratory under Contract No. DE-AC02-06CH11357.

I would like to show my great gratitude to my academic advisor Dr. Likun Zhu for guiding and supporting me in my Master's degree program. Your rigorous attitude towards science and sincere help to students will benefit me for the rest of my life. I would also like to thank Dr. Yongzhu Fu, his courses led me into lithium ion battery area and you spare no effort to help me with problems. Also, my sincerely acknowledgements are given to Cheolwoong Lim, a big brother. All my research is following his previous work and he never hesitated to teach me experiments and image processing skills.

I thank Dr. Bo Yan for providing 3D geometry analysis code and Tianyi Li for calculating particle size distribution.I would also like to show my gratitude to Dr. Yadong Liu, Yi Cui, Min Wu, Armuth Bhargav for sharing their pearls of wisdom with me during the course of this research. I thank David Briel for helping me with software and computer issues. I'm also immensely grateful to three anonymous reviewers for their comments on an earlier version of the NMC paper manuscript.

In addition, I would like to thank my thesis committee members Dr. Likun Zhu,Dr. Jing Zhang and Dr. Yongzhu Fu for their time and participation in my thesis defense. Their advice and comments have further enriched the quality of this thesis.

Finally, I extend my thanks to Mr. Jerry Mooney for assisting me in formating my thesis. I'd also like to stretch my heart fully to thank my family and my friends, it's your love and care supporting me in this journey.

TABLE OF CONTENTS

Page

LIST OF TABLES

LIST OF FIGURES

NOMENCLATURE

LIB	Lithium ion battery
NMC	$LiNi_{1/3}Mn_{1/3}Co_{1/3}O_2$
C/carbon	Super-P carbon black (C65, TIMCAL Ltd.)
PVDF	Polyvinylidene difluoride (KF 1120 polymer 12 wt.% PVDF)
NMP	N-methyl-2-pyrrolidinone solvent (NMP, anhydrous 99.5%)
Electrolyte	EC/DEC Electrolyte containing 1M $LiPF_6$ in a 1:1 volume-ratio mixture of ethylene carbonate and dimethyl carbonate
EV	Electric Vehicle
HEV	Hybrid Electrical Vehicle
PHEV	Plug-in Hybrid Electric Vehicle
NREL	National Renewable Energy Laboratory
SHE	Standard Hydrogen Electrode
FIB-SEM	Focused ion beam scanning electron microscope
TXM	Transmission X-ray microscopy
APS	Advanced Photon Source
ANL	Argonne National Laboratory
EIS	Electrochemical impedance spectroscopy
SPEs	Solid polymer electrolytes
EIS	lithium salt
LiX	Solid polymer electrolytes
PAN	Polyacrylonitrile
PEO	Polyethylene oxide
PVC	Poly(vinyl chloride)
PMMA	poly(methyl methacrylate)

PPO	Poly(phenylene oxide)
PEG	Polyethylene glycol
PVC	Poly(vinyl chloride)
LTAP	$Li_{1.3}Ti_{1.7}Al_{0.3}(PO_4)_3$ as Li-ion conductor

ABSTRACT

Kang, Huixiao M.S., Purdue University, May 2017. Geometric and Electrochemical Characteristics of Lithium Ion Batteries. Major Professor: Likun Zhu.

The geometric and electrochemical characteristics of different lithium ion batteries (LIBs) are investigated in this study. The core work is to study the impact of the calendering process on NMC cathode electrodes performance. X-ray CT image processing by Python, MATLAB, ImageJ and Avizo is utilized in this study.

NMC electrodes with different calendering conditions were fabricated to calculate electrochemical properties of the cells. Charge/discharge of the electrodes under 0.1C, 0.2C, 0.4C, 1C, 2C, 4C and 0.1C (retention test) rates were cycled for three times respectively between 4.2 V and 3.0 V. Electrochemical impedance spectroscopy testing was used to further explain the effects of NMC density on rate capability.

Geometric properties of NMC electrodes with different calendering conditions were calculated from the computed tomography data of the electrodes. A synchrotron transmission X-ray microscopy tomography system at the Advanced Photon Source of the Argonne National Laboratory was employed to obtain the tomography data. X-ray CT image processing before the data analysis was introduced. Python based Tomopy and ASTRA toolbox were used to filter the original HDF5 data and reconstruction. ImageJ was used to help remove noise, adjust contrast and cropping. Iso2mesh and image processing tool box were used in MATLAB to generate meshed 3D structure of CT data.

Geometric properties of NMC electrodes including porosity, pore size distribution, particle size distribution, specific surface area and tortuosity were calculated from the computed tomography data of the electrodes.The geometric and electrochemical analysis show that calendering can increase the electrochemically active area, which

lead to improving of the rate capability. However, more calendering will result in crushing of NMC particles, which can reduce the electrode capacity at relatively high C rates. This study shows that the optimum electrochemical performance of NMC electrode at 94:3:3 weight ratio of NMC:binder:carbon black can be achieved by calendering to 3.0 g/cm^3 NMC density.

LTAP solid electrolyte and NMC cathode material mix electrode-electrolyte X-ray CT data was studied in last chapter.By using 8 kev X-ray energy, we could distinguish NMC active material, LTAP solid electrolyte and the others three phase. On the basis of NMC electrode image processing method, dilation and multiply threshold method is applied to get three-phase 3D geometry. A comparing of connection area between NMC and LTAP of 700psi and 1300psi electrode was analyzed. Geometric properties like tortuosity, diffusion length and effective diffusivity were generated from the CT data.

1. INTRODUCTION

1.1 LIB Implication

Environmental problems caused by noise, emissions, and the limits of primary energy sources like crude oil, force us to develop and test new energy. The automobile industry has become one of the main areas directly facing this problem. Therefore, multiple tests of these new technologies are implemented and accomplished in several researching institutions all over the world.

In the past thirty years, consumer application of LIBs are dramatically increased and LIBs have been used in the automobile industries. The rapid development of Electric Vehicle (EV), Hybrid Electrical Vehicle (HEV) and Plug-in Hybrid Electric Vehicle (PHEV) requires high energy and power density batteries. As shown in figure 1.1, one report from the National Renewable Energy Laboratory (NREL) estimates the global demand for all types of EVs for LIBs is approximately 18 GWh in 2016. However,the demand will increase to 53Gwh in 2020. There is a huge market vacancy in the near future.

LIBs have become the main power source for EVs profiting by their numerous of beneficial properties and characteristics such as high energy density, good specific energy and long cycle life. Nowadays, lots of research efforts have been made towards the development of new generation of LIBs to improve their performance.

1.2 LIB Theory

Through electrochemical oxidation-reduction (redox) reaction, a battery converts the chemical energy contained in its active materials into electric energy. For a rechargeable battery, the electrochemical reaction could be reversed by the recharging

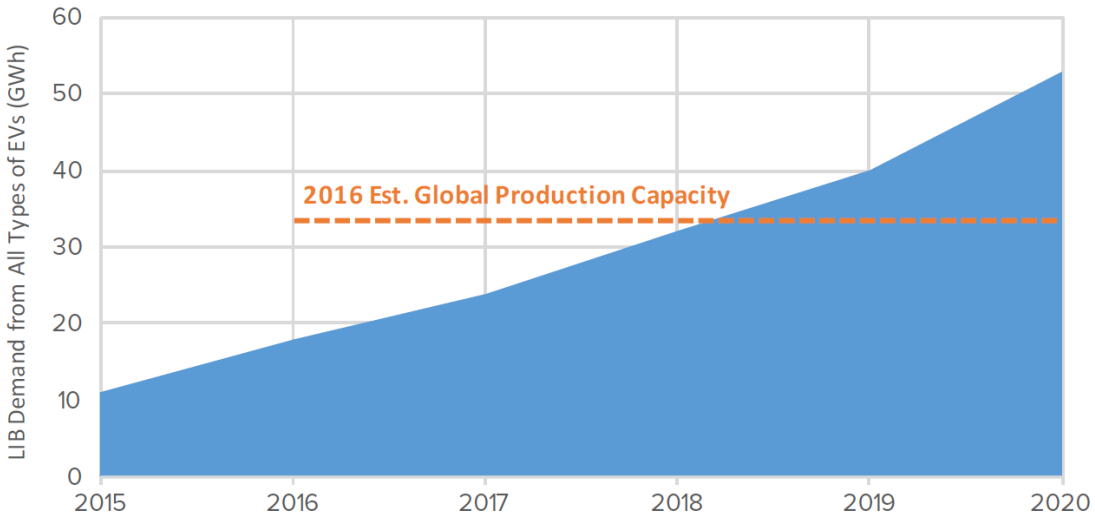

Fig. 1.1. Comparison of estimated LIB demand for EVs between 2015 and 2020 and estimated production capacity in 2016.

process. The charging and discharging process involves the transfer of electrons and ions from one material to another material through an electric circuit. Different from the battery, non-electrochemical redox reaction occurred during rusting and burning, which transferred chemical energy into heat. According to the Carnot cycle, combustion or heat engines have a limitation of energy convert efficiency dictated by the second law of thermodynamics. However, the battery has the capable of having higher energy conversion efficiency which made it an ideal energy storage device. A basic unit of the battery is a cell. A battery is combined with one or more cells connecting in parallel or series, or both to meet different requirements. In general, a cell has three major components: cathode, anode, and electrolyte. A brief explanation of these three parts is as following.

1.2.1 Cathode

The cathode, also known as a positive electrode, shown as " +" on batteries. It works as an oxidizing electrode, accepts electrons from the external circuit, and is reduced in the discharge process. When charging, it works as a reducing electrode, gives electrons to the external circuit, and is oxidized. Theoretically, the stronger oxidizing agent correspond to the higher standard electrode potential. The bigger of the standard electrode potential difference between the electrode and a reference electrode (or anode), the higher theory cell voltage, which may lead to a higher energy density.

The Standard Hydrogen Electrode (SHE) consists of a platinum electrode in a 1 M H^+(aq) solution at 25C, through which H_2(g) at 1 atm is bubbled:

$$H_2(g, 1atm) \rightarrow 2H^+(aq, 1M) + 2e^- \quad E = 0V$$

$$2H^+(aq, 1M) + 2e^- \rightarrow H^2(g, 1atm) \quad E = 0V$$

The following are three sample cathode half reactions with standard reduction potential compared with SHE:

$$F_2(g) + 2e^- \rightarrow 2F^-(aq) \quad E^o(V) = 2.87$$

$$MnO_4^-(aq) + 4H^+(aq) + 3e^- \rightarrow MnO_2(s) + 3H_2O(l) \quad E^o(V) = 1.68$$

$$Cr_2O_7^{2-}(aq) + 4H^+(aq) + 6e^- \rightarrow 2Cr^{3+} + 7H_2O(l) \quad E^o(V) = 1.33$$

1.2.2 Anode

Anode, also known as a negative electrode, shown as " -" on batteries. It works as a reducing electrode, gives electrons to the external circuit, and is oxidized in the discharge process. When charging, it works as an oxidizing electrode, accepts electrons from the external circuit, and is reduced. By using the standard reduction potential of cathode minus the standard reduction potential of the anode, we could

easily estimate the cell voltage. The choosing of the anode and the cathode is a pair. The following are three sample cathode half reactions with SHE:

$$Li^{+}(aq) + e^{-} \rightarrow Li(s) \quad E^{o}(V) = -3.04$$

$$Mn^{2-}(aq) + 2e^{-} \rightarrow 2Mn(s) \quad E^{o}(V) = -1.18$$

$$Ni^{2-}(aq) + 2e^{-} \rightarrow 2Ni(s) \quad E^{o}(V) = -0.23$$

1.2.3 Electrolyte

The electrolyte is working as ionic conductor, which provides the medium for transfer of charge as ions inside the cell between the anode and cathode [1].The electrolyte could be either liquid or solid. Liquid electrolyte could be water, or other solvents with dissolved salts, acids or alkalis, it helps improve ionic conductivity of the battery.

The physical location of the electrolyte is between cathode and anode electrodes, so it has close interaction with both electrodes and needs to be changed based on the usage of positive and negative electrodes. The interfaces connection between electrolyte and electrodes have a significant influence on the battery performance, which makes the choosing of the electrolyte is very important.

1.2.4 LIB Working Principle

LIB belongs to the big family of rechargeable batteries. Rechargeable battery, also known as secondary battery, means that the battery could be reused after recharging. Same as all kinds of batteries, lithium positive ions move from the negative electrode to the positive electrode through electrodes and electrolyte during discharge. Meanwhile, electrons transfer from negative electrode to the positive electrode through conductive material and outside circuit passing the electric equipment. During charging, an external power is used to provide energy for the reversed electrochemical reaction,

which allows lithium ions to go back to the negative electrode through the inner battery and electrons to go back to the negative electrode through the outer circuit. The discharge of the battery is a spontaneous reaction that provides electric power, and the charging process of the battery is non-spontaneous reaction which requires external energy (which make the battery energy storage device). Figure 1.2 is a sketch map of LIB working principle [2], which clearly shows the electrons and ions transfer direction and path during the battery charging/discharging process.

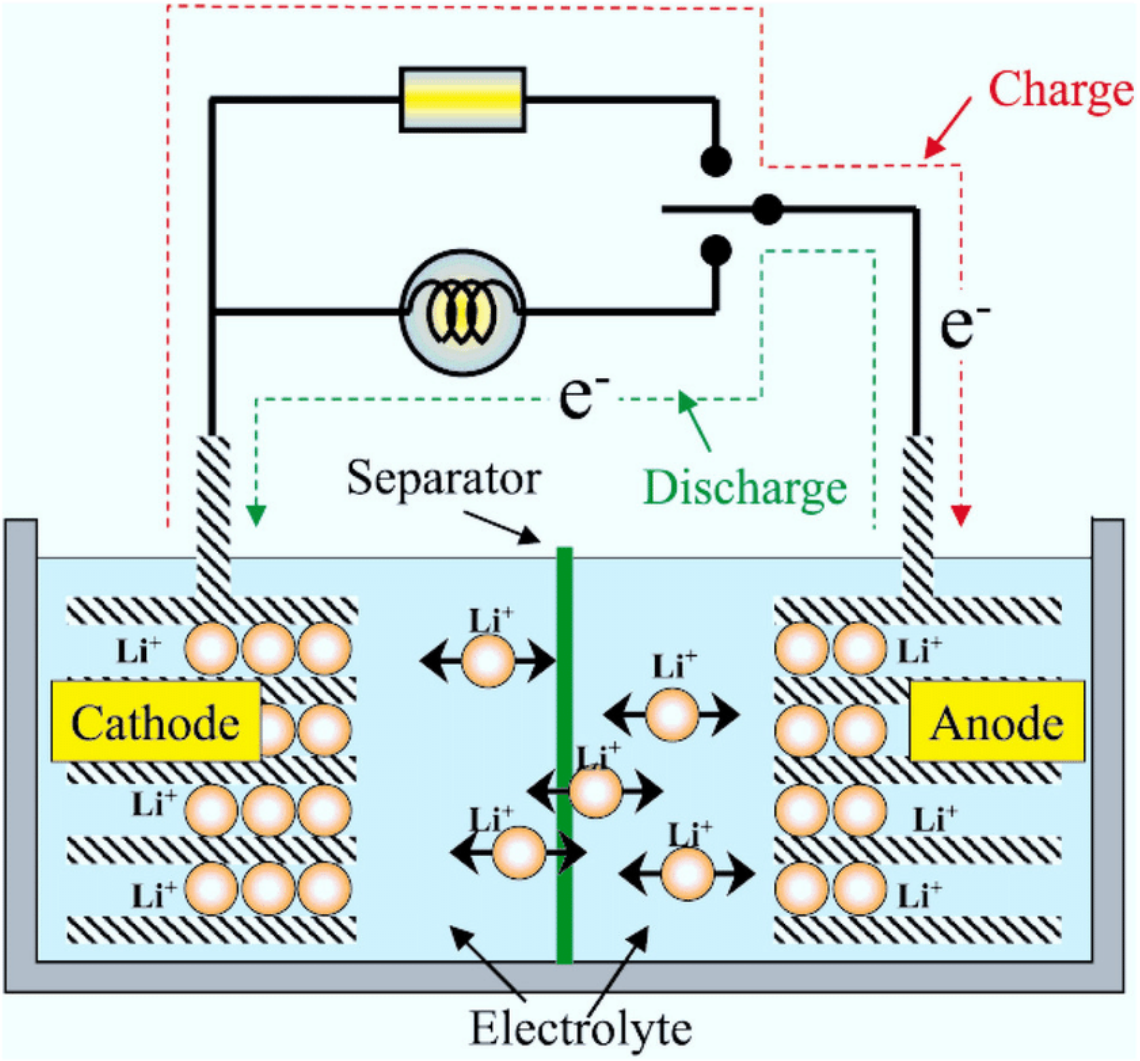

Fig. 1.2. LIB working principle [2].

The standard potential of a cell is one of the main characters of the cell which can calculate from the standard electrode potentials. As we mentioned before, we could calculate using the following equation: cathode (reduction potential) -Anode (oxidation potential) =standard cell potential. The potential value for cathode and anode should come from same reference standard, for example, SHE.

The theoretical capacity of a cell is also a requisite parameter on the battery label. It is determined by some active materials in the cell and expressed as the total quality of electricity involved in the electrochemical reaction. Capacity is defined by regarding coulombs or ampere-hours. Theoretically, one gram-equivalent weight of material will deliver 96,487C or 26.8Ah. (A gram-equivalent weight is the atomic or molecular weight of the active material in grams divided by the number of electrons involved in the reaction.) The theoretical capacity of an electrochemical cell, based only on the active materials participating in the electrochemical reaction is calculated from the equivalent weight of the reactants [1]. Hence, the theoretical capacity of the Zn/Cl_2 cell is 0.394Ah/g, that is,

$$Zn + Cl \rightarrow ZnCl_2$$

$$(0.82Ah/g) \qquad (0.76Ah/g)$$

$$1.22g/Ah + 1.32g/Ah = 2.54g/Ah \quad or \quad 0.394Ah/g$$

Theoretical energy value of a cell is the maximum energy value that can be delivered by a specific electrochemical system, which could calculate by the following equation:

$$Watthour(Wh) = voltage(V) * ampere - hour(Ah)$$

In a real cell, only a fraction of the theoretical energy is realized. That is because in order to make a cell, electrolyte, separator, binder and other nonreactive components are added. And, when the battery is not discharged at the theory voltage or current, energy is not fully used. Whats more, the active material in the cell may not fully react due to the unavailable manufacture inhomogeneous and side reaction.

1.3 Research Field

As described in the previous section, anode, cathode, and electrolyte are three main components of a cell. It is no doubt that their electrochemical properties become the primary research mission.

One aspect is to focus on the "source" , which includes finding new materials and making full use of the known potential material. For example, GeSe and Tin are known as the potential materials of anode and the main challenges of these materials are their volume expanding and shrinking during the charging and discharging process, which may cause a significant contact problem, decrease the cycle life and lower power density of the battery.

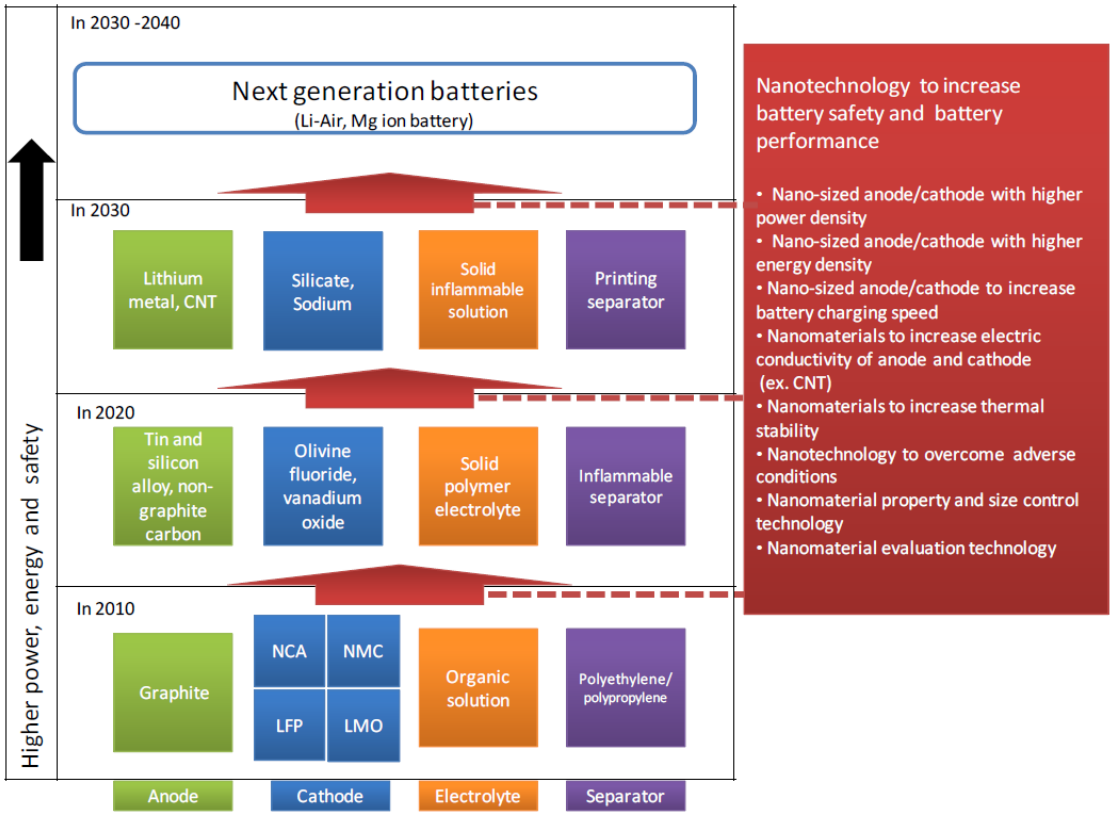

Fig. 1.3. LIB road map and nanotechnology.

Second aspect is to focus on the "process", which means to find a new method to optimize the electrochemical reaction process. With the growing of nanotechnology, multiple nanometer materials and nano-technologies are applied in LIB area. How to create and make full use of nano-size material has become one of the main research areas of LIB. Nanomaterials demonstrate different chemical and physical properties of micro-sized materials because of their significantly smaller particle size. The unique properties of nanomaterials offer significant potential to improve battery performance. Figure 1.3 shows a road map for battery technology which include the development of lithium-ion batteries from 2010 to 2030 and next-generation batteries emerging after 2030 [3]. The research of calandering NMC electrode performance in this paper is part of this area.

The third is "application". Nowadays, lithium ion batteries are widely used in our daily life but are not used in the aerospace field. The main reason is that LIBs have flammable characteristics, which means any accident leakage may cause a serious safety problem. To extend the application of LIBs into the aerospace field, safety need to be ensured. Hence, solid electrolyte research which could avoid liquid electric leaking has become another hot research area, which is also involved in the last chapter of this thesis.

2. $LINI_{1/3}MN_{1/3}CO_{1/3}O_2$ ELECTRODE ELECTROCHEMICAL CHARACTERISTICS STUDY

2.1 Preface

The microstructure of composite electrodes determined by the fabrication process also plays a critical role in determining of the performance of the LIB [4]. However, the impact of fabrication process on the performance of LIBs has not been widely explored [5]. In practice, many fabrication parameters are chosen based on experience rather than analysis and computation [5]. The fabrication of LIB electrode is a complex process involving many procedures, such as slurry preparation, coating, calendering, cell assembly, et al. All of the procedures could have significant impacts on the performance of a LIB. In this paper, we are going to focus on the impact of the calendering process.

Calendering is a process used in battery industry to adjust the porosity and thickness of electrodes, smooth the surface roughness, and enhance conductivity of the electrodes. To this end, some research works have been done to study the impact of calendering process on electrochemical properties of LIB electrodes [6–15]. For instance, Zheng et al. investigated calendering effects on the physical and electrochemical properties of NMC cathode [6,10]. They found that the matrix conductivity is closely associated with the fraction of inactive material and weakly associated with the degree of calendering. Marks et all. have reported that compression on low carbon content NMC electrodes could reduce the space between carbon chains and apparently increasing conductivity of the electrode [12].

However, there are few reports on the geometric characteristics and their impacts on the electrochemical performance of LIB electrodes with different calendering conditions,calindering condition have a significant influence to LIBs at the aspect

of inhomogeneity, complexity, and three-dimensional (3D) nature of the electrodes microstructure. In this chapter, the manufacturing of different calendering condition NMC electrodes and their electrochemical performance is introduced. The comparing of geometric characteristics and electrochemical performance of LIB battery by using NMC as cathode electrode will be illustrated in following chapter.

2.2 Cell Fabrication

2.2.1 Introduction

As mentioned in chapter 1.2, three electrochemical reaction material required in a battery are cathode, anode, and electrolyte. The material choosing of these three parts decide the theory energy density and capacity limitation of the battery. In the chapter, we are not focus on finding new material for better battery performance, but on improving the manufacturing method to make full use of the active material, to give a reference to the current commercial battery about calandering condition control. Therefore, the material choosing, coin cell manufacturing, and electrochemical testing are following the commercial manufacture process. We make the research electrodes that are as similar as possible to those found in the commercial cells in our research.

Besides cathode, anode, and electrolyte, several other materials are required for electrode making. To make full use of the electric energy, the current collecting foil is used at both anode and cathode to conduct electricity. Therefore, electrode materials should adhere well to the current collecting foil and each other to avoid particle connection problem during cycling.Particles losing connection are not participating in the electrochemical reaction, which will decrease the overall cell capacity. To meet this requirement, the binder material is needed to help connect the electrode materials and the current collecting foil. While the binder is non-conducting material, electron conductive material is also needed to help electrons transferring between the active material particles and the current collecting foil.

What's more, a cell holder is needed to getting all the materials together and to transfer electric energy for electric equipment. There are three types of basic cell: coin cell, punch cell, and cylinder cell.These cells and their manufacture sketch map are shown in figure2.1. Different cells are used in different condition.

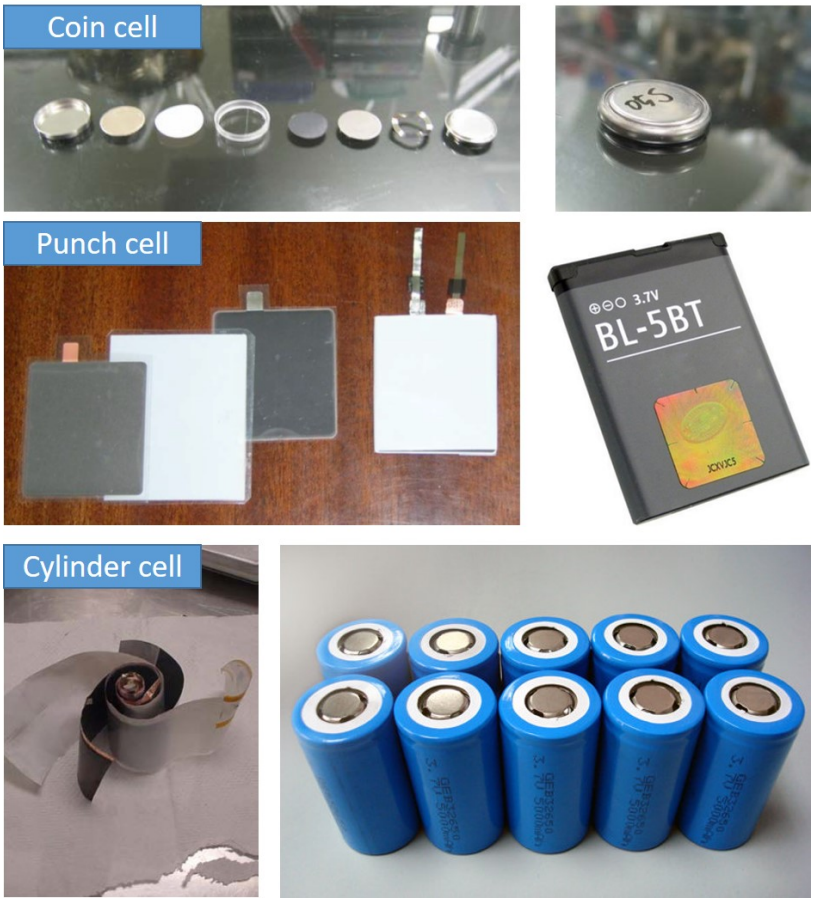

Fig. 2.1. Different cell type fabrication and application [16].

2.2.2 Material Selection

NMC is one of the most successful LIB cathode materials which is widely used in the battery market. It is widely accepted that NMC LIBs is promising for EVs Therefore, we choose NMC as the active material in this section. NMC active material we used is from Umicore, Brussels, Belgium. SEM image of NMC powder is shown

in Figure 2.2. The majority NMC particles size is 5-6um and the biggest particle size is around 10um. Most of them are not a sphere shape but close to a sphere. The sub-particles size of NMC particles are around 0.2-1um. Sub-particles have a relative smooth surface, while the NMC particles have relative rough surface. Super-P carbon black (C65, TIMCAL Ltd.) is used as ion conduct material in this research. It is from MTI, Richmond, CA.

Polyvinylidene difluoride (KF 1120 polymer 12wt.% PVDF) binding agent is from Kureha, New York, NY. N-methyl-2-pyrrolidone solvent (NMP, anhydrous 99.5%) is from Sigma-Aldrich, St. Louis, MO. NMP is used as the solvent of electrode slurry, which is usually working together with PVDF binder. EC/DEC Electrolyte containing 1M $LiPF_6$ in a 1:1 volume-ratio mixture of ethylene carbonate and dimethyl carbonate is received from BASF, Elyria, OH.

A thin aluminum foil which has a thickness of 17um is used as current collecting foil to coat the electrode slurry. Lithium foil is used as the anode (reference electrode) to provide enough Li ion for the battery reaction. The choosing of Lithium foil is because it helps to minimize the influence of anode to the cell electrochemical performance. Celgard 2400 separator is used between cathode and anode material. It allows permeating of electrolyte, which assured the transmission of Li ion during the reaction. And, it is isolator, which physically isolates cathode and anode. What's more, Celgard 2400 separator has good suppleness which allows it to overcome the high pressor during the cell assemble. Nicole form is used as filler at the anode side when assembling coin cell to ensure the connection between cell case and anode. Standard 2016 coin cell is used as the cell case.

2.2.3 Slurry Material Percentage

Electrodes should contain as much active material as possible to improve the active material per unit volume. To improve the electrode density, one way is to add less assist material like a binder and conductive material; another way is to compress

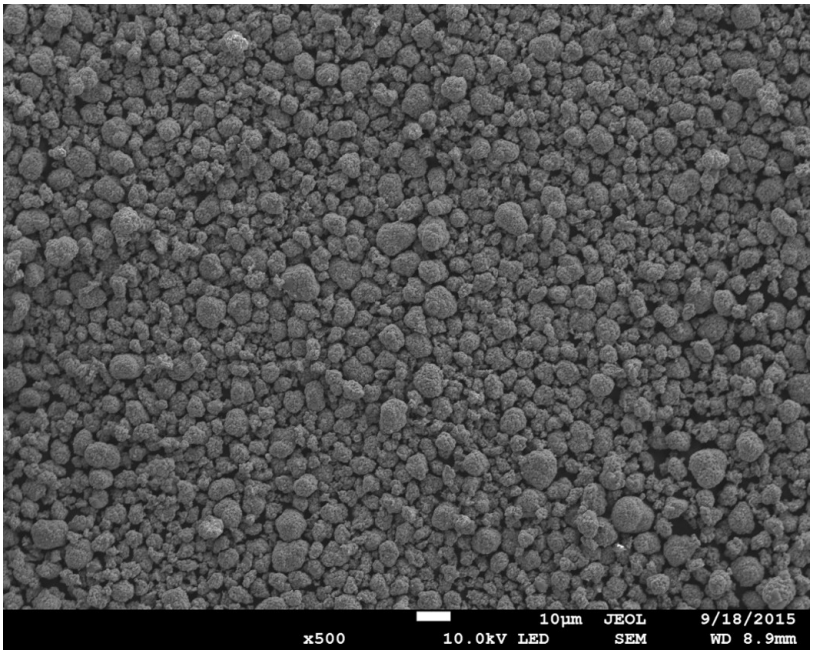

(a) Magnifying 500.

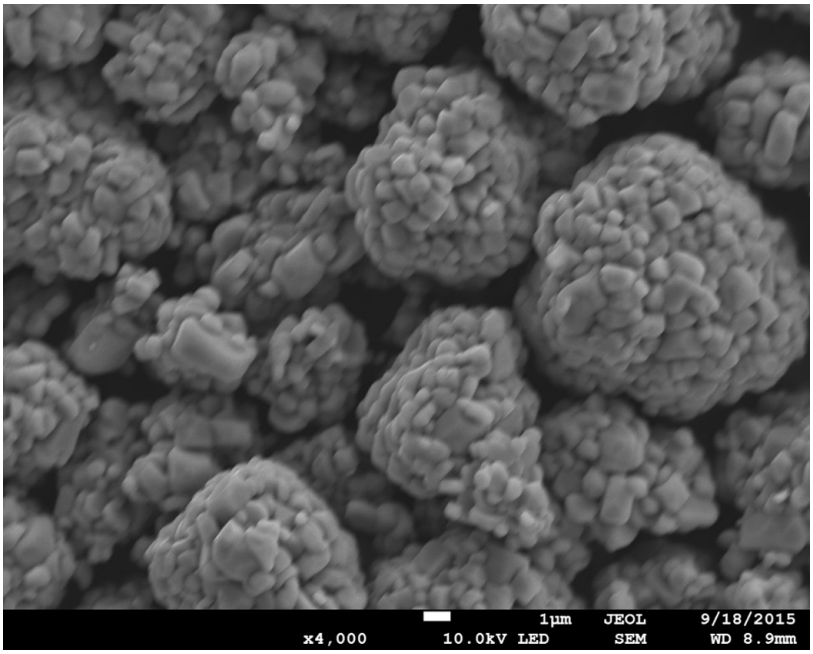

(b) Magnifying 4000.

Fig. 2.2. SEM image of NMC powder with magnifying 500 and 4000.

the electrode after the electrode is dried. These methods are widely known and used in industry. While in research, researchers normally use recipes from predecessors or spend time themselves to get a working recipe for their research. The recipe difference between industry and research cause an inescapable problem which is research could not meet the commercial requirement. That means a long improving process may required before the research result applying in industry. There are many different NMC electrode recipes presented inliteratures. Dr. Marks had made a brief summary of that and did depth analysis of different recipe to guide the NMC active material using percentage in research [12].

Table 2.1.
Some recipe that have been used to fabricate positive electrodes for LIBs as found in the indicated literature [12].

Active material	% active by mass	% binder by mass	% carbon black (and/or graphite) by mass	Compressed Yes/no
NMC	96	2	2	Yes
$Li_{\sim 1.1}Mn_{\sim 1.9}O_4$	~96	~2	~2	Yes
$LiMn_2O_4$	85	5	10 (graphite)	No
NMC	88	6	6	No
$Li_{1.04}Mn_{1.96}O_4$	75	5	20	Not clear
NMC	86	7	7	No
$LiCoO_2$	92	4	4	No
$LiMn_2O_4$	92	6	2	No
$LiCoO_2$	90	5	5	No
NMC	80	10	10	No
NMC	84	8	8 (4 carbon and 4 graphite)	Yes
NMC	76	12	12	No
NMC	82	7	11 (7 carbon and 4 graphite)	No
$LiCoO_2$	85	5	10	No
$LiCoO_2$	78	10	12 (6 carbon and 6 graphite)	No
$LiCoO_2$	75	5	20	No
$LiMn_2O_4$	70	5	25	No

Electron conductive material makes cathode/anode having a bigger surface area to contact with. A big surface area may increase parasitic reactions which occur at the connect surface of the electrolyte and conductive material. In addition, parasitic reactions may shorter the cycle life of the cell. On the other hand, if there is not

enough conductive material in electrode recipe, some part of the active material may have a bad electron conductive. This situation will lower the battery capacity, which should also avoid in industry. Whats more, in our research, low percentage of binder and carbon black in the electrode is mainly due to the requirement of the high capacity of LIB electrode and the invisibility of carbon and binder in synchrotron transmission X-ray microscopy (TXM) tomography [17]. To meet the requirements we mentioned above, we set the cathode recipe to be NMC:PVDF:C=94:3:3.

2.2.4 Electrode Making and Thickness Control

The commercial NMC particles usually have a spherical morphology with diameter around ten m and they are composed by sub-particles with size several hundred nanometers. Recently, multiple methods have been developed to tune the nano scale structure of sub-particles to improve the performance of NMC electrode. For instance, Li et al. designed a facile nanoetching-template synthesis route to assign a porous nanomicrohierarchical morphology for NMC particles [18]. Peng et al. reported novel nanoarchitectured NMC cathodes composed of self-assembled nanosheet structures synthesized via a facile hydrothermal method and a stepwise calcination process [18]. Due to the unique microstructure of NMC particles and the knowledge obtained from the previous studies [19–21], we hypothesize that the impact of calendering on NMC electrode is different from $LiCoO_2$ shown in ref [17]. Therefore, the purpose of this section is to manfacture NMC cathode electrode with different calendering conditions to change microstructure of electrode.

The active material and carbon black current conductor were ground by research for 20minutes. To make electrode slurry, the mix were added with a binder into NMP solution and mixed homogeneously by a magnetic stir bar in a vial for 20h. NMP solution amount is decided according to Dr. Markss Guide [12]. The gel-like slurry particle size was checked before using slurry making electrode as showed in figure2.3.

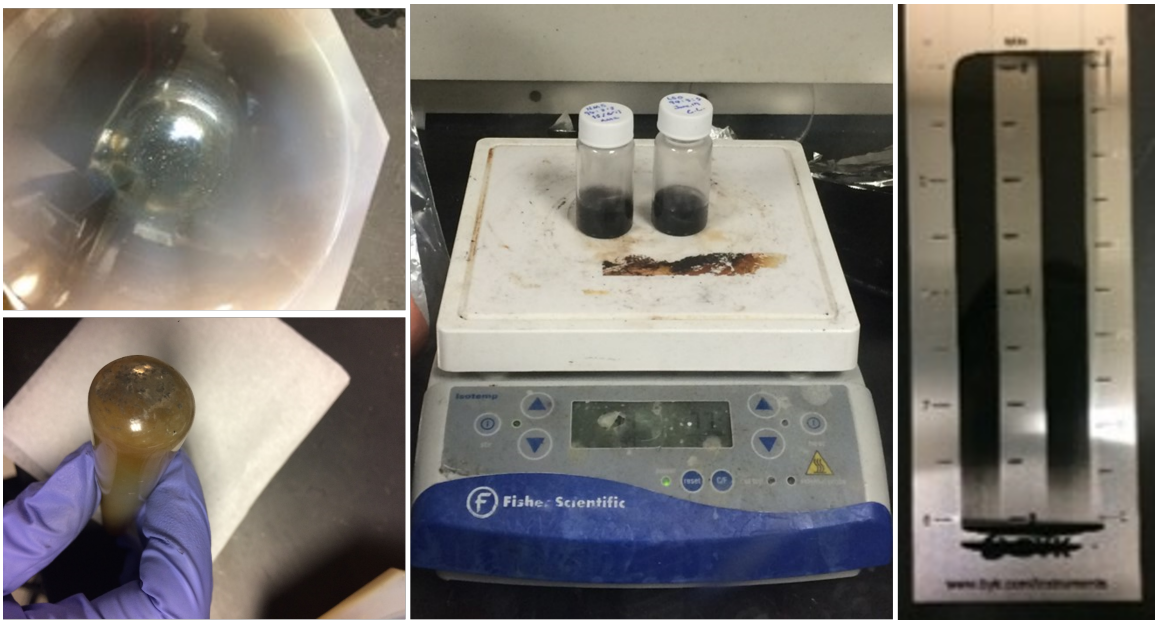

Fig. 2.3. NMC coin cell slurry making process: grounding, mixing and particle size testing.

The slurry was coated onto a thin aluminum foil via a film casting doctor blade (EQ-Se-KTQ-100, MTI, Richmond, CA, USA) shown in Figure. The doctor blade was pre-set to a certain thickness to ensure each electrode on the current collector had a uniform thickness. By controlling the setting of the doctor blade, four different thickness of NMC electrodes were coated on the current collector. The coating thickness of electrodes before dry is influenced by the slurry thickness, doctor blade setting, coating researcher, environment condition. Normally we need to make plenty of electrodes to get the electrode thickness we required after dry. The coating thickness of electrodes before dry is not same every time. Doctor blade height setting we have used to making different thickness electrodes are as the following table. Each set electrodes are made from one bottle of slurry under the same condition at the same day. We control the electrodes after dry are 50um, 70um, 80um, 100um. The approximate setting height of Doctor blade and dry thickness are shown in table 2.1.

To minimize the experiment error, all the electrodes and cells in this paper are made by one people, out of one bottle of slurry, following the same process and period.

Table 2.2.
Approximate setting height of Doctor blade and electrode dry thickness.

Dry thickness (um)	50	70	80	100
set1(um)	200	250	270	340
set2(um)	220	270	290	330
set3(um)	210	260	280	330

The electrodes were then dried in an oven at 100C for 0.5h. After that, they were pressed down to 50um using a rolling press machine (MR-100A, MTI, Richmond, CA, USA) (50um thick electrode is not pressed). A digital micrometer with one micrometer resolution (Digital micrometer-1IN/25MM, Marathon, Richmond Hill, ON, Canada) was used to measure the thickness of the electrodes before and after pressing. Finally, four 50m thick electrodes with various NMC densities were obtained. The electrodes were cut in 10mm diameter and dried at 100 degree centigrade in a vacuum oven for 10h. These processes are shown in figure 2.4.

2.2.5 Coin Cell Fabrication

The NMC electrodes were assembled with standard 2016 coin cell hardware with, Celgard 2400 separator, liquid electrolyte and 16 mm diameter Li metal sheet as the counter electrode in an argon-filled glovebox(under O_2 smaller 0.1ppm, H_2O smaller 0.1 ppm condition; Unilab 2000, Mbraun, Stratham, NH, USA). The cell was sealed by using a compact hydraulic crimping machine (MSK-110, MTI, Richmond, CA, USA) in the glove box. The cell fabrication order is shown in figure 2.5. All the cells were aged for ten h before the first charge to ensure the full absorption of electrolyte into the pores of the electrodes.

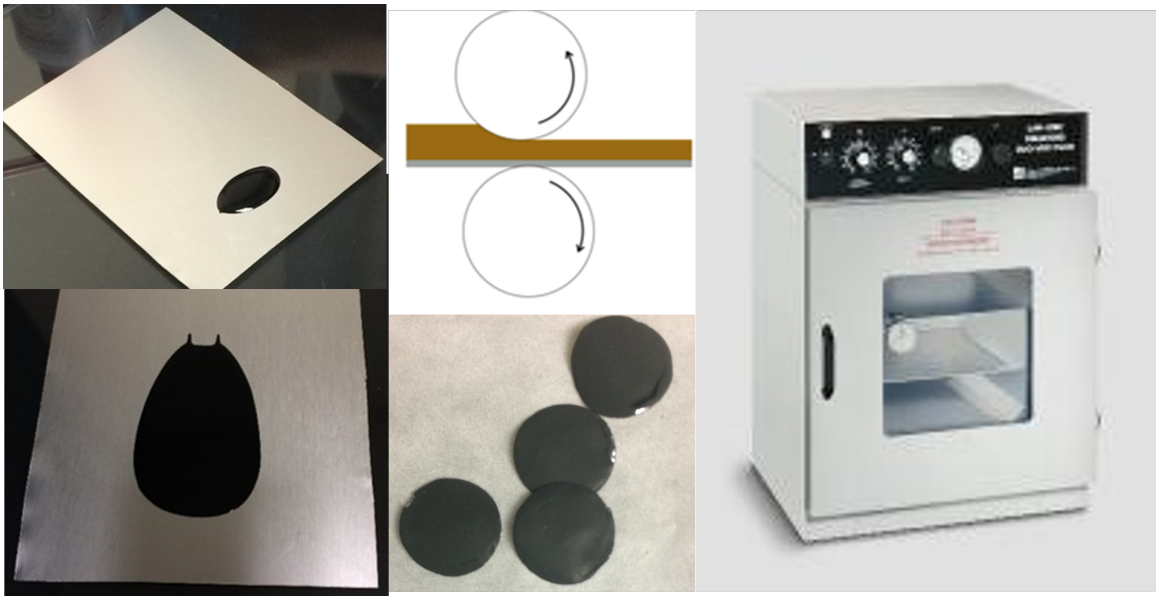

Fig. 2.4. NMC electrodes making process: coating, calending, cutting and vacuum dry.

Li-Li cells were also fabricated by change the active electrode into same size Li mental. They have used for analysis the lithium anode electrochemical impedance spectroscopy (EIS). By wipe off the EIS influence from the Li anode, we could get more accurate EIS information for different NMC cathode electrode.

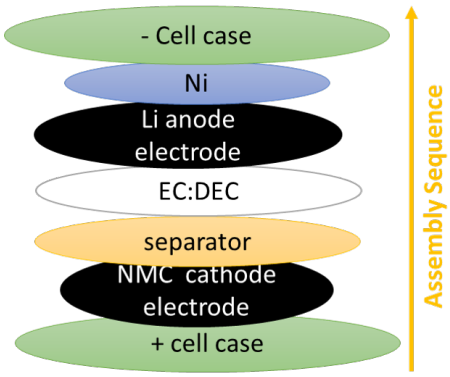

Fig. 2.5. NMC coin cell assemble order sketch map.

2.3 Electrochemical Testing

2.3.1 Introduction

The coin cells were initially cycled three times between 3.0 and 4.2V (vs. Li/Li^+) under a constant current condition at 0.1 C rate. Then electrochemical impedance spectroscopy (EIS) tests were carried out at open circuit potential (4.2V) using a two-electrode system with Li sheet as the counter electrode and NMC as the working electrode (CHI660D, CH Instrument, Austin, TX, USA). Voltage amplitude was set to be five mV and frequency range was form 1,000,000Hz to 0.01Hz. The Zview fitting software was used to fit equivalent circuit parameters. After EIS testing, the cells were cycled for three times at different C rates to investigate electrode capacity and rate capability using a battery cycler (BT2000, Arbin, College Station, TX, USA). The influence of the impedance of lithium counter electrode was described in our previous publication [17].

2.3.2 Charging/Discharging Testing and Analysis

The electrochemical performance of the electrodes with different NMC densities was investigated to study the geometric effects on LIB performance. For each density, multiple cells were fabricated and tested to ensure the repeatability of the electrochemical results. The cells with good capacity retention after rate capability testing were selected to demonstrate the electrochemical characteristics. Figure 2.6 to 2.8 shows discharge profiles of the electrodes under various C rates cycled between 4.2V and 3.0V.

Figure 2.9 and 2.10 shows the discharging capacity of the different NMC density electrodes summarized as rate capability plot and Ragone plot. The capacity retention is all above 90% after the cycling experiment which indicates the discharging curves for different C rates in this experiment are reliable. The capacity retention for different cells are shown as hollow markers at 0.1C rate in figure 2.9. As shown in figure

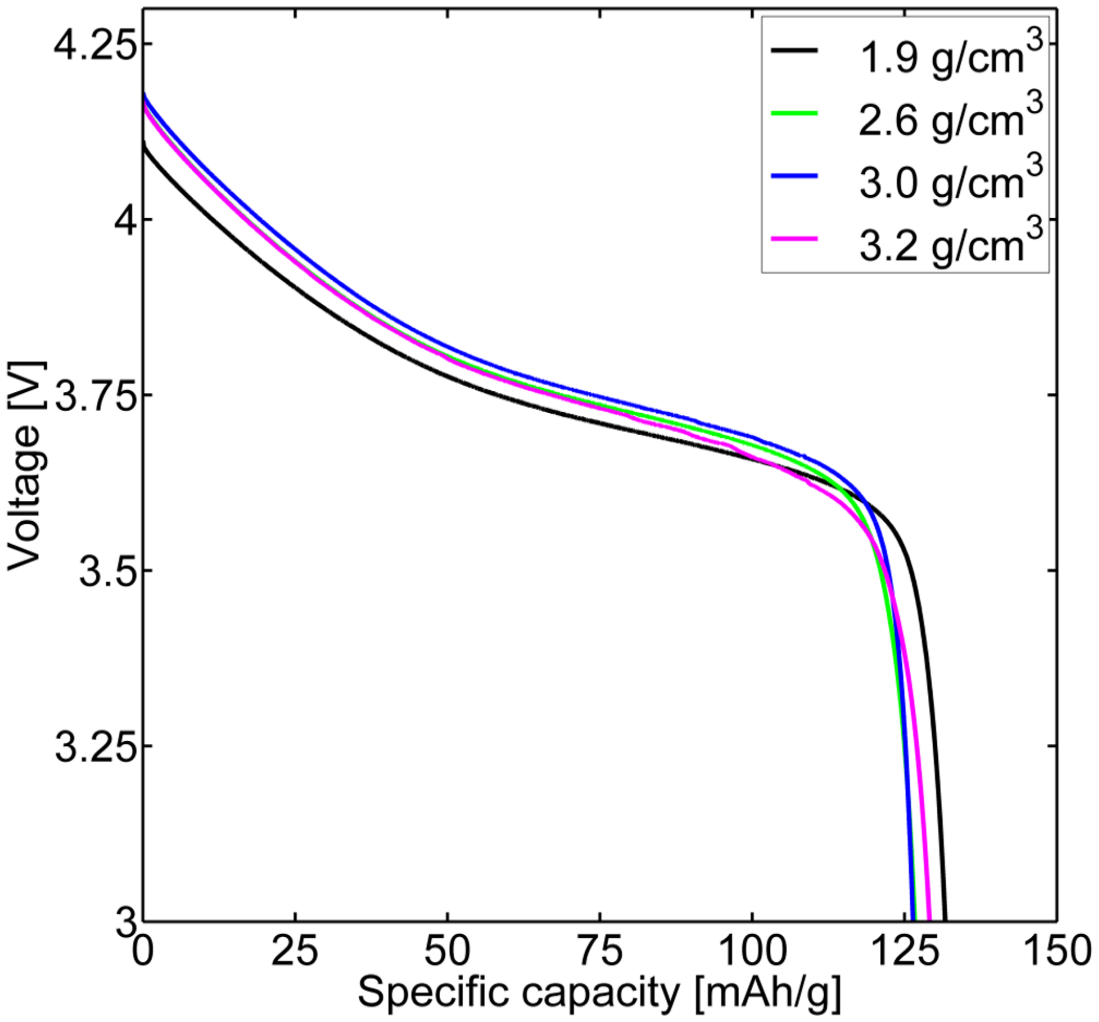

Fig. 2.6. Discharge profiles of the different NMC density electrodes measured at 0.1C rate.

2.9-2.10, at a low rates, such as 0.1C, the four electrodes have similar discharging capacity. As the C rate increases, the capacity of all electrodes starts to decrease, which is normal. However, compared to 3.0 g/cm^3 electrode, 1.9 g/cm^3 and 3.2 g/cm^3 electrodes have a much larger capacity drop. Figure 2.8 shows that the capacity of 1.9 g/cm^3 electrode is too small to shown on the 4C discharge profile. If we compare 1.9 g/cm^3 electrode and 3.2 g/cm^3 electrode, figure 2.6-2.8 shows that 1.9 g/cm^3

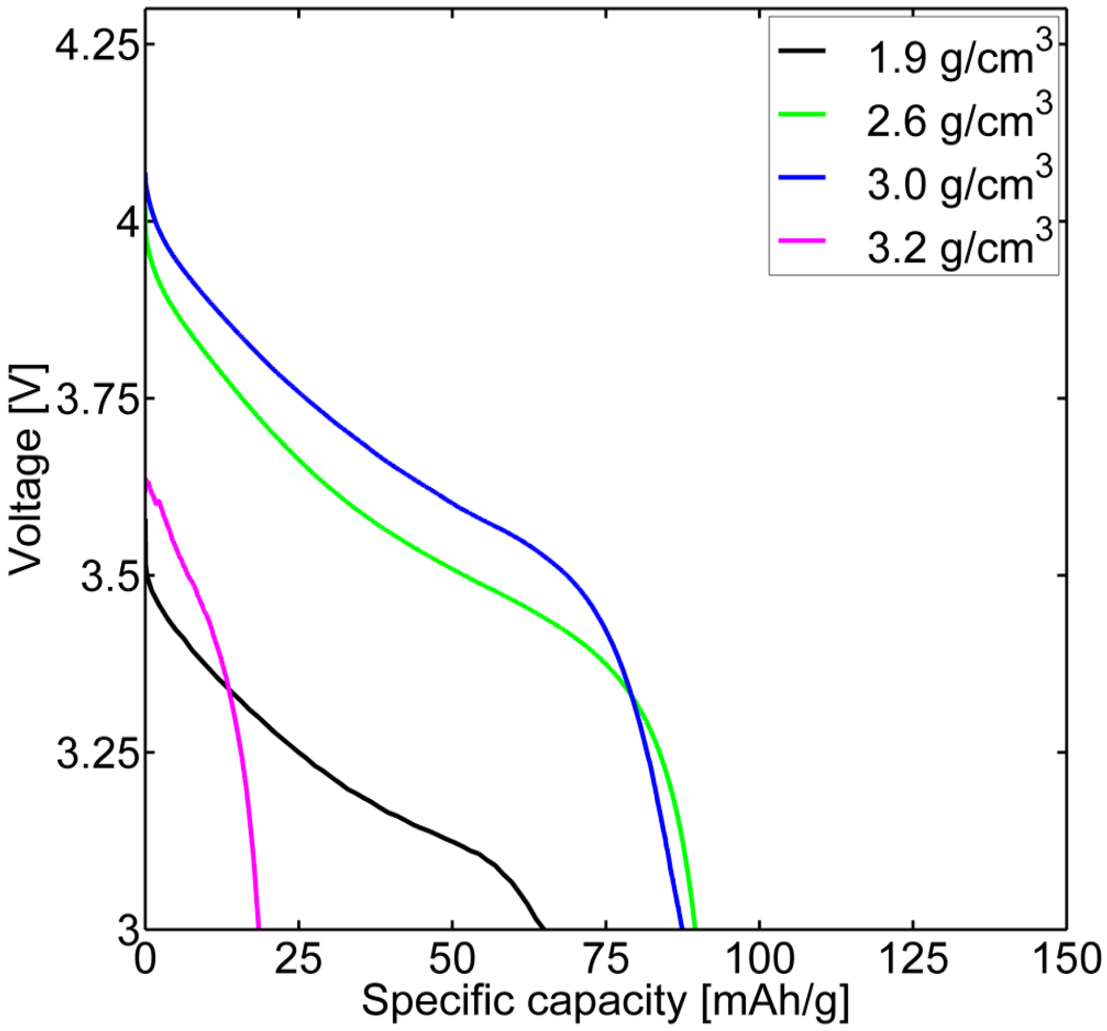

Fig. 2.7. Discharge profiles of the different NMC density electrodes measured at 1C rate.

electrode has larger initial voltage drop due to its large interface resistance, while 3.2 g/cm^3 electrode has a larger capacity loss. As a result, 1.9 g/cm^3 electrode has larger capacity than 3.2 g/cm^3 electrode at the C rates from 0.2C to 1C, but it has lower capacity than 3.2 g/cm^3 electrode due to the much larger ohmic loss at 2C and 4C. 3.2 g/cm^3 electrode still shows small capacity at these C rates, but 1.9 g/cm^3 electrode shows almost zero capacity. It is clear that the effect of NMC density on the capacity

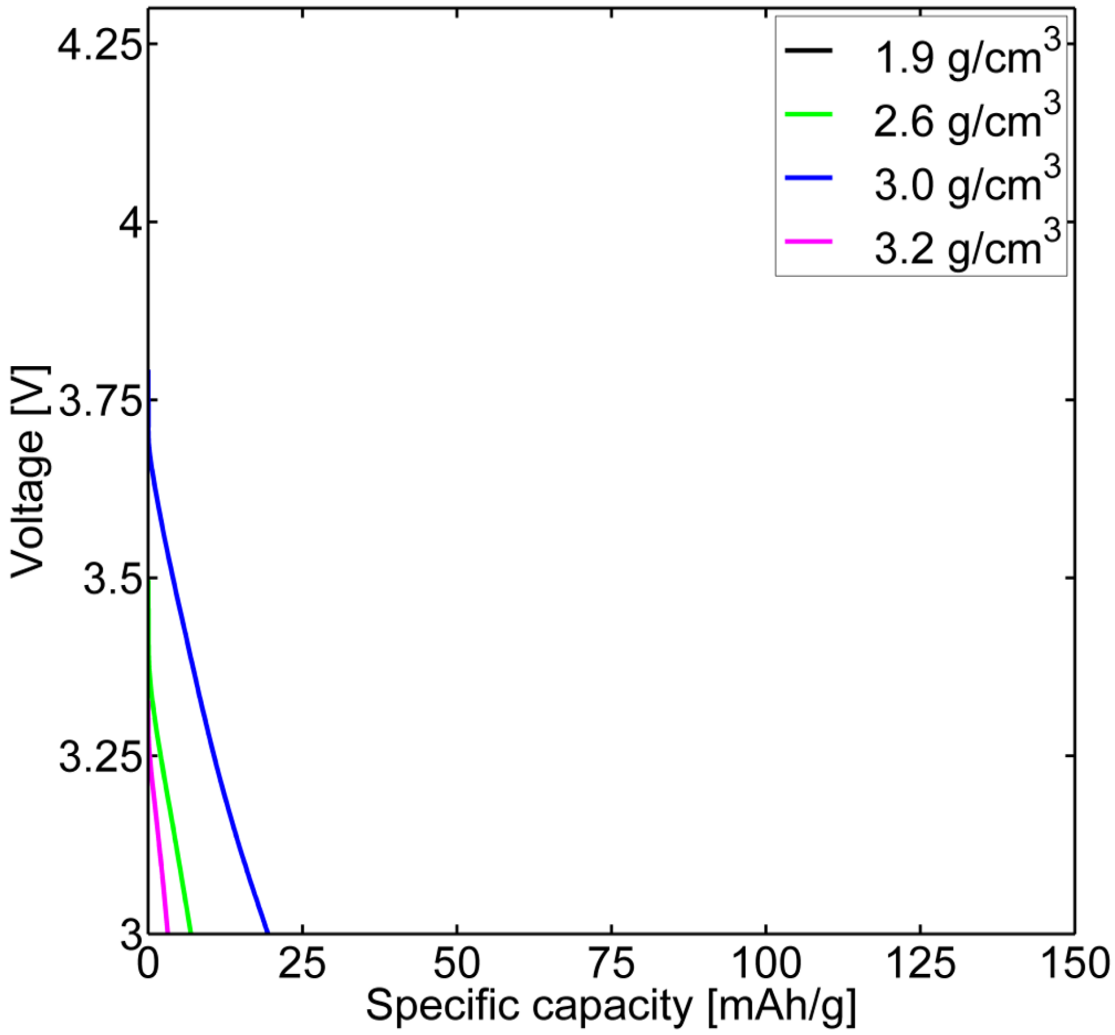

Fig. 2.8. Discharge profiles of the different NMC density electrodes measured at 4C rate.

and rate capability of NMC electrode is different from $LiCoO_2$ electrode [17]. Ebner et al. showed similar discharge performance of NMC electrodes at different NMC densities [19]. However, the density range of their electrode is from 2.2 to 2.8 g/cm3 electrode, which is narrower than the one in our experiment. Also, the crushing of NMC particles is not obvious as shown in their images. Compared to our results,

we think it is reasonable to have similar discharge performance from 2.2g/cm^3 to 2.8g/cm^3 density range.

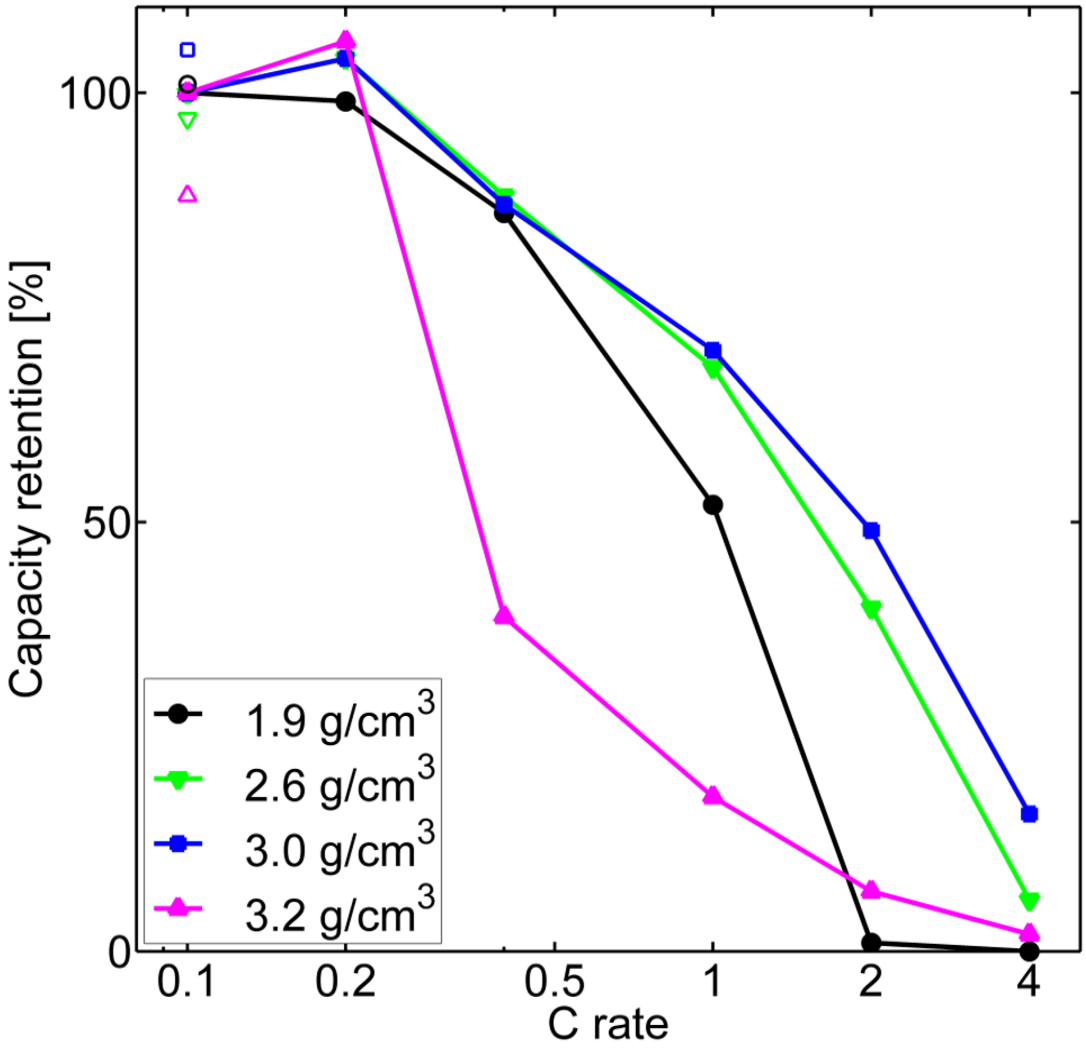

Fig. 2.9. Discharge performance of the different NMC density electrodes summarized as Rate capabilities plot.

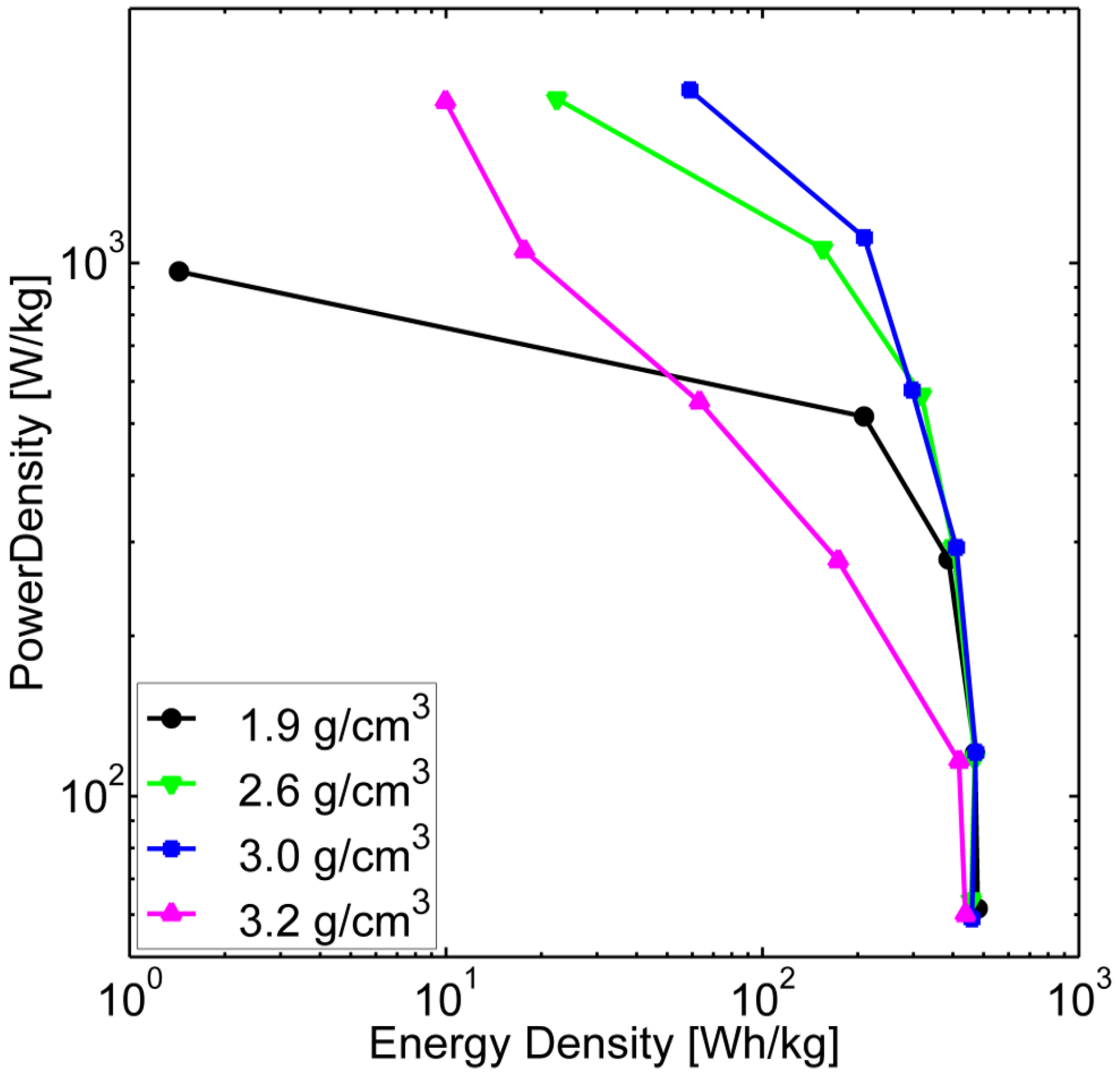

Fig. 2.10. Discharge performance of the different NMC density electrodes summarized as Ragone plot.

2.3.3 Electrochemical Impedance Spectroscopy Testing

EIS results are used to further explain the effects of NMC density on rate capability. The impedance results of the EIS tests for different NMC density electrodes at 4.2V are shown in figure 2.11. All four different density electrodes showed two depressed semicircles when the frequencies progressed from high (left) to low (right).

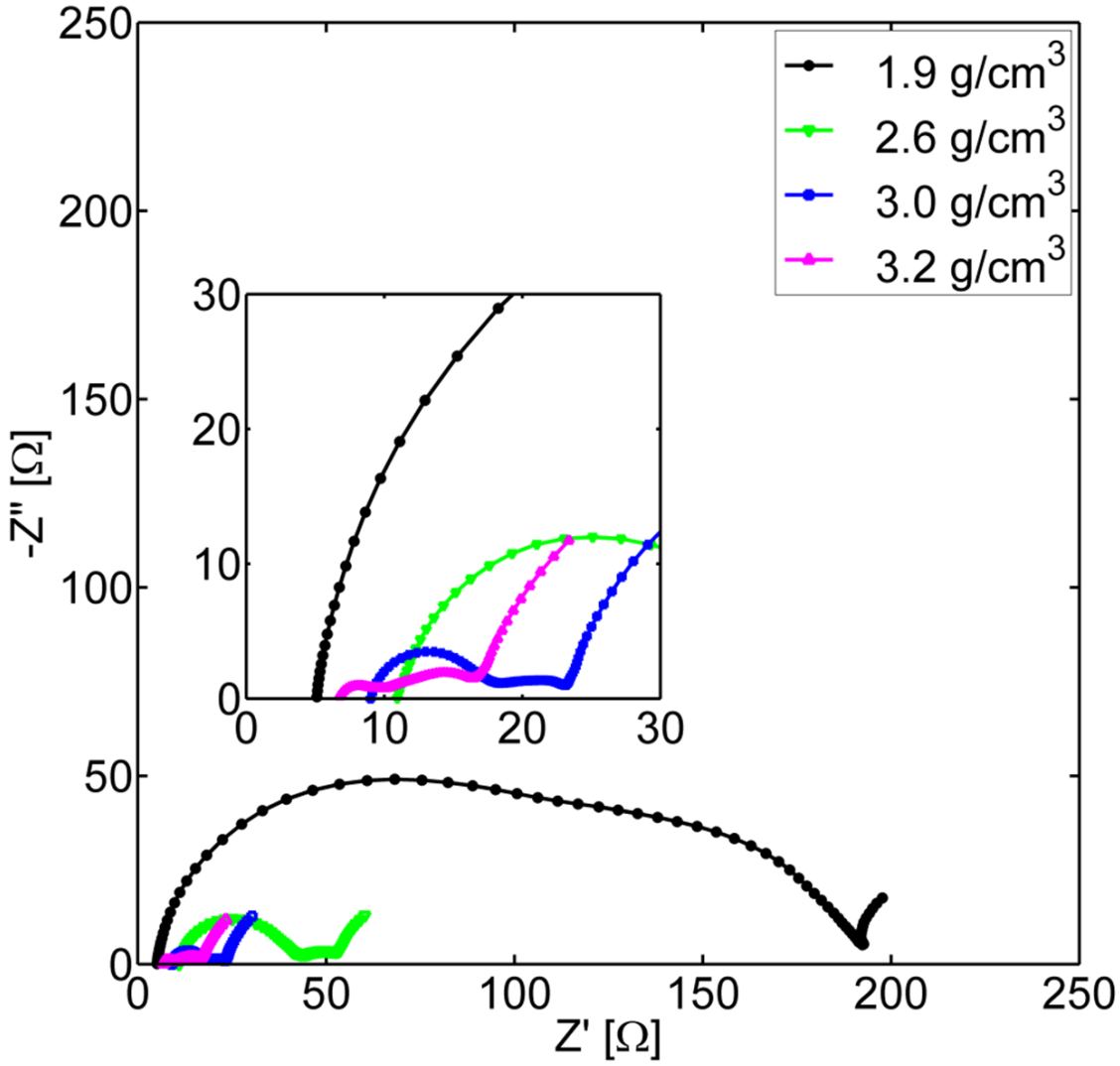

Fig. 2.11. EIS tests results for different NMC density electrodes at 4.2V.

These EIS spectra represent same impedances as the $LiCoO_2$ electrode shown in our previous publication [17]. Briefly, the real axis (Z_0) intercept of the Nyquist plot at the high frequency is assigned as the ohmic resistance of the cell (Re) by the electrolyte [6]. First semicircle in the high-to-mid frequency range is ascribed to the resistance (Rsf) by the SEI layer formed on the active material [22]. The second semicircle in the mid-to-low-frequency range is ascribed to the charge transfer resistance (Rct) at the

electrolyte/electrode interface [23]. Warburg type impedance response (Zw) at the low frequencies is considered as the solid-state diffusion of Li ions within the active material [23] and the electrolyte phase diffusion of Li ion [24]. To quantify the EIS spectra, equivalent circuit displayed in Table 1 was used to analyze the impedance spectra data. All the error percentage generated is lower than 10%, which verifies the validity of the equivalent circuit. As shown in Table 1, 1.9 g/cm^3 electrode has much larger Rsf and Rct than the other electrodes. 3.0 g/cm^3 and 3.2 g/cm^3 electrodes have the similar Rsf and Rct. However, the rate capability of 3.2 g/cm^3 electrode is not the best. Since ohmic resistance (Re) of the four electrodes is similar, we can conclude that the high tortuosity at high NMC density is not limiting the rated capacity of 3.2 g/cm^3 electrode. This phenomenon can be explained by the electrochemically active area theory proposed in our previous publication [4] and the crushing of NMC particles in 3.2 g/cm^3 electrode. The smaller pore size and uniform pore distribution cause more uniform distribution of conductive carbon-binder matrix and better contact between carbon-binder matrix and NMC particles, which lead to the increase of electrochemically active area. Thus, the Rsf and Rct are reduced in the high NMC density electrodes, and 3.0 g/cm^3 electrode has better rate capability than 1.9 g/cm^3 electrode. It should be noted that the conductivity of carbon-binder matrix can be degraded during cell cycling. Grillet et al. reported that ectrochemically-induced mechanical stresses degrade binder conductivity, increasing the internal resistance of the battery with cycling [25]. Although 3.2 g/cm^3 electrode also has low Rsf and Rct, many NMC particles were crushed during calendering process. The nanometer-sized NMC particles are not connected well electronically and ionically, which can result in high impedance inside the particles. At low C rates, the capacity is not affected. However, at high C rates, many loosely connected nanometer-sized NMC particles become inactive, and the capacity reduces significantly. This effect of calendering is different from the $LiCoO_2$ electrode, which has the best performance at the highest $LiCoO_2$ density until the limitation of the calendering process is reached [4].

3. NMC ELECTRODE GEOMETRIC CHARACTERISTICS STUDY

3.1 Preface

Recently, porous electrode microstructures have been reconstructed by advanced tomography techniques such as X-ray nano-computed tomography (nano-CT) [4, 26–34] and focused ion beam scanning electron microscope (FIB-SEM) tomography [14, 35, 36]. The reconstructed microstructures have been applied to investigate the geometric characteristics and electrochemical performance of LIB electrodes with different calendering conditions. For instance, Ebner et al. studied the influence of compression and percentage vary of carbon black and binder on NMC cathode electrode porosity and discharge capacity by using synchrotron radiation X-ray tomographic microscopy. Their results show that compression results in a porosity decrease by a factor of two, but has no significant impact on the high rate constant current discharge capacity [19]. The major advantage of their tomography system is the large field of view of the microscope, which can generate a very large reconstruction volume to ensure the accuracy of structural analysis, especially for tortuosity. However, the voxel size of the synchrotron radiation X-ray tomographic microscopy used in Ebners study is $370 \times 370 \times 370$ nm^3 , which is not small enough to reveal the detailed microstructural information at smaller scales. In our recent publication, Lim et al. studied the geometric and electrochemical characteristics of lithium cobalt oxide ($LiCoO_2$) cathode electrode with different packing densities using a synchrotron TXM tomography with voxel size of $58.2 \times 58.2 \times 58.2$ nm^3 [4]. They found that $LiCoO_2$ electrode with higher packing density shows larger capacity and better rate capability. Chen-Wiegart et al. studied the 3D morphology of a commercial LIB composite $LiCoO_2$-NMC positive electrode using a synchrotron TXM with voxel size

of $38.9 \times 38.9 \times 38.9$ nm^3 [20, 37]. They found that the NMC particles have a much rougher surface compared to the $LiCoO_2$ particles. Cracks due to processing exist in both $LiCoO_2$ and NMC particles but the NMC particles exhibit more severe cracking and also tend to have internal pores in addition to radial cracks. In addition to experimental studies, the reconstructed microstructures have been utilized in electrochemical simulations to predict electrode performance. For instance, Mendoza et al. conducted coupled electrochemical-mechanical simulations based on 3D reconstruction of $LiCoO_2$ electrode and reported that the binder has a significant role in relaxing the overall stresses throughout the microstructure as well as at particle contacts [21].

Therefore, the purpose of this chapter is to investigate the realistic geometric characteristics of NMC cathode electrode microstructures with different calendering conditions and their impacts on electrochemical performance using synchrotron TXM tomography with high spatial resolution.

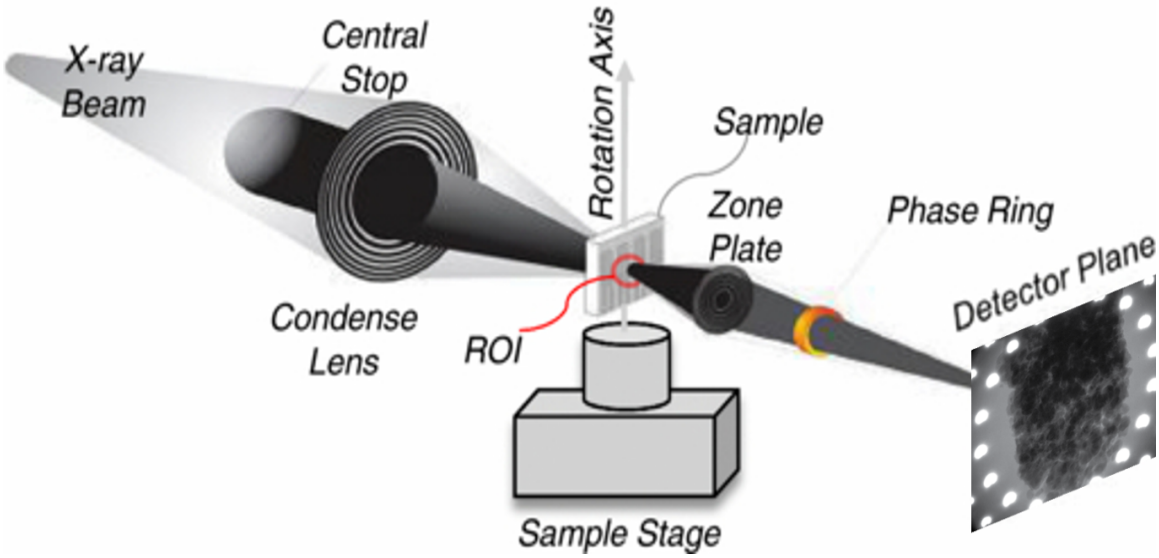

Fig. 3.1. X-ray computerized tomography working principle.

The working principle of X-ray Computerized Tomography is shown in figure 3.1. Coming X-ray beam is concentrated by condense lens to the sample, then the

dispersed beam was concentrated and projected on detector plane. The detector plane recorded the strong and week signal of X-ray.

In this study, four NMC electrodes were fabricated from a same composition of materials, and calendered to an identical thickness under different loading of NMC. We reconstructed the porous microstructures of electrodes with different calendering conditions to examine geometric characteristics by employing synchrotron TXM tomography at the Advanced Photon Source (APS) of the Argonne National Laboratory (ANL). The electrodes were assembled in coin cells with a Li counter electrode to investigate the electrochemical characteristics. The impact of calendering condition on the porous microstructure and electrochemical performance of NMC electrode is discussed based on the microstructural and electrochemical results.

3.2 Synchrotron TXM Tomography Experiment

We used the same electrodes we got for electrochemical testing. Four different thickness electrodes were all tested in this part. We needed to break the electrodes into small pieces with sharp tip smaller than 60 um for the experiment. While with Aluminum foil it is hard to make such sharp tip, so Aluminum foil was removed. Carbon and PVDF have much lower X-ray absorptivity than NMC, so these two phase are not showing in the X-ray CT images results, they could not be distinguished with pores. Aluminum foil was removed by soaking the electrode in 30% NaOH solution. Because we use PVDF as binder (only soluble in organic solvent such as NMP), which allowed the electrode to maintain shape when put into water. Then the electrodes were cleaned by DI water, dried in air and broke into sharp edge samples by using a sharp razor. By rewashing the electrode in DI water, we limited the contaminating to be acceptable. Figure 3.2 a shows how to remove aluminum by NaOH. The removing process took around 2minutes, depend on the size of electrode. Figure 3.2 b shows how NMC electrode is sticked on the top of a pin. A sharp edge is expected to be vertical and as sharp as possible.

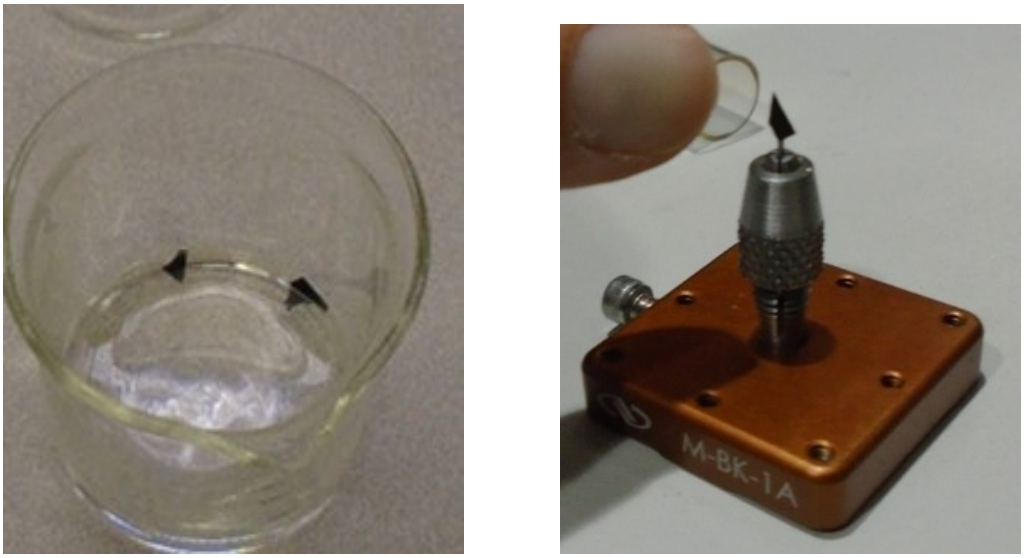

(a) Remove Al by NaOH solution.

(b) Set the NMC electrode sample on a pin.

Fig. 3.2. X-ray testing sample prepare.

The samples were mounted to the rotation stage of the synchrotron TXM at the beamline 32-ID-C at the APS of ANL for tomography scan. High energy level X-ray (8keV) from the beamline was able to capture the projected X-ray images with 2s exposure time at each 0.25degree rotation increments over 180 degree. Flat field images with X-ray on and off were also taken as contrast for image processes.We name them as "white" and "black" images respectively. The total collection time for one electrode sample was 25min. The synchrotron TXM in ANL is shown in figure 3.3.

3.3 Image Processing

One section of the X-ray CT data we get directly from ANL is shown in figure 3.4. The black particles are NMC particles in our sample. Gray parts are space, PVDF and carbon phase combine. We have 720 images with size $2160pix \times 2560pix$. Ten white and ten black images with same image size are shown in figure 3.5 a and b.

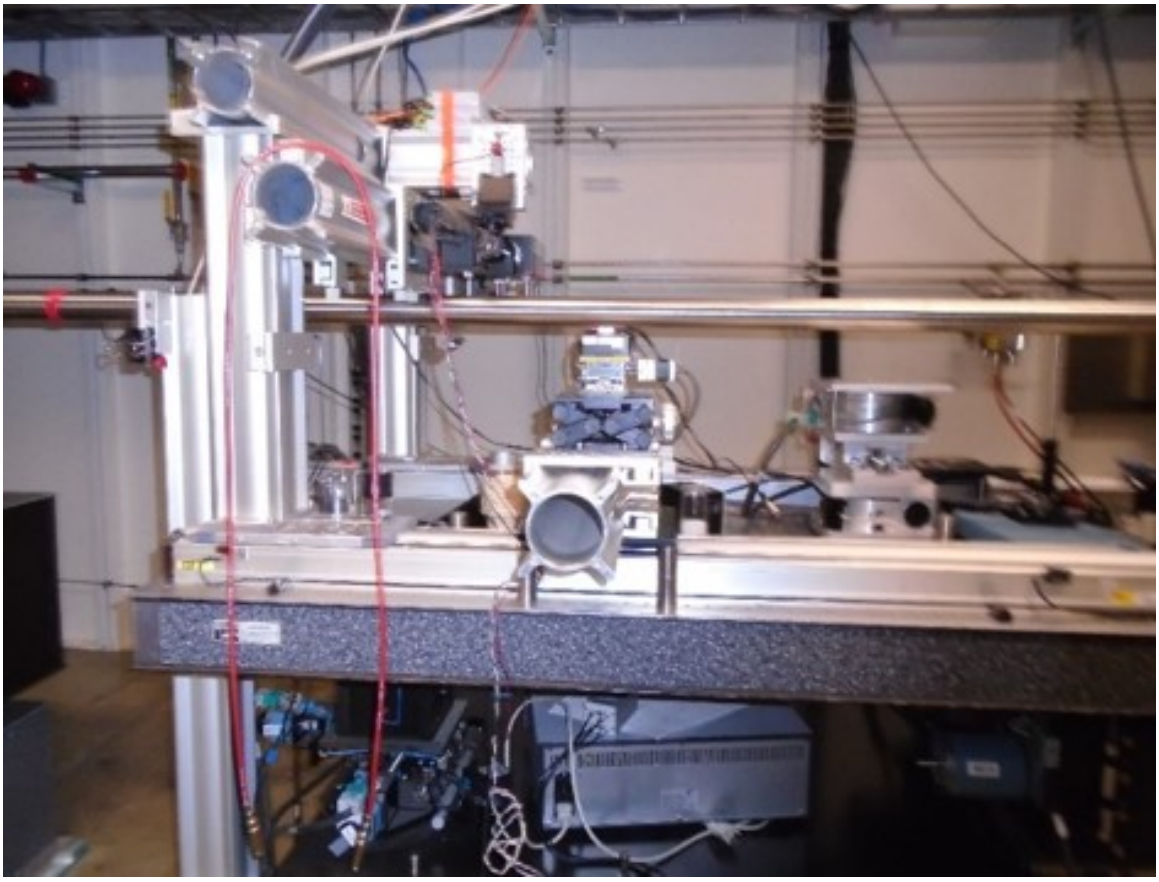

Fig. 3.3. The synchrotron TXM in ANL.

3.3.1 X-ray CT Reconstruction - ImageJ

To get the reconstructed data, ImageJ was first used to checking the raw HDF5 data and distinguish the useful electrode data and reference white/black images. Based on the white images, we could find some clear gray dots. These dots are noise from the optics lens and CCD tomography board. ImageJ was used to remove these noise information from the raw data by reference the white image.

ImageJ was used again for the image slice generated by Python code. Images brightness and contrast were adjusted automatically by ImageJ. To reduce computation time for the latter calculation and focus on the stacked-part of the electrode-

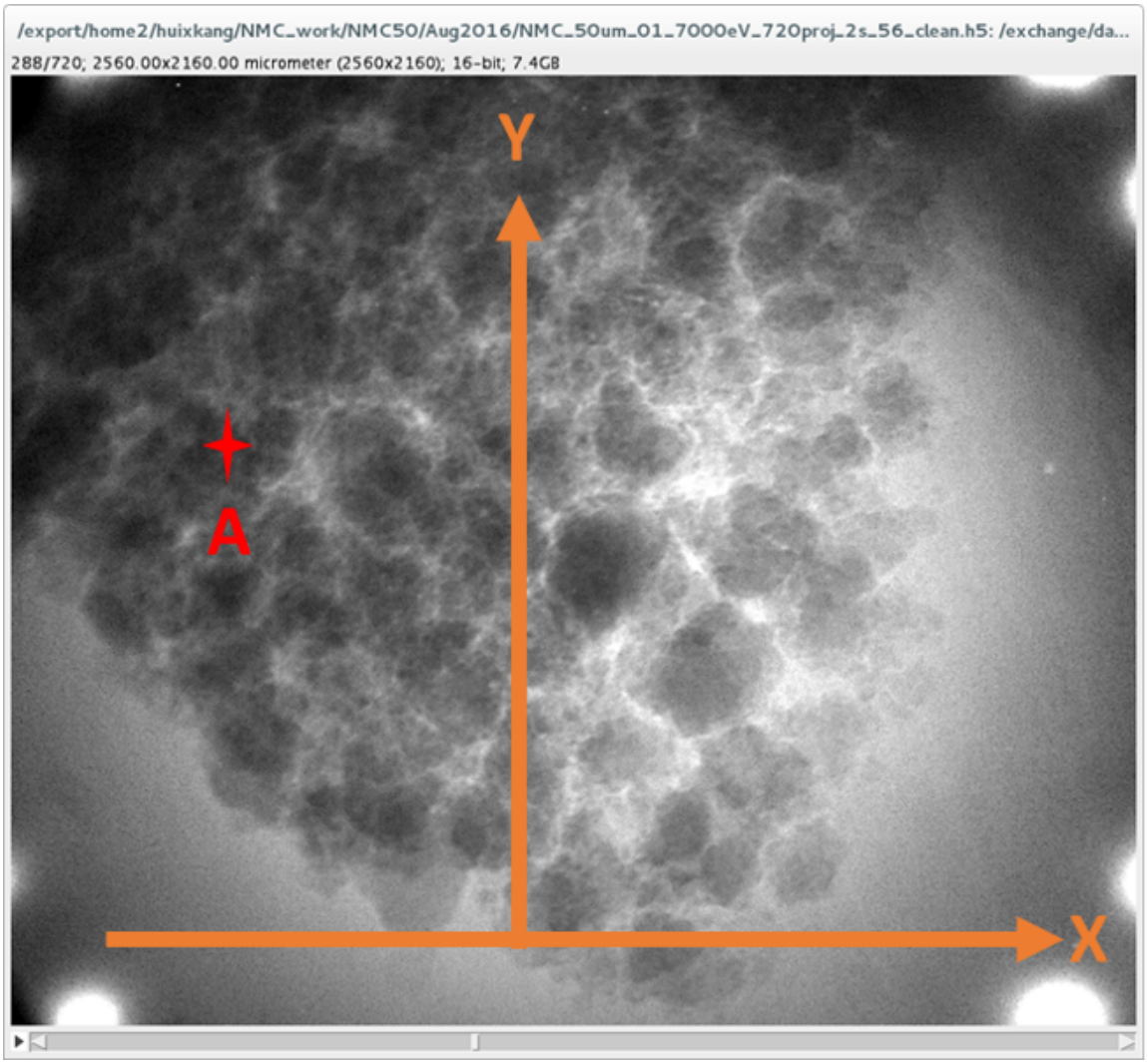

Fig. 3.4. Sample X-ray CT image with rectangular coordinate system.

electrolyte, images were cropped into the biggest solid-cubic (no external space is included). Figure 3.6 shows the Image working flow.

3.3.2 X-ray CT Reconstruction - Python

Python is a powerful programming language which is widely used by researchers. Whats more, Python providing standard packages like NumPy and SciPy offer a free,

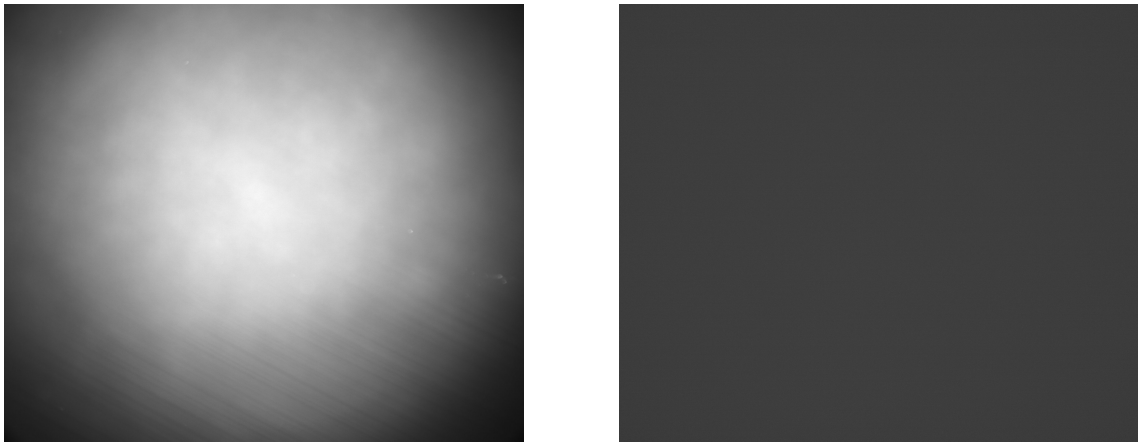

(a) Beam on X-ray CT image.

(b) Beam off X-ray CT image.

Fig. 3.5. X-ray CT white and dark reference images.

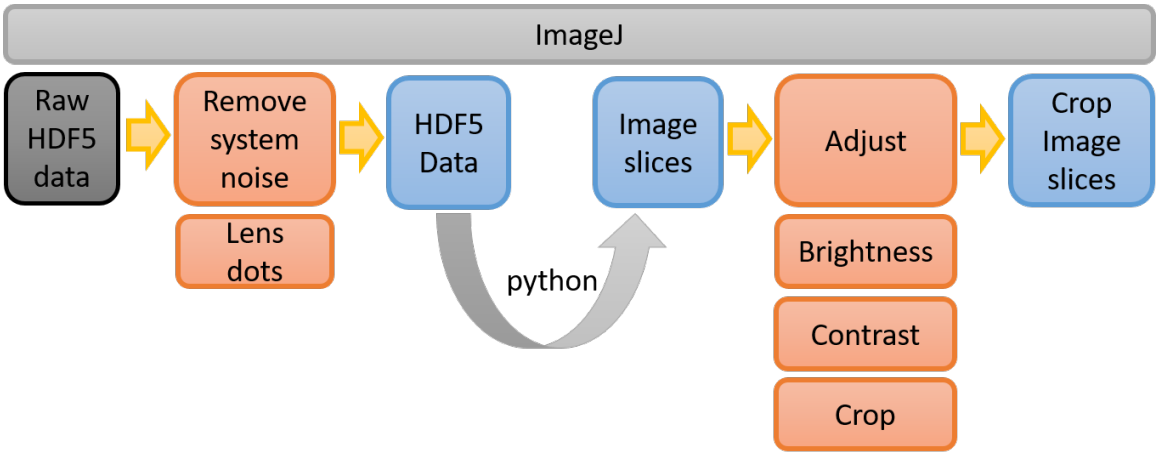

Fig. 3.6. ImageJ working flow.

open-source, modular, readable and manageable framework that researchers can use and contribute to easily. Tomopy and ASTRA are two of the python-based open-source framwork I used in my research.

Tomopy is used to perform tomographic data processing and image reconstruction tasks,developed at the APS of ANL (Gu rsoy et al., 2014). It is available for both Linux and OS X operating systems. Tomopy was developed aiming at providing

a high-level interface for processing and tomographic reconstruction of datasets at synchrotron light sources.

ASTRA toolbox is also an open-source software toolbox developed at the University o f Antwerp, Belgium, and at the Centrum Wiskunde and Informatica (CWI), Amsterdam, The Netherlands. ASTRA is mainly focused on the reconstruction of twodimensional (slice-based) and three-dimensional tomographic datasets (van Aarle et al., 2015). It is available for both Linux and Windows operating systems. ASTRAs goal is to provide a fast and flexible development platform for tomographic reconstruction algorithms. Dr. Pelt ect. reported a method to use Tomopy and ASTRA toolboxes together, which allow users to easily apply advanced tomographic algorithms on large-scale experimental datasets in an efficient way.

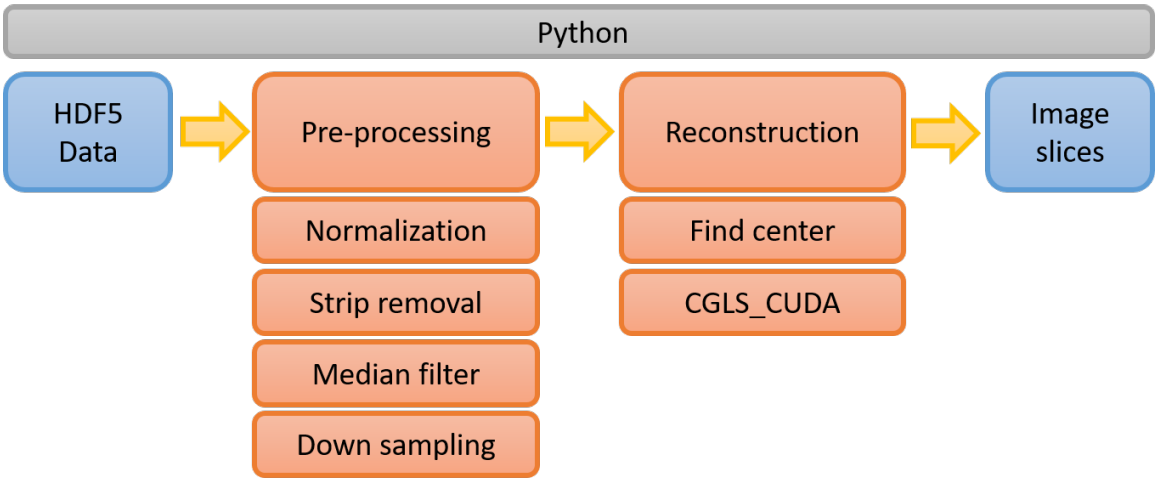

Fig. 3.7. Python working flow.

The flow work of Python code use is shown in figure 3.7. First, noise removing was used for HDF5 data. Normalization, strip removal, median filter and down sampling are some normal image processing method to make the image clear. Second, reconstruction theory. The HDF5 data have 720 projections, just like a cake cut in 720 knives. Figure 3.4 and 3.8 shows the theory of how reconstruction works.

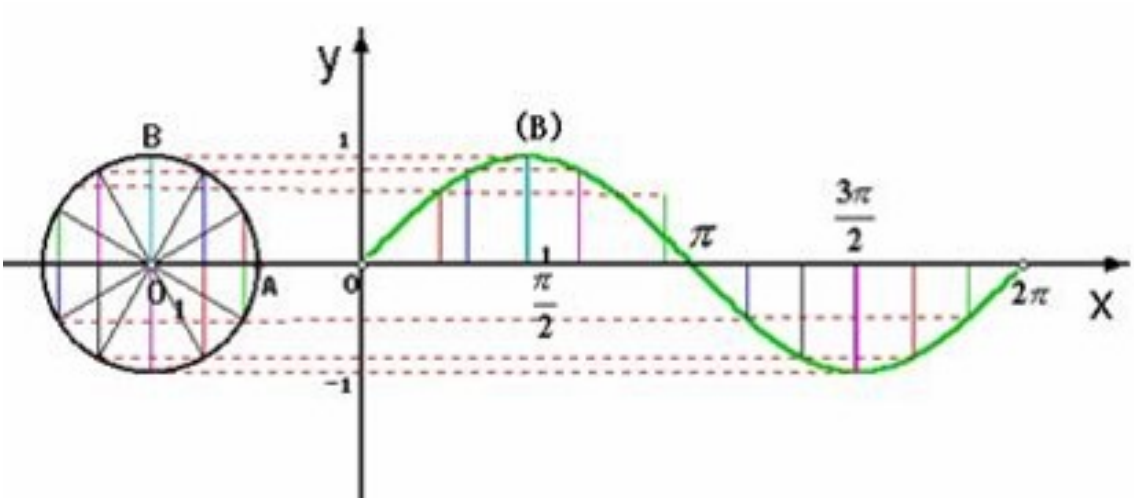

Fig. 3.8. X-ray CT images reconstruction theory.

We could regard every image as a section of one piece of cake, shown in plant X-Y (figure 3.4). Now we want to reconstruct the image into bread slice. As Y axis is the rotation center of the image stack, the brad slice should be cut in X-Z plane (Z direction perpendicular to the paper). Say, we have a particle A in the image. With the rotation, its moving path is a half circle with center on the Y axis (rotation center line). As shown in the circle projection picture, A path projection on the plane XY is a sine function with the rotation angle. Beside on this theory, we could regenerate the " bread" slice. Tomopy and ASTRA toolboxes are used in this process. Third, find rotation center. Based on step two, we could generate one image by using different rotation center value, then manually and automatic compare the the images quality to find the best rotation center. The rotation center value could be any X direction value (center is perpendicular to XZ plane and belong to all the projection images). Forth, using the center and python code to reconstruct the hole data set. NMC electrode CT reconstruct images for 1.9g/cm^3 2.6g/cm^3, 3.0g/cm^3 and 3.2g.cm^3 electrodes are shown from figure 3.9 to figure 3.12.

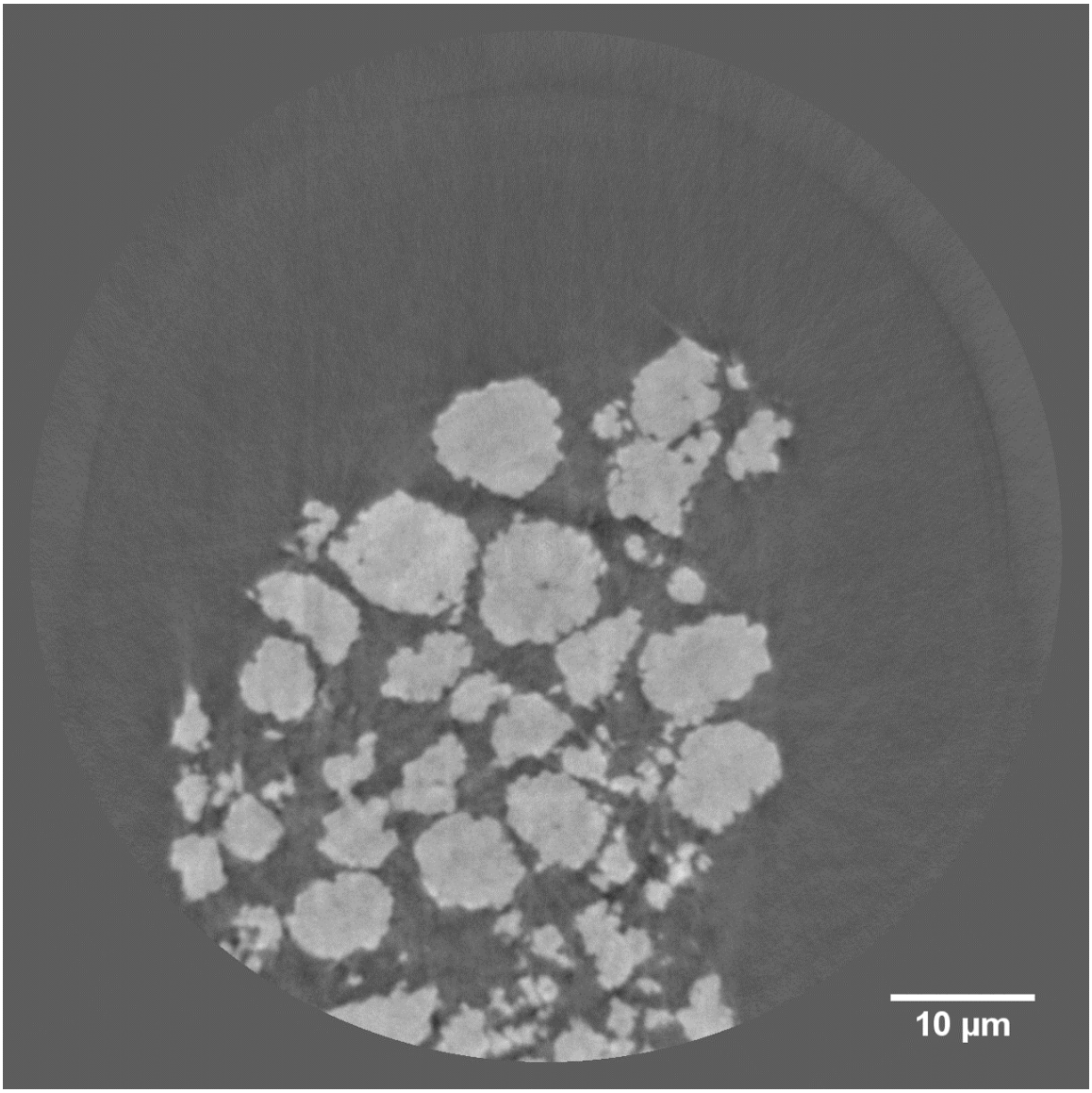

Fig. 3.9. 1.9g/cm^3 NMC electrode CT reconstruction image.

3.3.3 X-ray CT Reconstruction - MATLAB.

MATLAB coding is based on matrix and linear algebra operations. So the first step is to read all the crop images slices we get from imageJ into MATLAB and saving

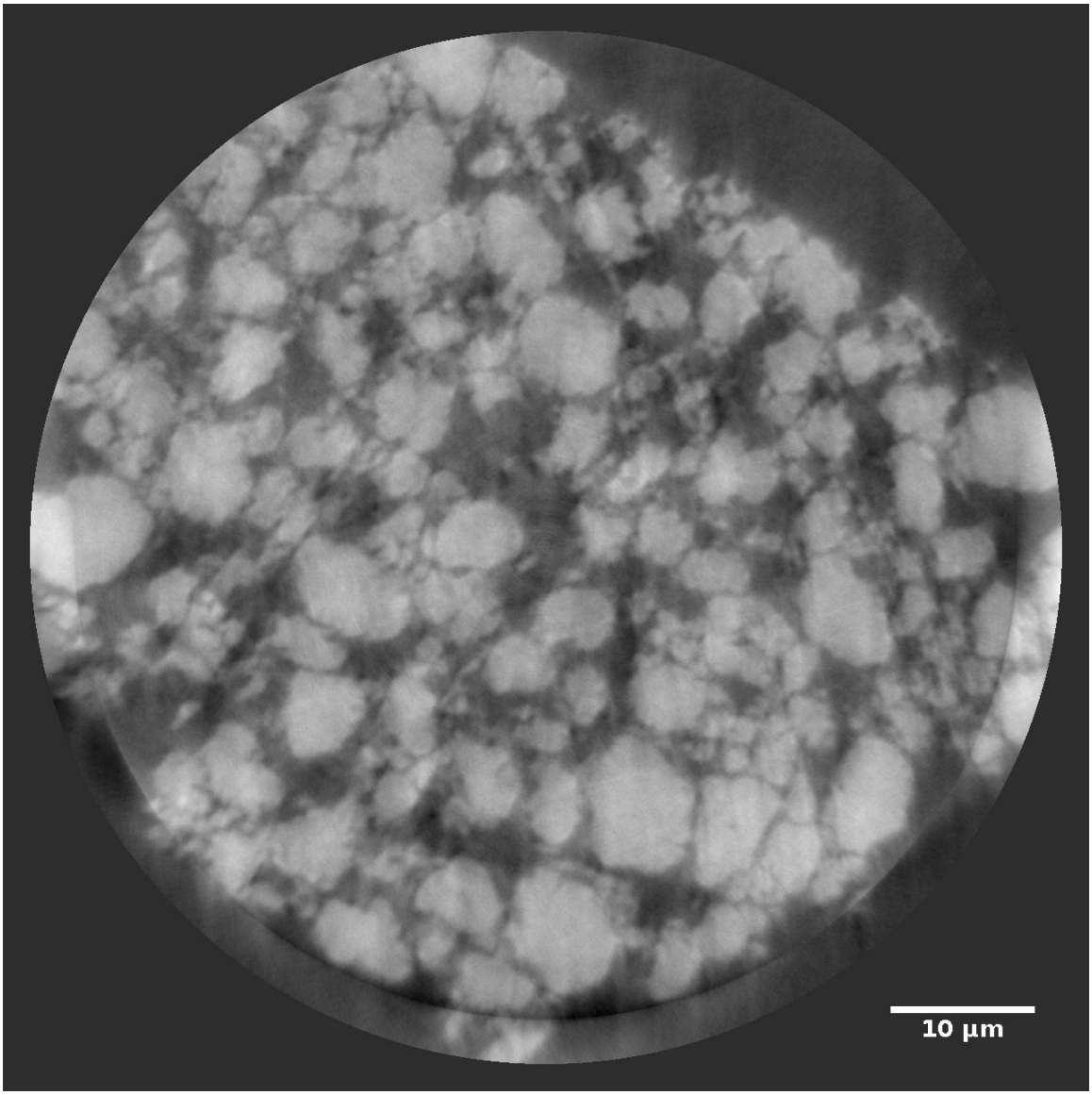

Fig. 3.10. 2.6g/cm^3 NMC electrode CT reconstruction image.

the pixel value into matrix form. Then, 3D Gaussian method provide by MATLAB image processing tool box is used to filter the images (matrix).

The filtered image have a histogram as figure 3.13 shows. The X axis is pixel value, y axis is pixel number. We could find two clear peaks which represent NMC

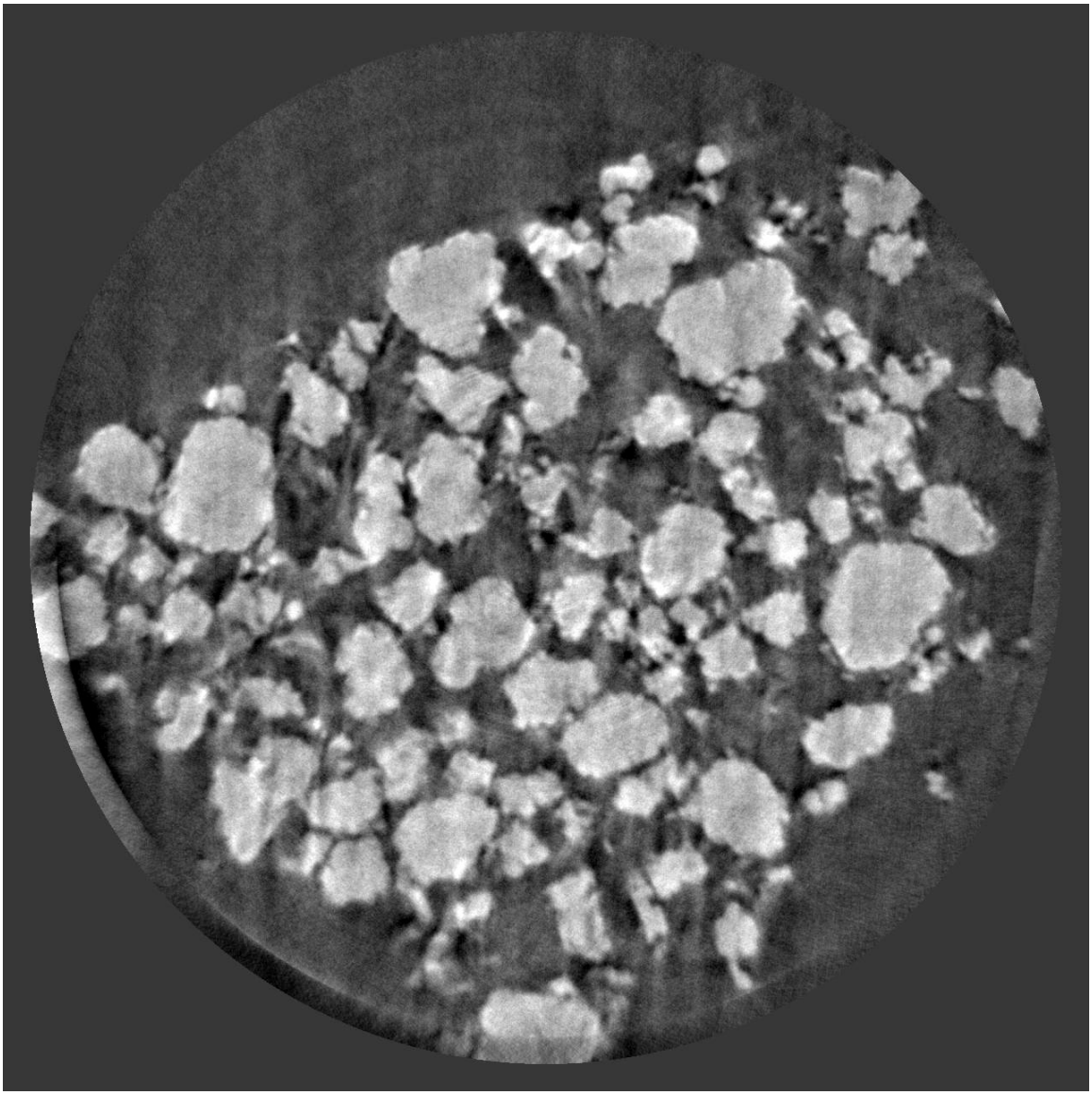

Fig. 3.11. 3.0g/cm^3 NMC electrode CT reconstruction image.

and other phase. Figure 3.14 shows the crop process and binary process of the image processing.

The logical matrix is used for 3D mesh (based on iso2mesh MATLAB tool box), pore size distribution calculation, porosity and material percentage calculation. Tetrahedral meshed microstructures of the electrodes were generated from the binary vol-

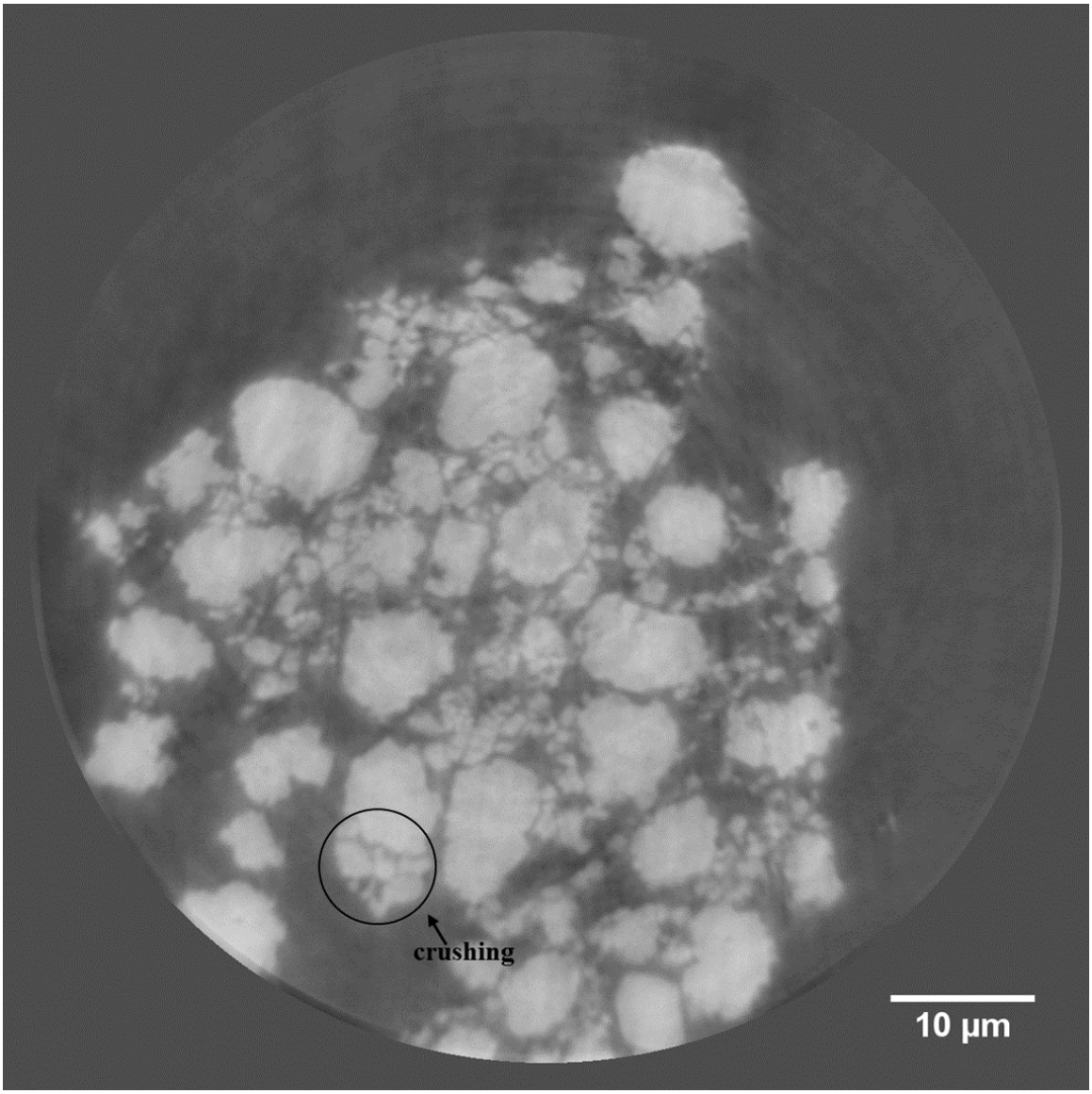

Fig. 3.12. 3.2g/cm^3 NMC electrode CT reconstruction image.

umetric data with iso2mesh MATLAB algorithm [38]. The meshing algorithm extracted surface from a binary data and generated a surface mesh based on Delaunay refinement process. Tetrahedral volume mesh was generated from the surface mesh. The MATLAB working flow is shown in figure 3.15.

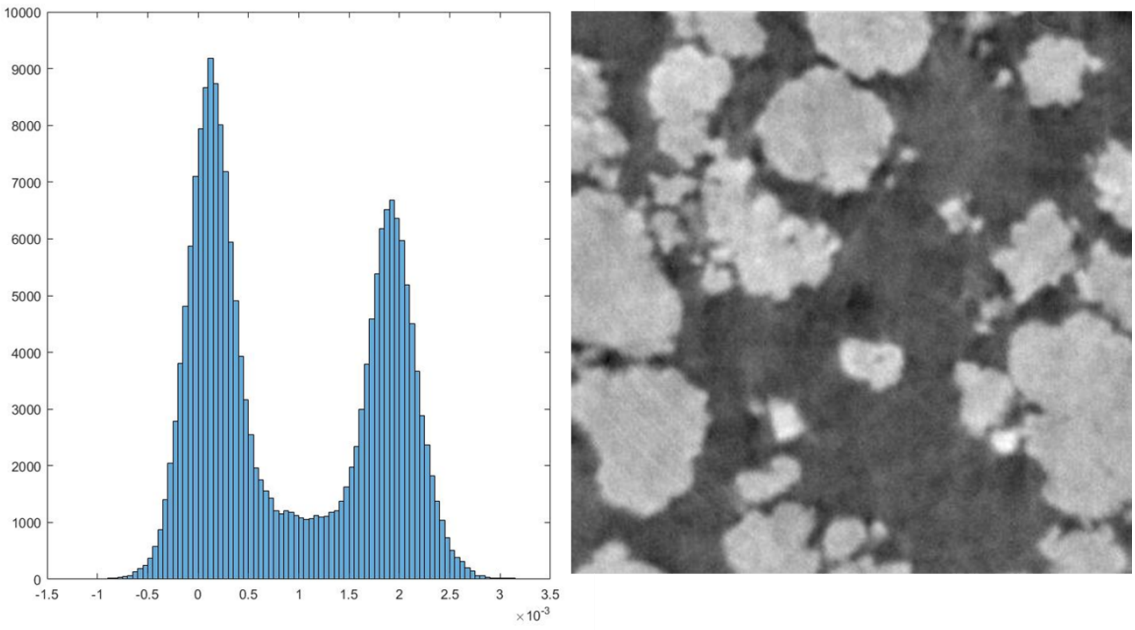

Fig. 3.13. Sample CT reconstruction image histograme of 1.9g/cm^3 electrode with X axis represent pixel value, Y axis represent pixel number.

Avizo is also used to calculate the particle size distribution in the following section. NMC electrode 3D reconstruction data generated by Abizo is shown in figure 3.16.

3.3.4 CT Results Comparison

Here is an compare of the CT results in Dr. Ebner‘s work and in our research [19]. Dr. Ebner‘s work is remarkable and the large volume of reconstruction gives a good view and enough particle information for general analyze. According to the uncompressed SEM image shown in their paper, the NMC particles are as big as 30um, and the majority particles are around 10um. The sub-particles used to synthesis NMC particles have a diameter around 0.5um. The resulting voxel size they get is $0.37 \times 0.37 \times 0.37$ um^3 , which means its hard to distinguish the sub-particles under this resolution, especially when sub-particles are fall off after crushing. This will limit

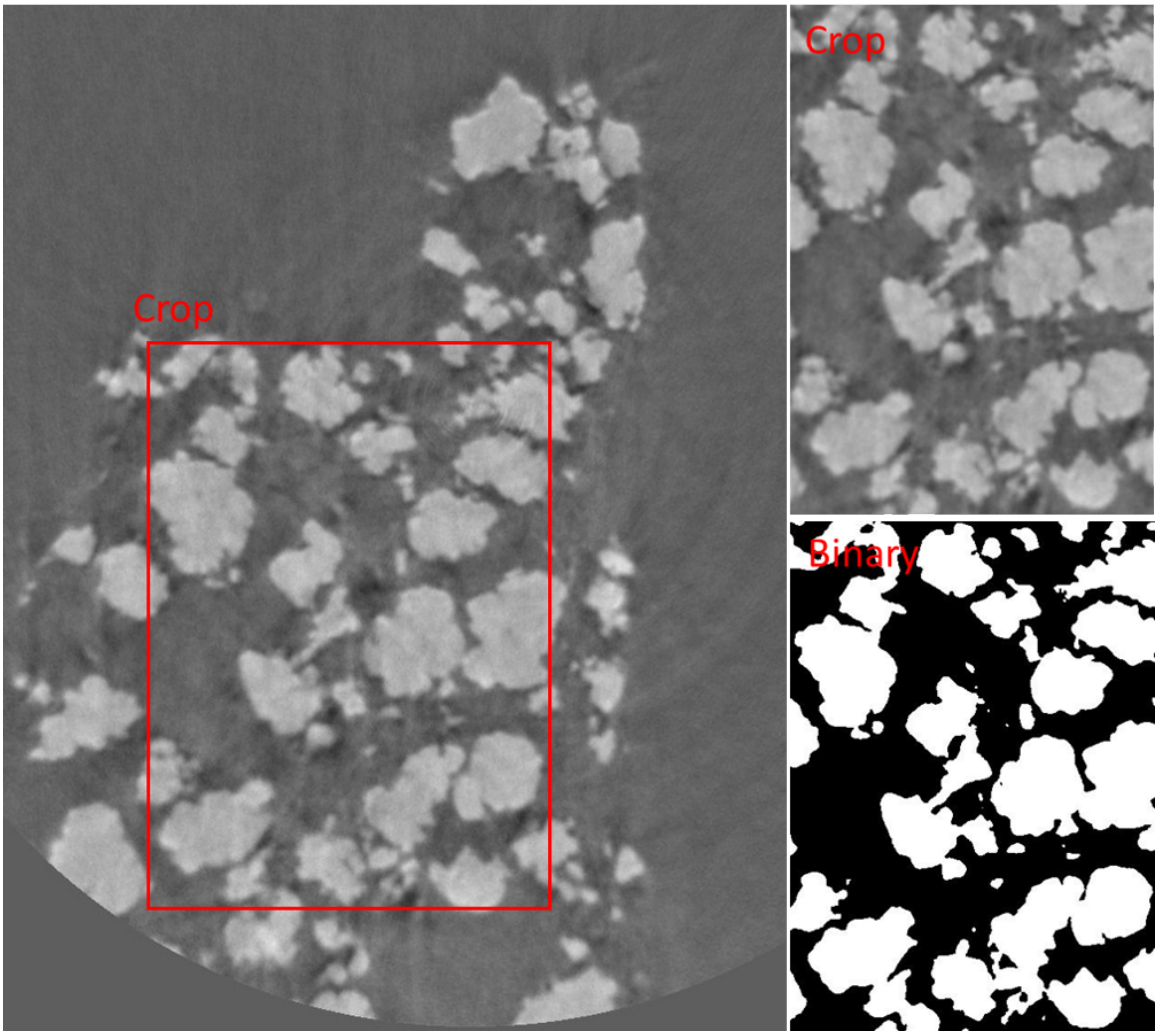

Fig. 3.14. Sample cropping and binary image of 1.9g/cm^3 electrode.

the tortuosity analysis on NMC particle level rather than sub-particle level. While in our experiment, the majority NMC particles size are 6um and as big as 10um. The sub-particles used to synthesis NMC particles also have a diameter around 0.5um. The spatial resolution is 0.0582 m, which is 6.4 times smaller than Dr. Ebner‘s work and enable to study sub-particles. In Dr. Ebner‘s work single NMC unit shows crank (figure 1 i and j) after press, while under higher resolution, we could clearly see the

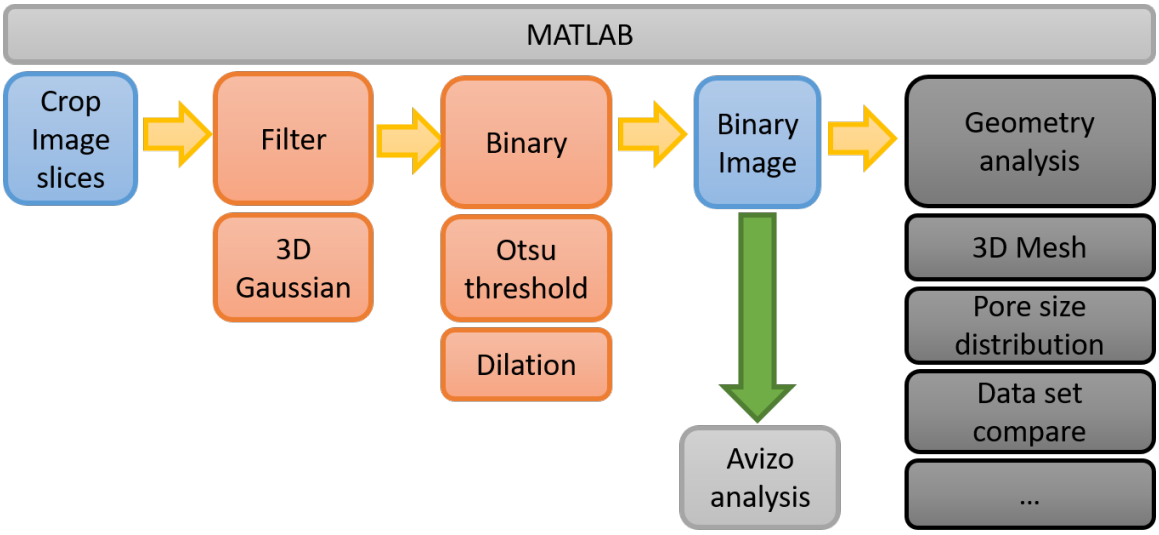

Fig. 3.15. MATLAB working flow.

NMC unit is break in to small particles lays very close instead of cracks. Under this condition, ion go through cracks, which is tortuosity, need to be reconsidered.

A size of $20.4 \times 26.2 \times 29.2$ cubic was get in the end of the image processing and used for next step analysis. By compare our CT volume and papers from Dr. Shearing and Dr. Lim [26, 28], we could find that our volume is big enough for the following analysis. Table 3.1 shows the compare of REV.

Table 3.1.
Compare of X-ray CT REV.

	Median diameter of particle	Majority diameter of particle	REV size (um)	resolution
Dr. Shearing's paper	4.78um	around 40um	43.2*116.2*119.5	0.48um
Dr. Lim's paper	-	around 20um	44.8*44.8*39.2	0.56um
This paper	0.48um	around 5um	20.4*26.2*29.2	0.0582um

(a) 1.9g/cm^3 NMC electrode CT 3D reconstruction.

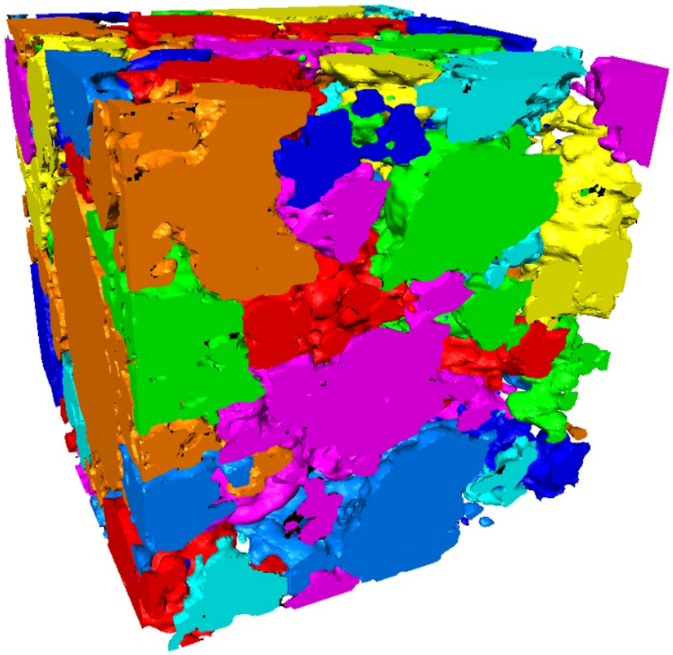

(b) 3.2g/cm^3 NMC electrode CT 3D reconstruction.

Fig. 3.16. NMC electrode 3D reconstruction.

The particle majority diameter we used in our study is 5um, 8 times smaller than Dr. Shearings and four times smaller than Lims. When we scale down the REV recommending size with same proportion, its obvious that the volume size we used is much larger than the recommend REV.

3.4 Geometric Characteristics Study

3.4.1 Material Volume Fraction

Four electrodes with different NMC densities, 1.9 g/cm^3 , 2.6 g/cm^3, 3.0 g/cm^3 and 3.2 g/cm^3 were fabricated by calendering process. The NMC density is calculated by electrode $weight \times NMCpercentage/electrodevolume$. Electrode weight was measured by balance and NMC percentage was set to be 94% in our electrode. Electrode volume was calculated by electrode surface area electrode thickness. The difference of the highest and lowest NMC density electrodes is shown in both X-ray CT images (from figure 3.9 to 3.12), 3D reconstructions (figure 3.16) and SEM images (figure 3.17).

We can clearly see the carbon-binder mix in SEM images. In the CT image, NMC particles are shown as white color. with very rough surface and most of them are not spherical. The particle morphology is similar to the ones shown in Chen-Wiegarts paper [21] but different from the ones shown in Ebner‘s paper [19]. The difference could be due to their large voxel size and different vendor of NMC material. To validate the reconstructed electrode microstructures, the volume fractions of the electrode components based on reconstructed microstructure are compared with the volume fractions based on the measured 10 mm diameter electrodes weight and thickness (figure 3.18). Since PVDF binder and carbon conductor have low X-ray attenuation, they cannot be distinguished from the pore phase. Therefore, the volume fractions of PVDF binder and carbon conductor in figure 3.18 were shown together with pore phase. Volume fraction of a phase is calculated by the volume of the phase over the total volume. As shown in figure 3.18, the volume fractions from reconstructed CT

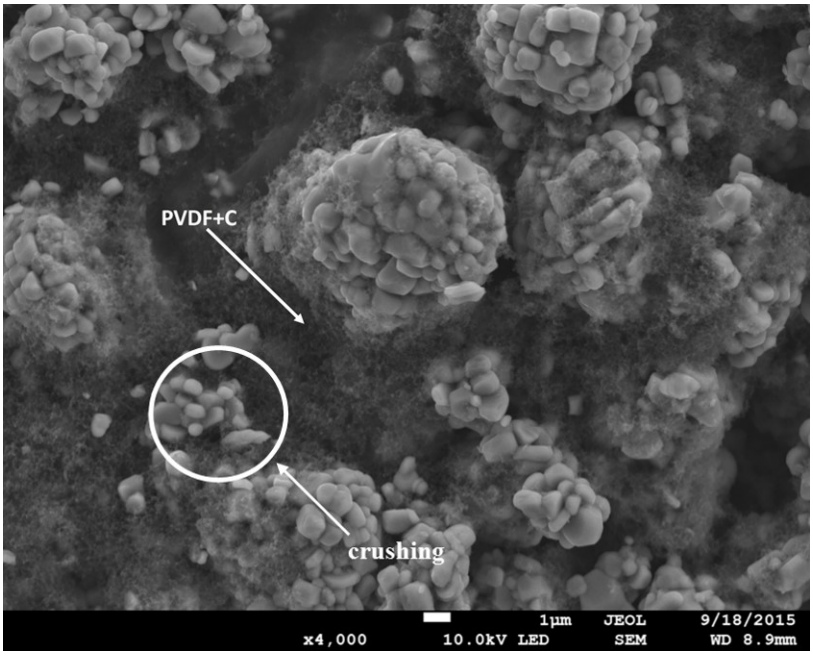

(a) 1.9g/cm^3 NMC electrode SEM image.

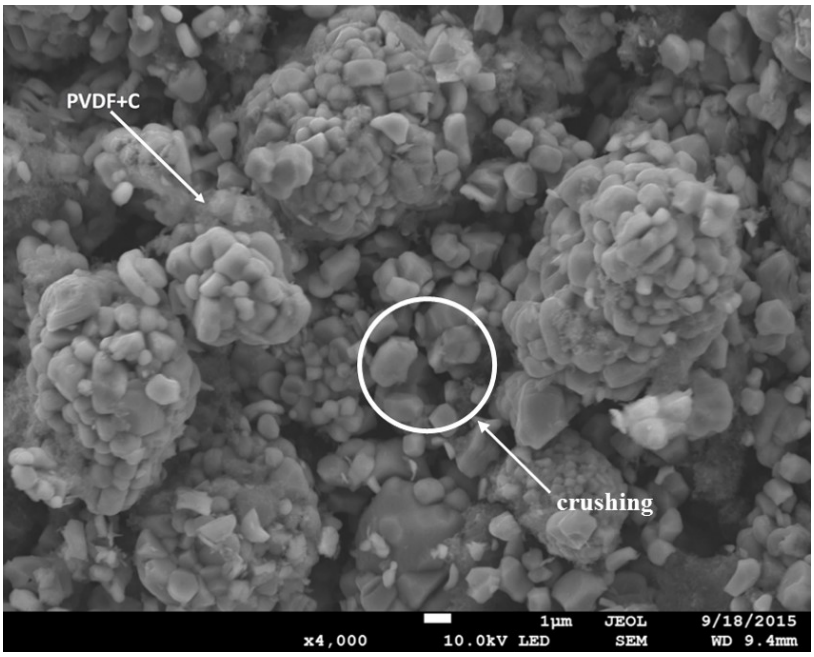

(b) 3.2g/cm^3 NMC electrode SEM image.

Fig. 3.17. SEM image of NMC electrode at different NMC density.

data and weight measurement are consistent. The slight differences between them could be due to several reasons. First, the limited volume of the CT reconstruction and inhomogeneity of the electrode may cause an error. The reconstructed volumes are around $25 \times 25 \times 25$ m^3, which is limited by the field of view of the TXM and sample preparation. Second, electrodes used for CT scan were cut, soaked and rinsed before the experiment, which may lose some particles and decrease the volume fraction of NMC. Third, the thickness of electrodes was measured by a digital micrometer with 1um resolution. Since the total thickness is 50um, theoretically there is a 2% measuring error.

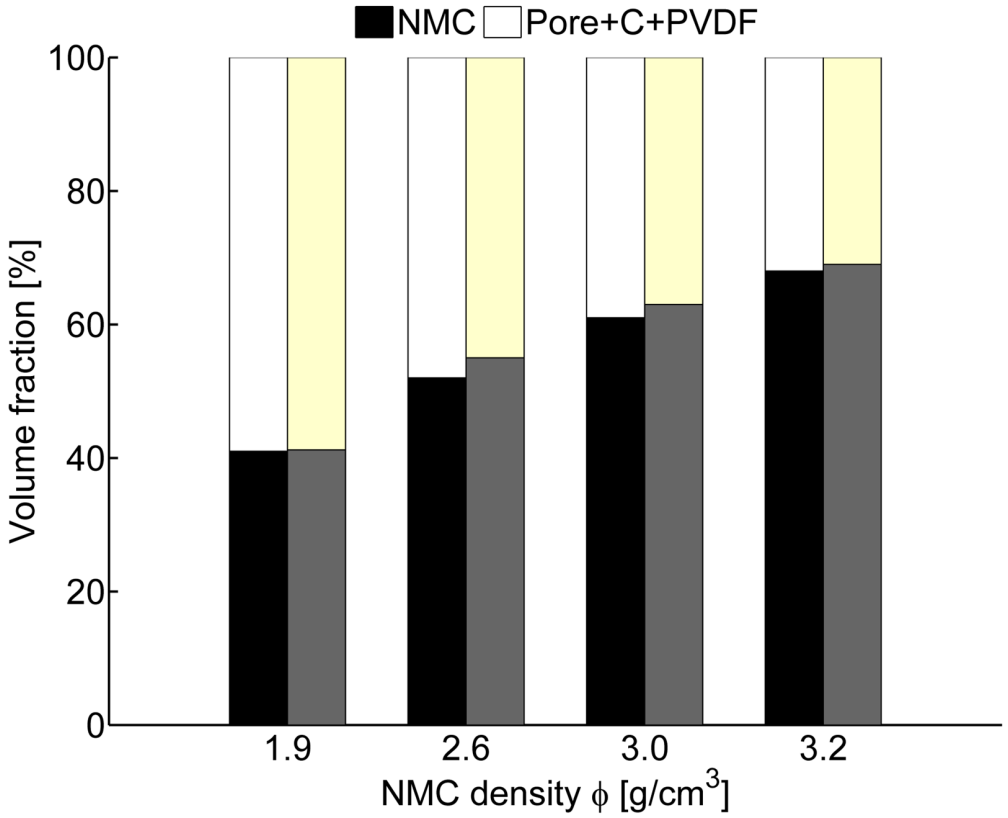

Fig. 3.18. Volume fractions of NMC and pore+C+PVDF calculated from the reconstructed porous microstructures (left) and the loadings of the different NMC density electrodes (right).

3.4.2 Particle Size Distribution

As shown from figure 3.9 to 3.12, with calendering percentage increasing, porosity is decreased, but many NMC particles are crushed into smaller sub-particles. To quantify this phenomenon, particle size distribution was calculated from equivalent spherical diameters of particles generated from CT labeled data by using Avizo. The frequency distributions of particle size (q3) of the four different electrodes are shown in figure 3.19. The curve of 1.9 g/cm^3 electrode shows a normal distribution of particle size, which should be similar to the original NMC particles. The curves of the other three electrodes show larger distribution at larger size. It is mainly due to the resolution of TXM tomography (58.2 nm). Any gap smaller than this resolution cannot be detected. Since the particles are tightly packed at high densities, some of them may be combined as a single large particle after CT reconstruction. However, the 3.2 g/cm^3 electrode has much higher distribution between 2 and 4 um and lower distribution between 4 and 7 um, which demonstrates that increasing calendering percentage crushed more NMC particles to sub-particles. The crushing of NMC particles could have a negative impact on the cell performance.

3.4.3 Pore Size Distribution

Pore size distribution (PSD) is an important parameter to characterize the morphology of porous LIB electrode [39]. In this study, PSD is quantified from the 3D binary CT data using the method described in Ref [20]. PSD of different NMC density electrodes and the corresponding box plot are shown in figure 3.11 and figure 3.22.

The PSD results were calculated from the combined phase of pore and carbon-binder matrix because carbon and PVDF phases cannot be distinguished from the pore phase. The relative volume is defined as the total volume of a pore radius over the volume of the inactive phases including carbon, PVDF, and pore phases. The

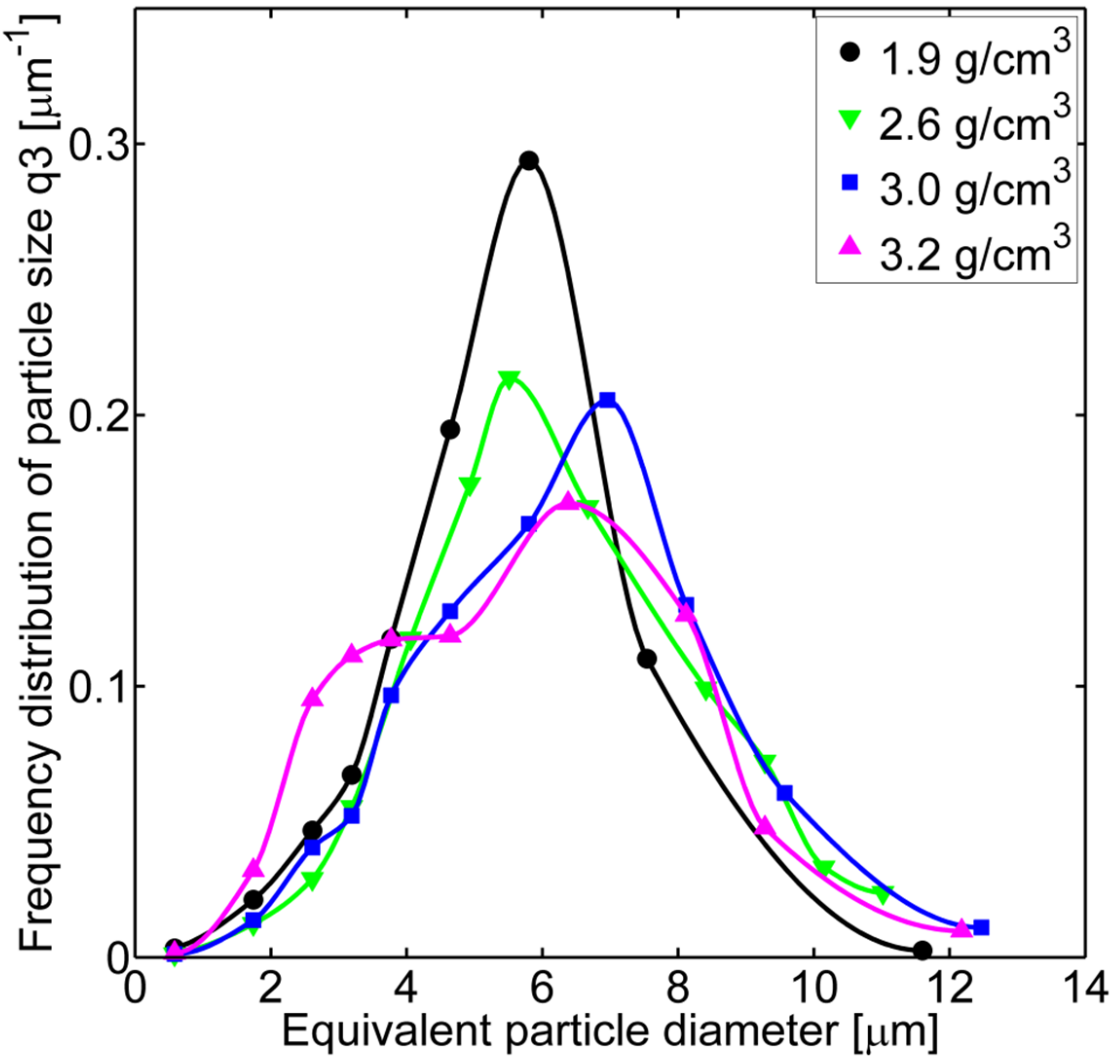

Fig. 3.19. Particle size distribution obtained from the labeled tomography data of the porous electrodes with four different NMC densities

pore radii are positively skewed for all electrodes and tend to concentrate at smaller radius range with the increased NMC density.

Figure 3.21 shows box plots of pore radius of the different packing density electrodes. A box width is a range of pore radii from 25 to 75 percentiles and a centerline in the box indicates a median radius at a corresponding NMC density. The median

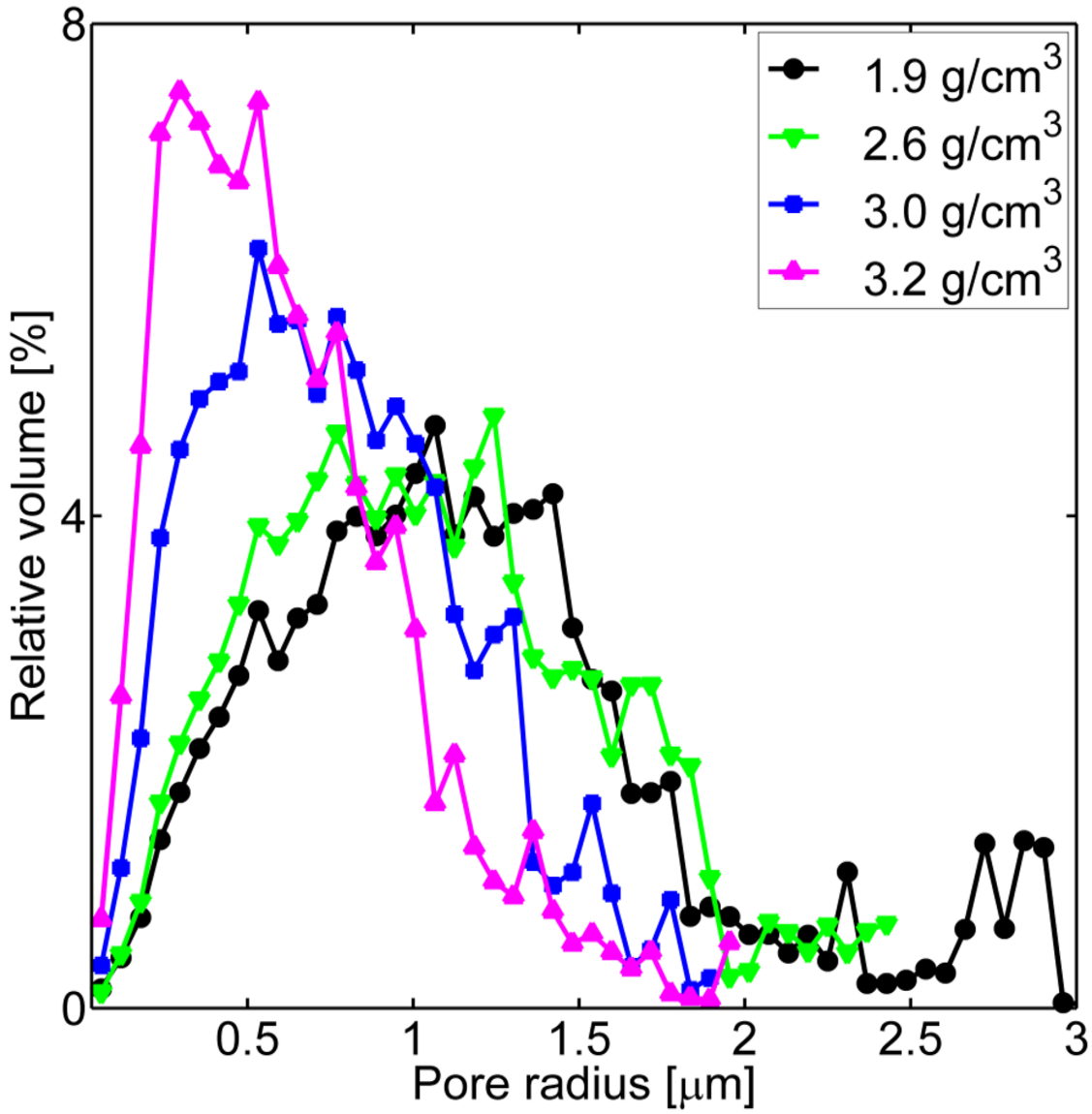

Fig. 3.20. Pore size distribution of the different NMC density electrodes calculated from the reconstructed microstructure with the voxel size of $58.2 \times 58.2 \times 58.2$ nm^3.

and box width are reduced with increasing NMC density. For instance, the relative pore volume of 1.9 g/cm^3 electrode has a wider inter quartile range (box width = 0.71 um) with the median radius 1.12 um and the maximum radius 3.16 um. The relative

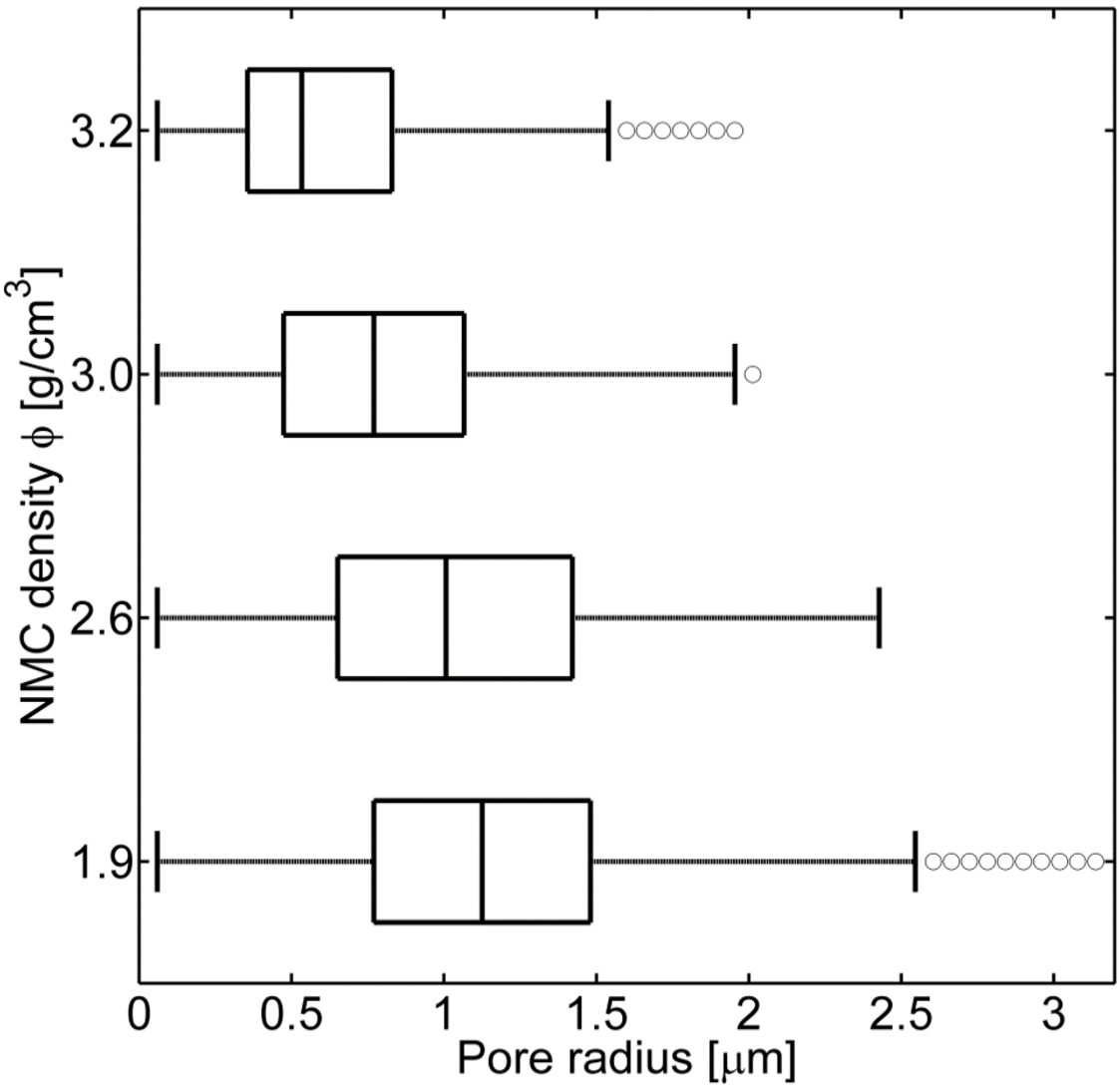

Fig. 3.21. Pore size distribution of the different NMC density electrodes corresponding box plot.

pore volume of 3.2 g/cm^3 electrode has the narrowest box width 0.47 um with the median radius 0.52um and the maximum radius 1.98 um. It is noted that there should be pores smaller than 58.2nm that cannot be detected by the synchrotron TXM. As we can predict from distribution data shown in figure 3.20, the relative volume of those

small pores should be very small. Although the carbon and PVDF phases cannot be distinguished from the pore phase, the result still can relatively demonstrate that the calendering process by the rolling press contributes more homogeneous distributions of pores and carbon-binder matrix.

3.4.4 Specific Surface Area

Specific surface area is the solid-electrolyte interface area of an electrode per bulk volume and it is important in LIB electrode because electrochemical reaction happens on the interface areas. In this study, the specific surface area can be obtained from the reconstructed microstructure. It should be noted that the specific surface area includes both the areas covered by carbon-binder matrix and open areas because the synchrotron TXM cannot distinguish carbon-binder phase from pore phase.

Figure 3.22 shows the specific surface area of the reconstructed electrodes and the homogeneous (spherical particle diameter is 5.2um) electrodes. The results show that the specific surface area increases with the volume fraction of NMC increasing. However, they dont show a clear linear relationship as the $LiCoO_2$ electrode [17]. It is mainly due to the different size distribution of NMC particles at different densities. For the 3.2 g/cm^3 electrode, the sub-particles generated by crushing increase the specific interface area. The CT images also show that the NMC particles have highly irregular shape and rough surface, which can increase the specific surface area. To investigate the effect of surface roughness of NMC particles on specific surface area, several large particles close to spherical shape were selected from the CT data.

Figure 3.23 a and b show the 3D reconstruction of a NMC particle and a SEM image of a NMC particle, respectively. The images demonstrate that the synchrotron TXM tomography can capture the rough surface of NMC particles. The specific surface areas of the particles (surface area/particle volume) calculated from CT data are 140% of the specific surface areas under spherical shape assumption. This important feature cannot be detected by other low resolution tomography techniques.

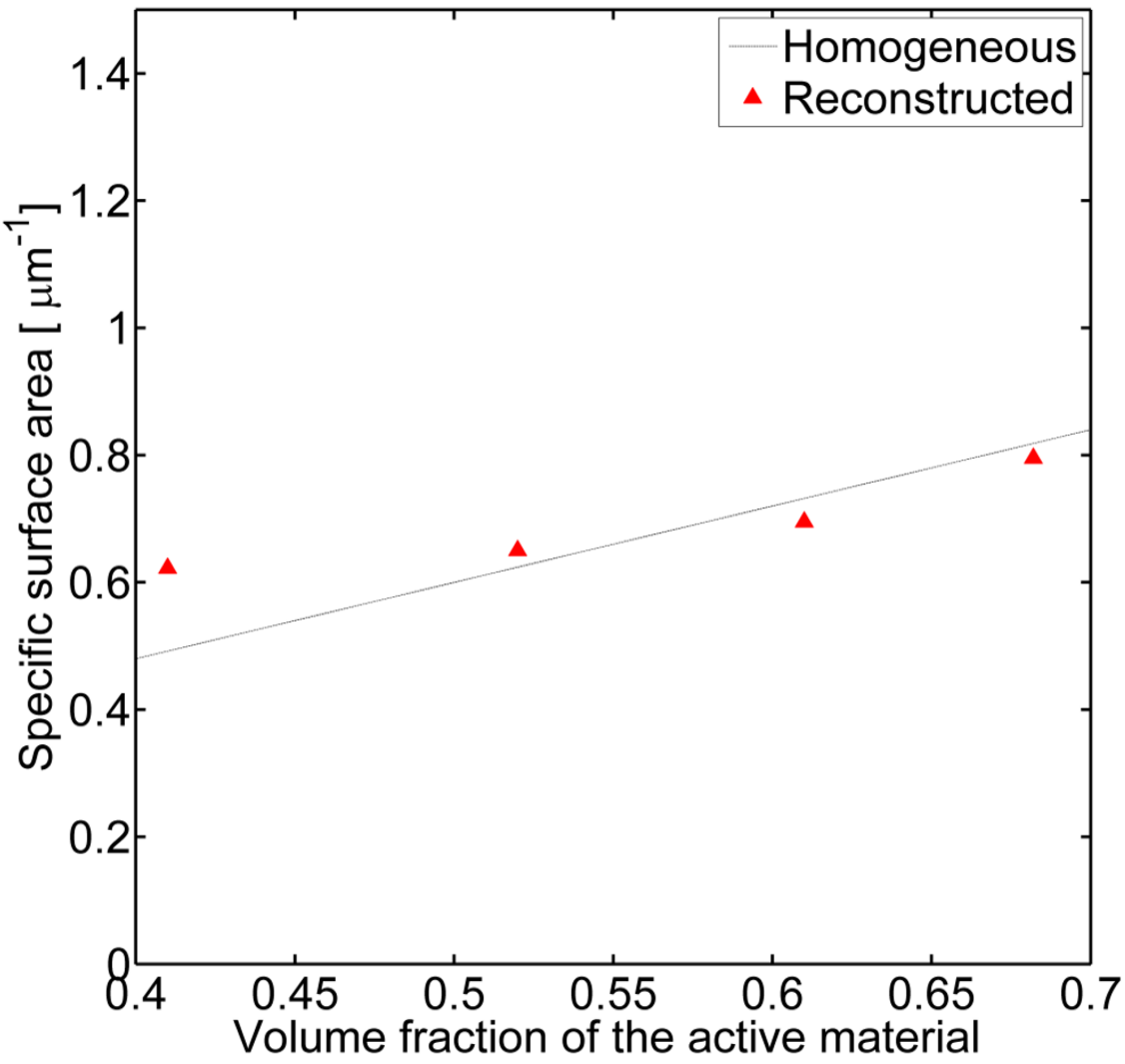

Fig. 3.22. Specific surface area of the reconstructed electrodes and the homogeneous(spherical particle diameter is 5.2um) electrodes with the different volume fraction of the active material.

3.4.5 Tortuosity

Ion transport property in a porous electrode could be quantified by tortuosity (t). Tortuosity has been considered as a function of porosity (e) by Bruggeman relation:

$$t = e^{-0.5}$$

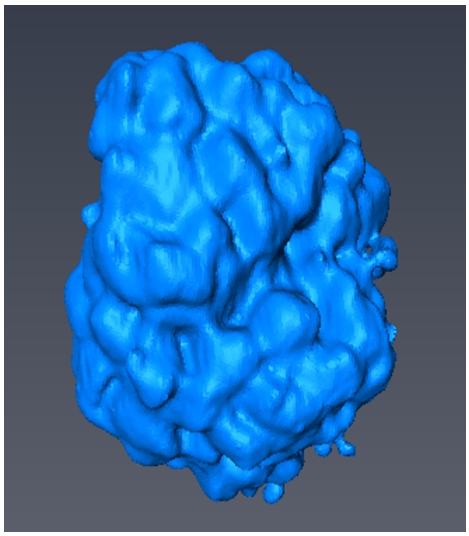

(a) 3D reconstruction of a NMC particle in the electrode with rough surface.

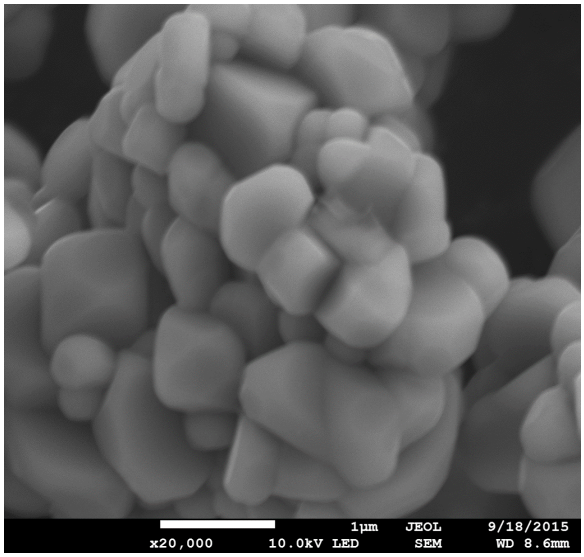

(b) 3.2g/cm3 NMC electrode SEM image.

Fig. 3.23. SEM image of a NMC particle showing rough surface.

However, evidence has indicated that Bruggeman relation underestimates tortuosity in LIB electrode [4, 40]. In this study, tortuosity was calculated from the CT microstructure using the method proposed by Kehrwald et al. [40]. Figure 3.24 shows that the tortuosity is very similar to the experimental results shown by Thorat [41] and much higher than the tortuosity calculated by Bruggeman relation at high NMC densities. At 1.9 g/cm^3 density, the tortuosity is close to the $LiCoO_2$ result [4], but it is still higher than Bruggeman relation. It should be noted that the tortuosity is underestimated by neglecting carbon and binder effects in this study. The larger tortuosity is mainly due to the highly irregular shape and the wide size distribution of NMC particles. It is severe at high NMC densities because of the crushing of NMC particles.

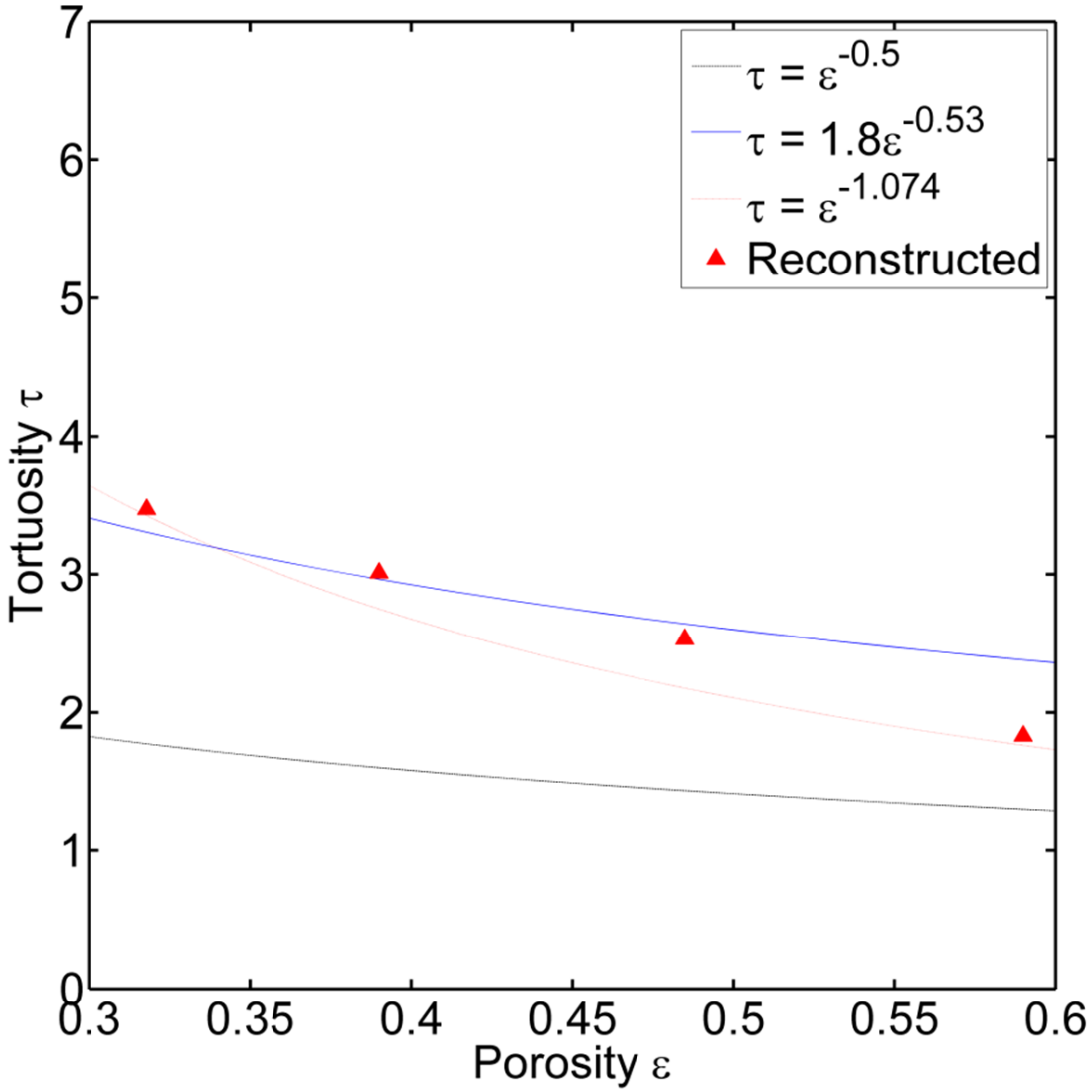

Fig. 3.24. Tortuosity of the reconstructed electrodes compared with the Bruggeman relation and previously reported experimental results ($t = 1.8e^{-0.53}$) and ($t = e^{-1.074}$).

4. SOLID ELECTROLYTE GEOMETRIC CHARACTERISTICS STUDY

4.1 Preface

Plenty of attention was put in the research and manufacture in replacement of the commercial liquid electrolytes batteries on the way to get sable, safe and high performing lithium ion batteries. Hybrid, polymer and solid inorganic electrolytes have gained a lot of attention to replace the conventional organic electrolyte materials. Glass and ceramic electrolytes among this category are studied by more and more organizations and researchers. Cell design, synthesis techniques, manufacturing methods are being studies and reported.

4.2 Solid Electrolyte Introduction

The Solid-state batteries has advantages summary as following: non-flammable, avoid leaking, high ion conductivities, long shelf life, no gassing high energy density, broad operating conditions (-40 to 170 centigrade for Li anodes and more than 300 centigrade for other anodes) ,high volumetric energy density, shock and vibration-resistant [42, 43].

However, the solid state batteries also have a lot of challenges such as low current drain, low capacity, low power density and limit cycle life. The main problem is the low conductivity of various inorganic solid electrolytes ranging between 10-4 to 10-8 S/cm at room temperatures. Besides that, the interface between electrode and electrolyte is a critical problem. Different from liquid electrolyte, solid electrolyte do not have a good liquidity which makes it impossible to adapt the space between electrodes automatically. Although the significantly high conductive at room temperature (10^{-3}

S/cm) of the glass ceramic electrolytes could make up some of the contact issue, the contact resistance between electrode and electrolyte is still very high. The challenge makes the manufacture process of the electrolyte-electrode mix very important and also hinders the use of solid electrolyte in commercial use. Hence, the adhesion situation between solid electrolyte and electrode need to be well studied.

Besides the initial electrode-electrolyte connection situation, the solid electrode volume expansion during the intercalation/de-intercalation of lithium ions is another factor to affect the connection surface situation, which directly influence the performance of solid state LIBs.

4.2.1 Solid Polymer Electrolytes

The solid polymer electrolytes (SPEs) are generated by dissolving a lithium salt (LiX) into a solid polymer matrix. The polymer substrate includes polyacrylonitrile (PAN), polyethylene oxide (PEO), poly(vinyl chloride) (PVC), poly(methyl methacrylate) (PMMA), and poly(phenylene oxide) (PPO), etc. PEO-LiX-based electrolytes are the most widely investigated solid electrolyte system [44].

PEO is a polyether compound that is widely used in industrial manufacturing processes and its chemical formula is $C_{2n}H_{4n+2}O_{n+2}$. Figure 4.1 shown the chemical structure of PEO. Generally, PEO refers to polymers with a molecular mass above 20,000g/mol and PEG (polyethylene glycol) refers to polymers with a molecular mass below 20,000 g/mol. Parker and Wright discovered the ionic conduction of PEO ionic conductivity in alkali metal salt complexes in 1973 [45]. After that, multiple polymer electrolyte have been investigated, involving a variety of transportation ions, e.g., H^+, Li^+, Na^+, K^+, Ag^+, etc. [46].

Dr. Wright et al. investigated the variation of the ionic conductivity with temperature in 1975 [47]. Armand et al. point out the potential use of these materials in lithium batteries area in 1994 [48]. In the meantime, various lithium salts have been studied including Li_2SO_4, $LiNO_3$, $LiAsF_6$, $LiClO_4$, $LiCF_3SO_3$, $LiPF_6$, $LiBF_4$,

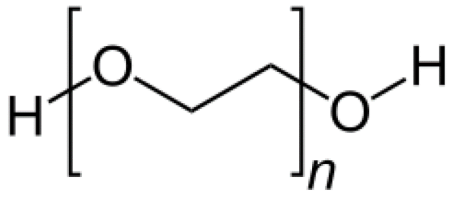

Fig. 4.1. Molecular structure of PEO

LiBOB, $LiN(CF_3SO_2)_2$ (or LiTFSI) and LiDMSI, etc. Chemical properties which are important for lithium battery are investigated. The properties are including conductivity, thermal stability, moisture tolerance, safety and etc. To summarize, the ionic conductivity is related to the segmental motion and local relaxation of the polymer chains and the ionic conductivity need to be improved to meet the requirements of SPEs. Therefore, a large amount of study have been done to improve the ionic conductivity and also other physiochemical properties. At mean time lots of research has been carried out so far.

4.2.2 Inorganic Electrolytes

Inorganic electrolytes include ceramic and glass-ceramic electrolytes. The main differences between them is the extent of their crystallization. Ceramic materials have a high crystallinity, while glass-ceramics have more than one crystalline phase and have an amorphous phase region. Compared to SPEs, GPEs and CPEs, most ceramic and glass-ceramic solid electrolytes have a higher mechanical strength which could prevent dendrite formation. And same as SPEs, with the increasing of temperature, the ionic conductivity of a ceramic solid electrolyte increased. Ceramics are more suitable than liquid for high temperatures or other aggressive environments because of its incombustibility. The most common ceramic electrolytes including NASICON-type (e.g., $Li_{1+x}Ti_{2-x}M_x(PO_4)_3$ (M=Al, Ga, In, Sc)), garnet-type (e.g., $Li_5La_3M_2O_{12}$ (M

= Al, Ga, In, Sc), $Li_3Ln_3Te_2O_{12}$ (Ln = Y, Pr, Nd, Sm and Lu), $Li_6ALa_2Ta_2O_{12}$(A= Sr, Ba), and etc.), and LISICON-type (e.g., Li_2S-Li_2O-P_2S_5) [49–51] etc.

Monchak etc. found that the lithium conduction can be enhanced by partial substitution of tetravalent cations (Ti^{4+}) by trivalent ones (Al^{3+} , Fe^{3+}, Y^{3+}, etc.) [52]. Arbi ect. investigated the compound family with general formula $Li_{1+x}Ti_{2-x}M_x(PO_4)_3$ (M = Al, Ga, In, Sc) [53].

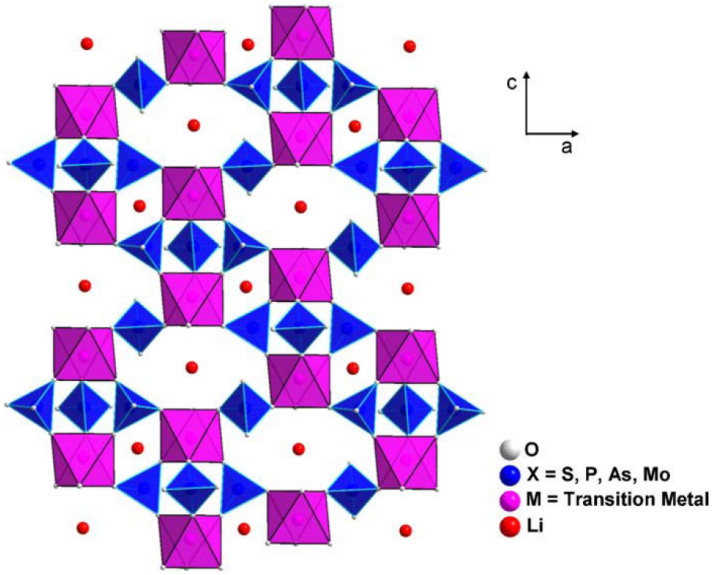

Fig. 4.2. Crystal structure of $Li_{1.3}Ti_{1.7}Al_{0.3}(PO_4)_3$ materials [54].

In the family of the NASICON-type solid electrolyte, $Li_{1+x}Al_xTi_{1-2x}(PO_4)_3$ has recently been widely investigated. It has high ionic conductivity, high electrochemical stability window, and stability in air and water [55, 56]. When x=0.3, the composition $Li_{1.3}Al_{0.3}Ti_{1.7}(PO_4)_3$ was reported to have the highest Li ionic conductivity [49]. Figure 2 to 3 is the crystal structure of $Li_{1.3}Ti_{1.7}Al_{0.3}(PO_4)_3$ materials.

Plenty of research have down on LTAP material, for example the different element ratio [55], the synthesis route [58–61], and the microstructure [62], etc. All these study are related with one important characteristic, conductivity. Get rid of the advantages compared with other solid electrolyte, LTAP is unstable with Li metal due to facile

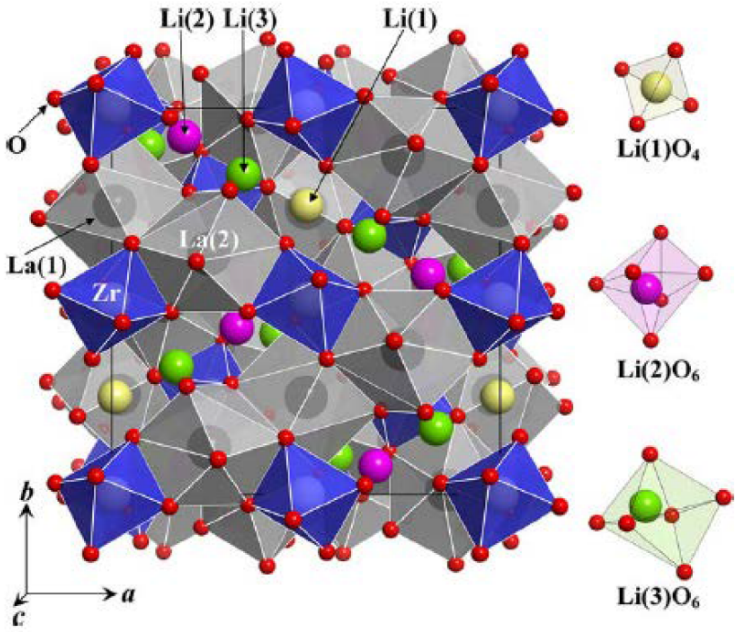

Fig. 4.3. Crystal structure of tetragonal $Li_7La_3Zr_2O_{12}$ [57].

Ti^{4+} reduction [63]. Therefore, recently a Ti^{4+} free NASICON ceramic electrolyte attract a lot attention [64–68].

LLZO, a garnet-like structured solid electrolyte material is also researched as a potential candidate for LIBs. It has a high Li ionic conductivity (bigger than 10^{-4} S cm^{-1} at room temperature) and stability versus lithium anode [63, 69, 70]. Kotobukis etc. works shown that there is no visual and XRD pattern change when LLZO pellets come in contact with molten Li metal for 72 hours [63].

Inaguma is the first one who synthesized perovskite $La_{0.5}1Li_{0.34}TiO_{2.9}$ [72]. It has potential to make bulky type or thin-film solid electrode for lithium ion batteries. It has remarkable bulk conductivity and compatibility with cathode materials [71, 73–75]. However, it has a relatively low grain-boundary resistance. The lithium sulfide electrolytes seem to have higher conductivity (-10^{-3} S cm^{-1})compared with other type of electrolyte. Their drawback is that they are unstable when in contact with moisture or oxygen [76].

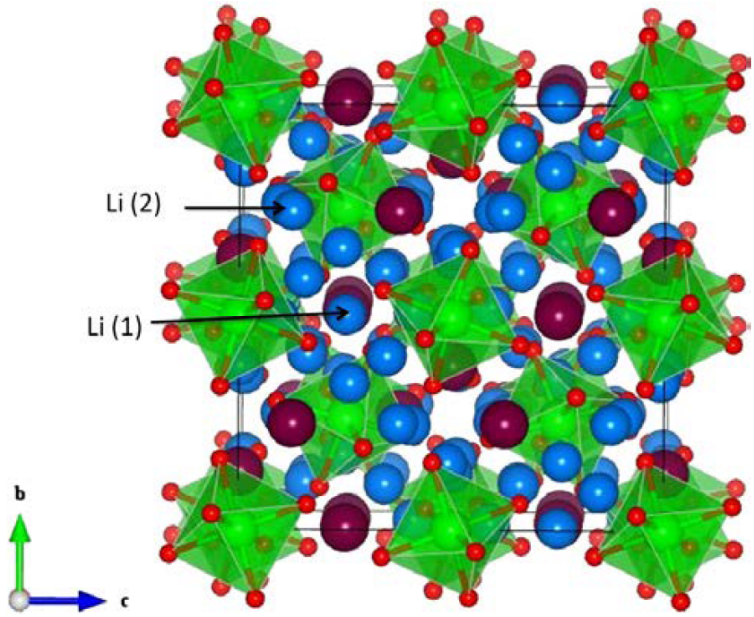

Fig. 4.4. Crystal structure of cubic $Li_7La_3Zr_2O_{12}$ (Blue balls represents Li, purple balls Zr, green balls La, red balls oxygen atoms) [65]

4.2.3 Gel-type Polymer Electrolyte

Ggel-type polymer electrolytes (GPEs), also known as plasticized polymer electrolytes, are made by impregnating liquid electrolyte plasticizer and lithium salt into polymeric host materials. There are several type of liquid electrolyte plasticizer, such as propylene carbonate (PC), ethylene carbonate (EC), diethyl carbonate (DEC) and polyethylene glycol (PEG). This type of solid electrolyte has an ionic conductivity comparable to a liquid electrolyte at room temperature. Generally, GPEs research is based on poly (vinilidene fluoride) (PVDF) [77], PMMA [78, 79], PVC [80], PVDF-HFP (vinylidene fluorideco-hexafluoropropylene) [81], PAN/PEGDA/PVP [82], and PVS [83]. The conductivity of GPEs are effected by multi-factor, such as the type and percentage of lithium salt [84–86], host polymer materials type, solvent type and amount [87, 88].

Among the GPEs family, PVDF-HFP had caught attention of researches due to its remarkable comprehensive properties. The good side of this material is that it not only

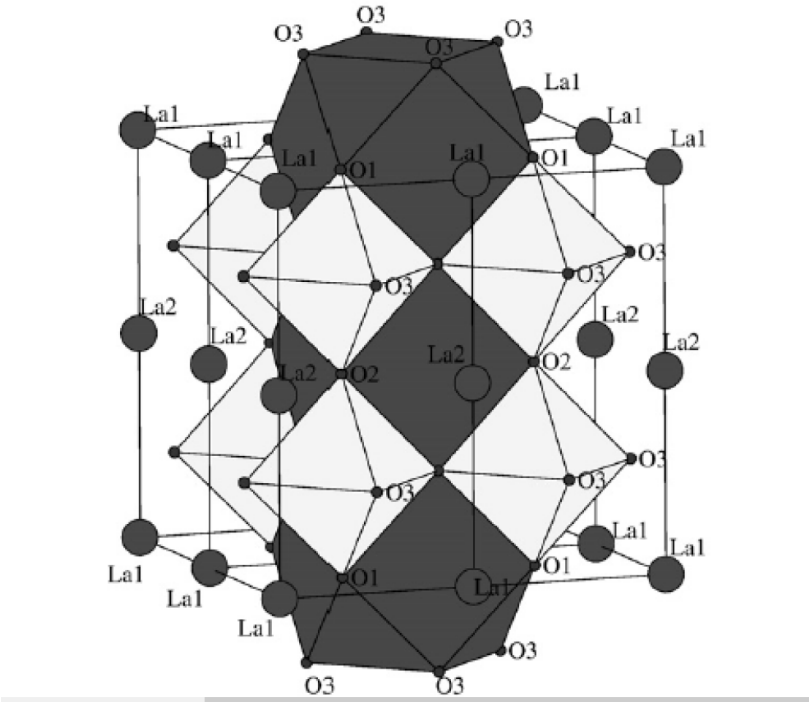

Fig. 4.5. Crystal structure of tetragonal Li $_{3}$xLa $_{2/3\text{-x}}$TiO $_{3}$ [71].

has great ionization of salt, liquid electrolyte entrapping abilities, a lower crystallinity and glass transition temperature, but also have good mechanical strength and high solubility [77, 89, 90]. The deficiency of PVDF-HFP is that its not stable enough over time. Thats caused by liquid leaching from the membrane with time passed and LiF forming due to the reaction between fluorinated polymers and lithium [91].

4.3 Three-phase Porous Solid-state LIB Fabricate and Experiment.

The LTAP electrolyte was manufactured by referring papers published by Dr. Hiromichi Aono etc. [92] and Dr. Kim [93]. First, Lithium carbonate (Li_2CO_3), Aluminum oxide (Al_2O_3), Titanium dioxide (TiO_2), and Ammonium dihydrogen phosphate $(NH_4)_2H_2PO_4$ that were ground and heated in a platinum crucible at 1652 Fahrenheit for 2h. Then ball milled the powder for another 6h and re-heated at the same conditions. Then put into ball milling to mill for 12h to obtain the final

LTAP powder. The last step was dried the powder at 120 degree centigrade for 24h to remove water molecules [42, 92]. Then we made the three phase electrode from a 47:47:6 (wt %) mixture of NMC as active material, $Li_{1.3}Ti_{1.7}Al_{0.3}(PO_4)_3$ as Li-ion conductor (LTAP), and Super P carbon as electron conductor [43]. The electrode was pressured under two conditions: 700psi and 1300psi. We also made a LTAP only solid electrolyte used for reference.

Nano-CT at ANL was also used to get X-ray CT image of the three phase electrolyte-electrode block.The experiment parameter were set as 8kev energy level with a 60nm of spatial resolution and five seconds expose for three different electrolyte-electrode block.

4.4 Image Processing

Image processing used in this chapter is similar with NMC image process. ImageJ was used to remove system errors of the projection images based on flat field images. Tomopy and cuda was used to remove noise and transform the projection image dataset into 3D reconstruction data (image stack). Normalize, remove stripe, median filter and down sample method was used to remove noise with python code. The reconstructed images for 700pis and 1300psi are shown from figure 4.6 to 4.7.

Different from NMC electrode image, LTAP-NMC block have three phase to distinguish. In the CT images of LTAP-NMC electrode, the white phase is NMC, gray phase is LTAP and black phase representative space, PVDF and super carbon.Then two step Otsu threshold code is used to separate and generate the binary image of three phase electrolyte-electrode method. Multiple threshold method is not used, because LTAP phase and space phase(with PVDF and C include) have close pixel value, which make the result not accurate. The histogram information of a sample CT reconstruction image (formate .tiff) is shown in figure 4.8. The X axis is pixel value, y axis is pixel number. We could find one small peak when X smaller than

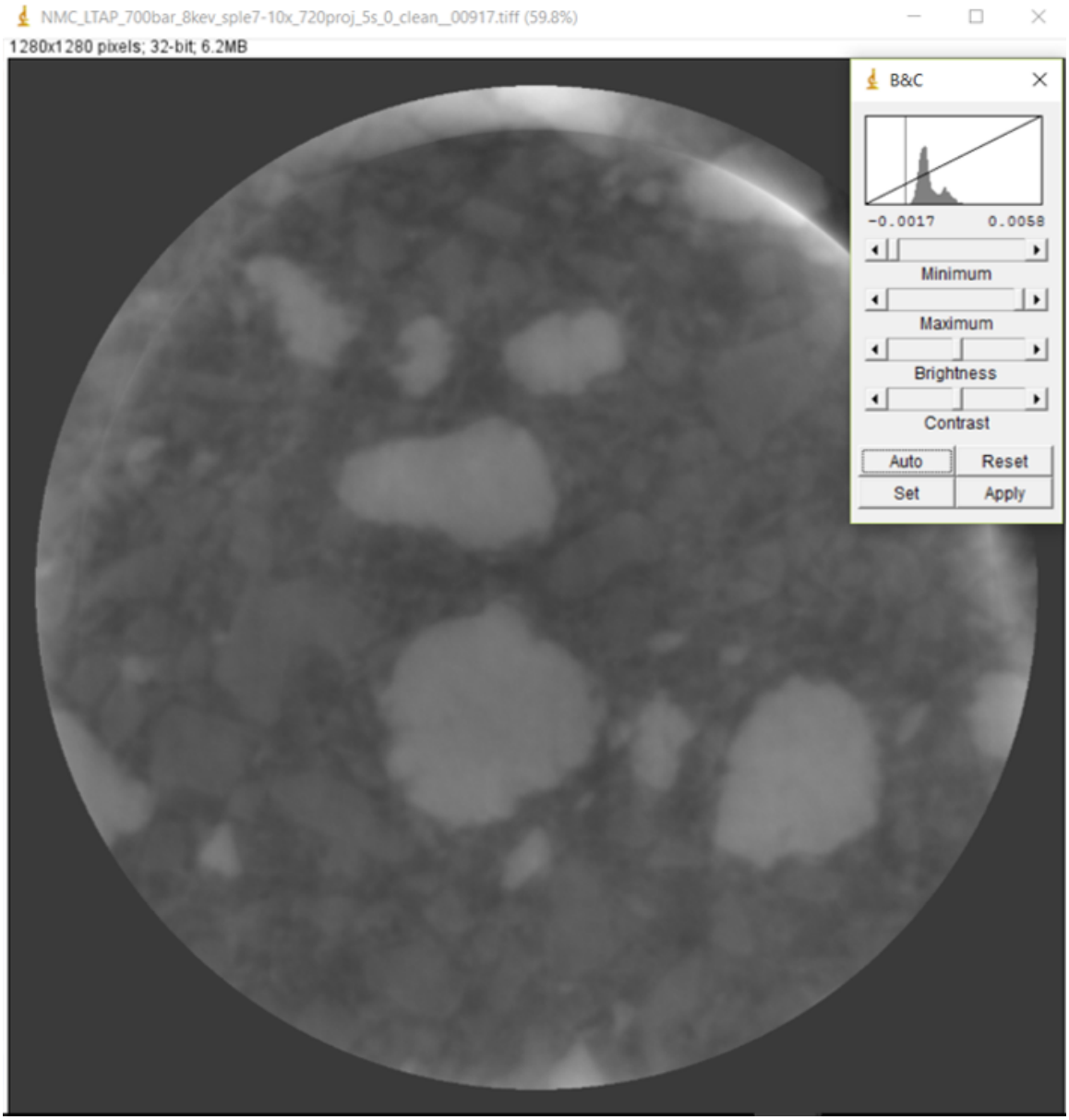

Fig. 4.6. X-ray CT reconstruct 700psi 8kev.

zero and two clear peak when X bigger than zero. They represent space, LTAP and NMC respectively.

It is obvious that there is a gradient area between the white and black phase, which could be distinguished as gray phase. This may cause a gray phase shape error, white

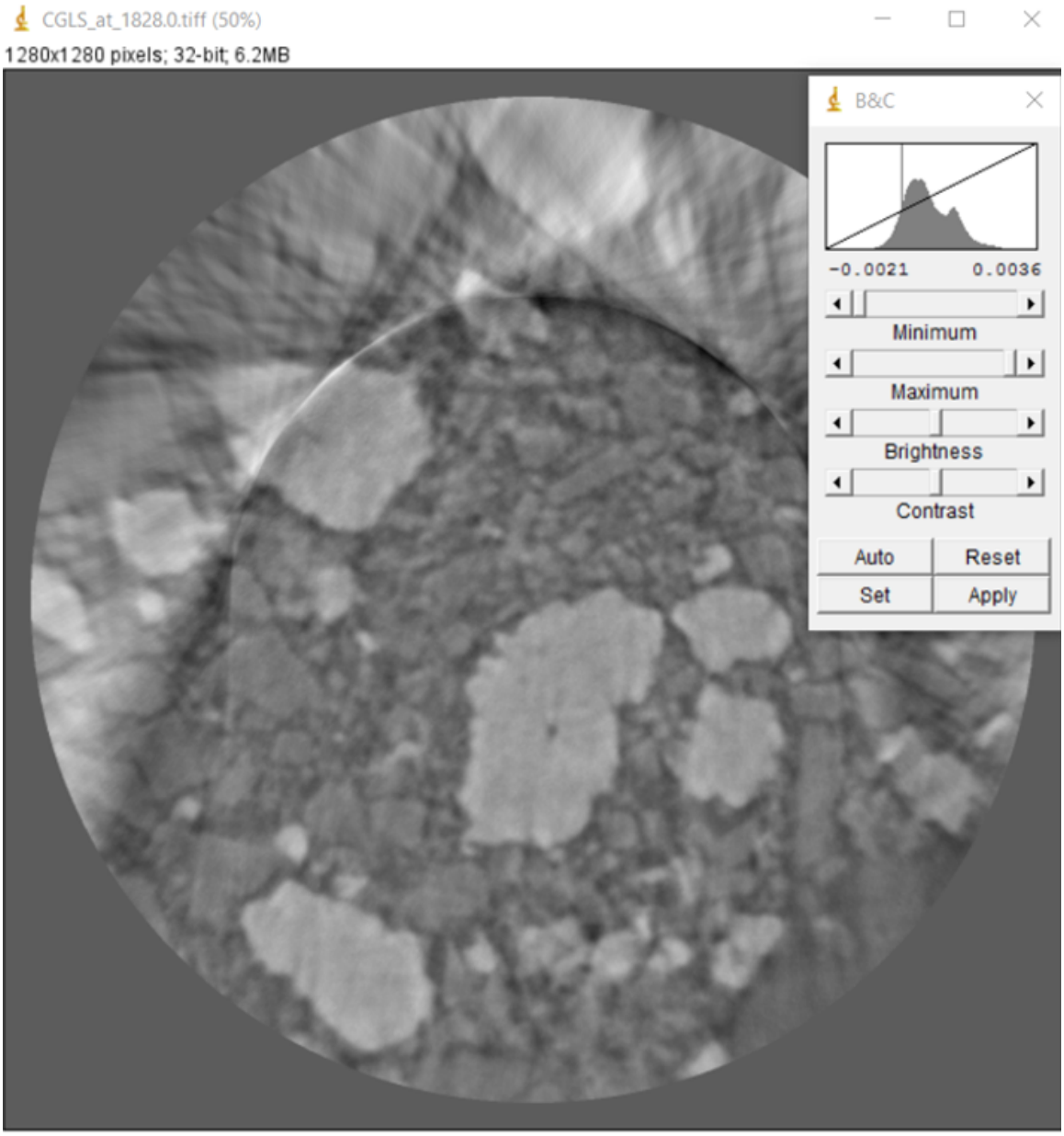

Fig. 4.7. X-ray CT reconstruct 1300psi 8kev.

and black phase shrink. Therefore, dilation code is used to grown NMC particles for a few pixels without change their outlines. The NMC particles size is inspected by comparing to the original CT reconstructed images to make sure the dilation is appropriate. A sample images and their dilation results are shown in figure 4.9.

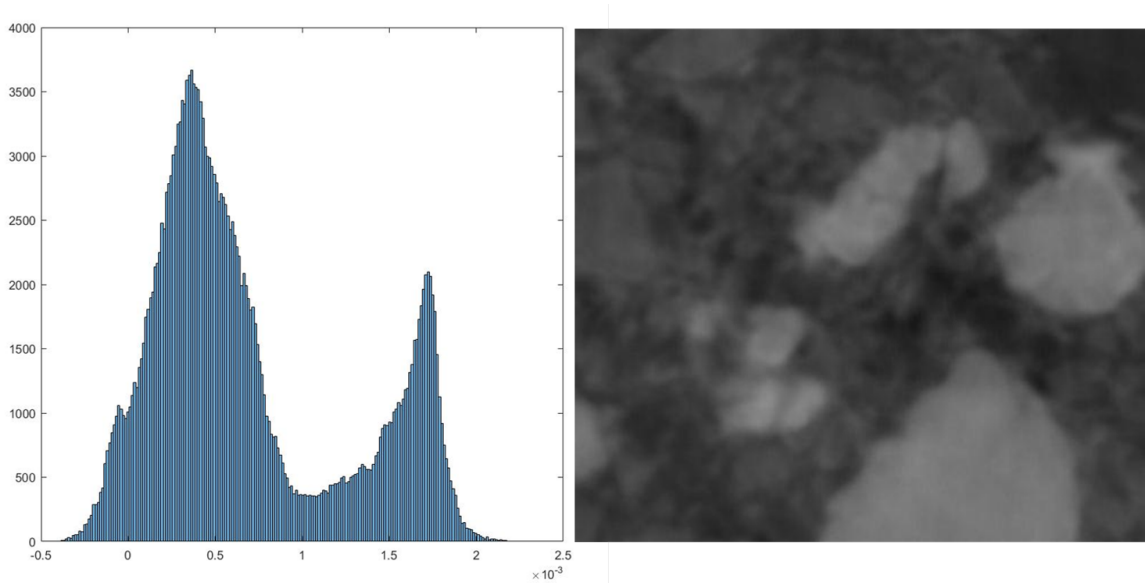

Fig. 4.8. Sample CT reconstruction image histograme with X axis represent pixel value, Y axis represent pixel number.

Figure 4.9 a) shows the original cropped CT image generated from imageJ. Figure b) and d) shows the binary NMC particle morphology before and after dilation. Figure c) shows the grown part of NMC particles from b) to d).

Figure 4.10 shows 3D reconstruction of LTAP-NMC electrode generated form Avizo. Green color shows the NMC particles and the red phase shows LTAP. Besides green and red are space and carbon phase.

4.5 3D Solid Electrolyte Analysis

As shown in the figure 4.6 and figure 4.7, the sample CT reconstructed LTAP-NMC images get from 8kev X-ray energy level could clear shown two peaks, they are represent white phase and gray phase respectively. Theory, there should show three peaks for three phase materials. It's clearly that the black phase have a very low ratio due to the high pressure during the electrode-electrolyte manufacture process. While according to the histogram figure 4.8, we could find the third small peak. Even

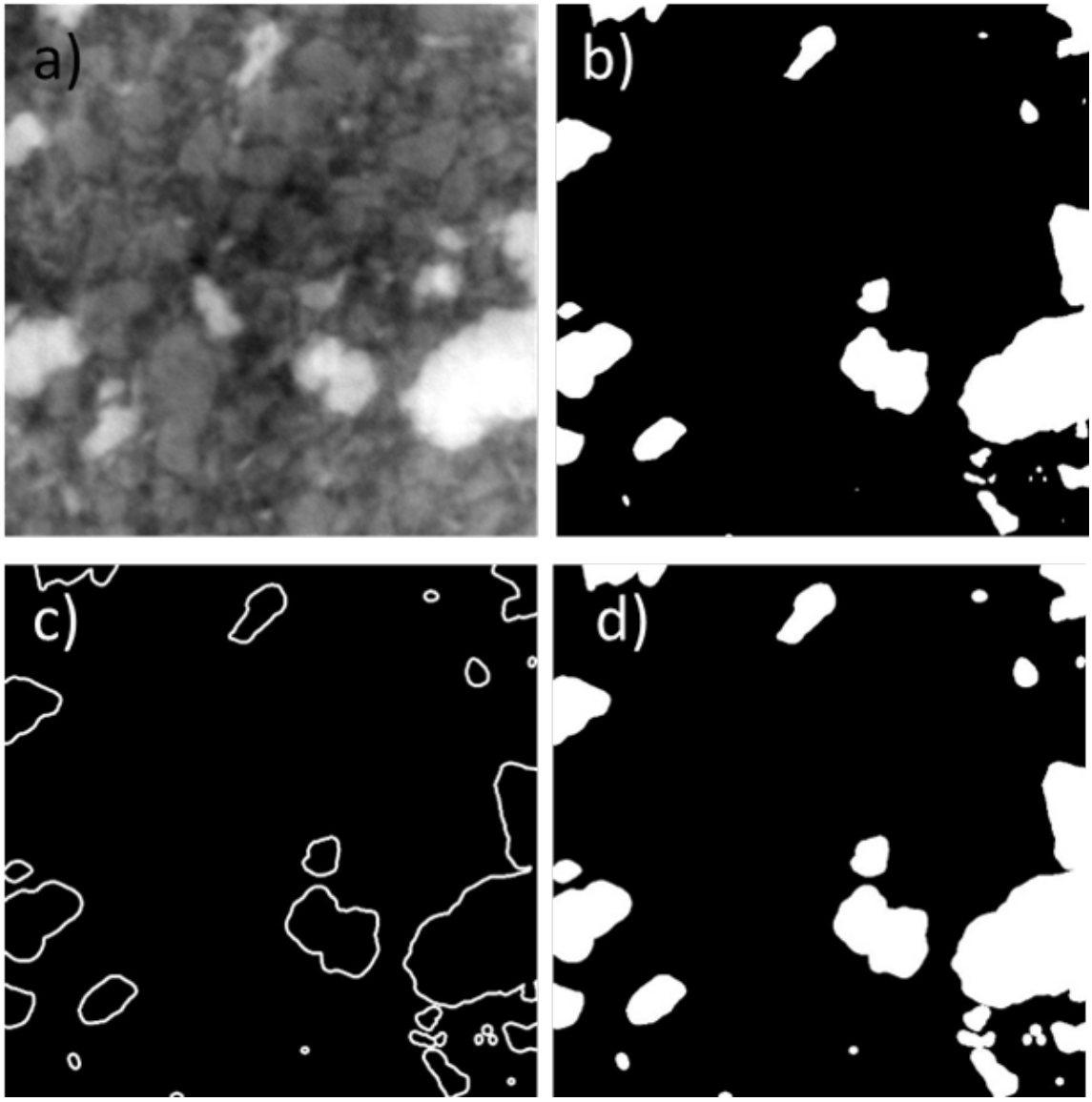

Fig. 4.9. Binary and dilation used for NMC particles.

though, the Otsu threshold method and dilation used in MATLAB could help us to distinguish the black phase from the gray phase, as shown in figure 4.9. That's means, we could use one X-ray energy level to distinguish both activity material and solid electrolyte phase in a battery. This method will provide a new train of thought used for solid electrolyte research, for example, in situ solid electrolyte battery testing.

To compare the 3D geometry of LTAP-NMC electrode with LTAP only electrode, X-ray CT reconstruction sample image of LTAP electrode is shown in figure 4.11. Figure 4.12 is SEM image of LTAP solid electrolyte (pressed under 1300psi). SEM image shows that LTAP particles have irregular shape and have size smaller than 2um. Whats more, the LTAP particles are not well connected to each other and clear space are shown between particles. While in the X-ray CT image, we could tell the irregular shape of LTAP particles, but we could not get clear gap between particles. That is because the resolution of the X-ray CT is 0.0582um, which is not as high as SEM. Besides that, the resolution also limit the detail analysis of the 3D reconstructed electrode data.

In the end of the image processing, crop size of the LTAP-NMC reconstruct CT data are 25um. As illustrated in previous chapter, the reconstruction data size is big enough for further geometric analysis. It is necessary to note that based on the inavoidable error produce during electrode fabricating, X-ray CT experiment and image processing, the following geometric analysis could have some error.

Contact area percentage between NMC active material and LTAP solid electrode is calculated by contact area/NMC electrode surface area. The contact area percentage results for 700pis and 1300psi are 55% and 59% respectively. The results show that the higher pressure applied on the sample, the bigger contact area percentage between the active material and solid electrolyte. Meanwhile, the result shows that even high pressures as 700psi and 1300psi are applied to fabricate the none-binder NMC-LTAP electrode, the connection between active material and solid electrolyte still have a high room to improve.

The transport of charge carriers, which is one of the most important parameter influence battery performance, is limited by ionic diffusion and electron mobility in many LIB electrode. Electron mobility is relay on the electron transport through carbon inside the electrode. We have add 6% of carbon in LTAP-NMC electrode. It is much higher than three percentage carbon in NMC electrode we tested in previous chapter. So we assume that the short slab that made the LTAP-NMC electrode not

working is the ionic diffusion in our condition. Three parameters, tortuosity, diffusion length and effective diffusivity, have a significant influence to the transport of ionic. So we calculated them from 3D meshed data generated from MATLAB as illustrated in previous chapter and the results are shown in table 4.1. LTAP solid electrolyte, 1300psi LTAP-NMC electrode have tortuosity as 2.3 and 4.6; diffusion length as 30.2um and 32.8um; effective diffusivity as 1.08×10^{-3}um^2/s and 3.04×10^{-4}um^2/s.

Table 4.1.
LTAP-NMC solid electrolyte-electrode geometric analyze results.

	diffusion length (um)	effective diffusivity (um^2/s)	tortuosity
LTAP Only	30.20	1.08×10^{-3}	2.28
LTAP –NMC 1300psi	32.80	3.04×10^{-4}	4.60

Table 4.2.
Material volume percentage calculated from CT reconstruct data.

Data Set	Contact area/NMC surface area	Contact area/total NMC volume($1/um$)	NMC	LTAP	SPACE + C
700 psi	55%	0.530	28%	45%	27%
1300 psi	59%	0.622	31%	51%	18%

The material volume percentage of both 700psi and 1300pis, 8kev electrode-electrolyte are calculated. The results are shown in table 4.2. It clearly shows that the 1300 psi have lower space percentage than 700psi. However, the space percentage is 46.52% and 33.31% including PVDF, C and space, which do not have ability to conductive ion.

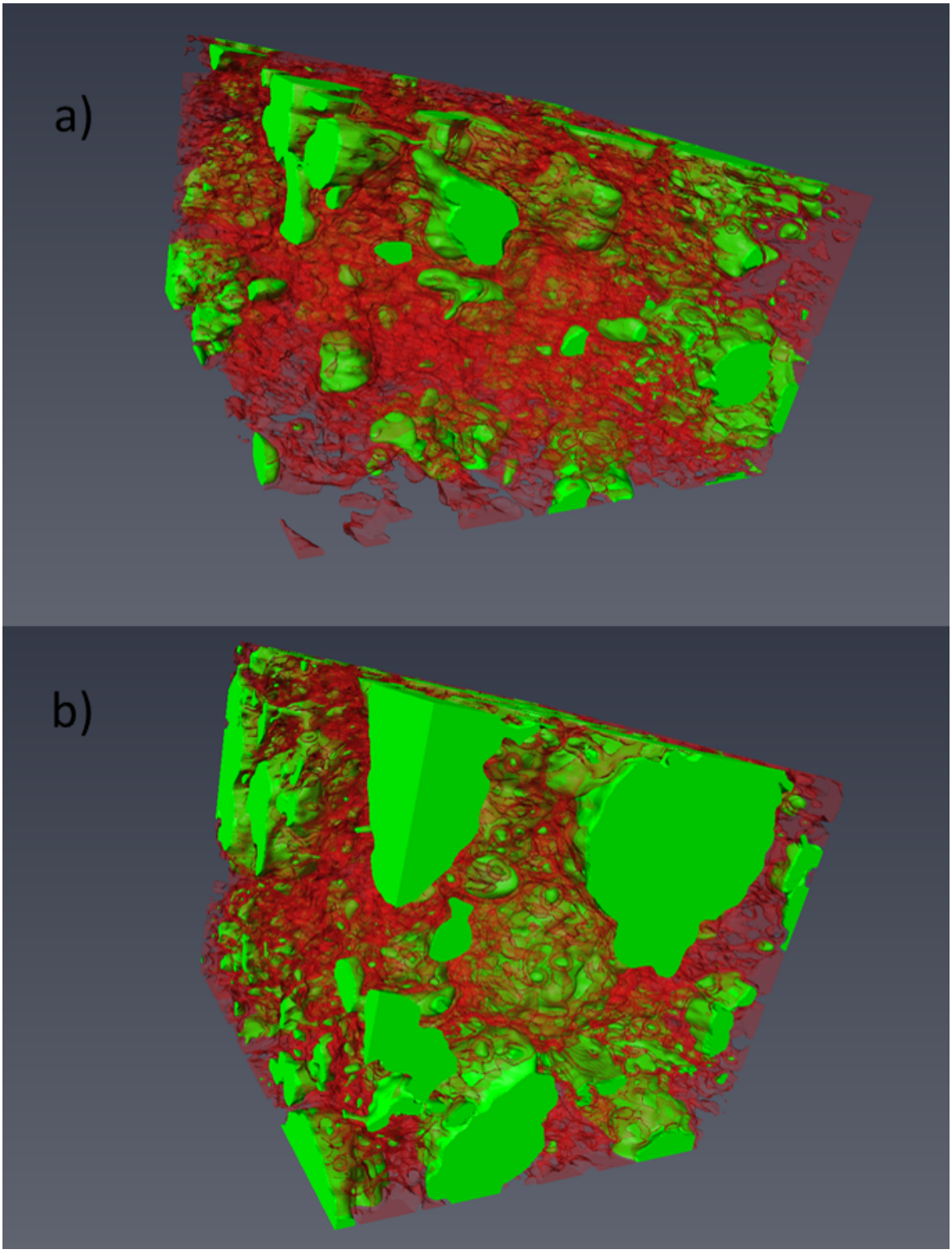

Fig. 4.10. 3D reconstruction of LTAP-NMC electrode generated form Avizo.

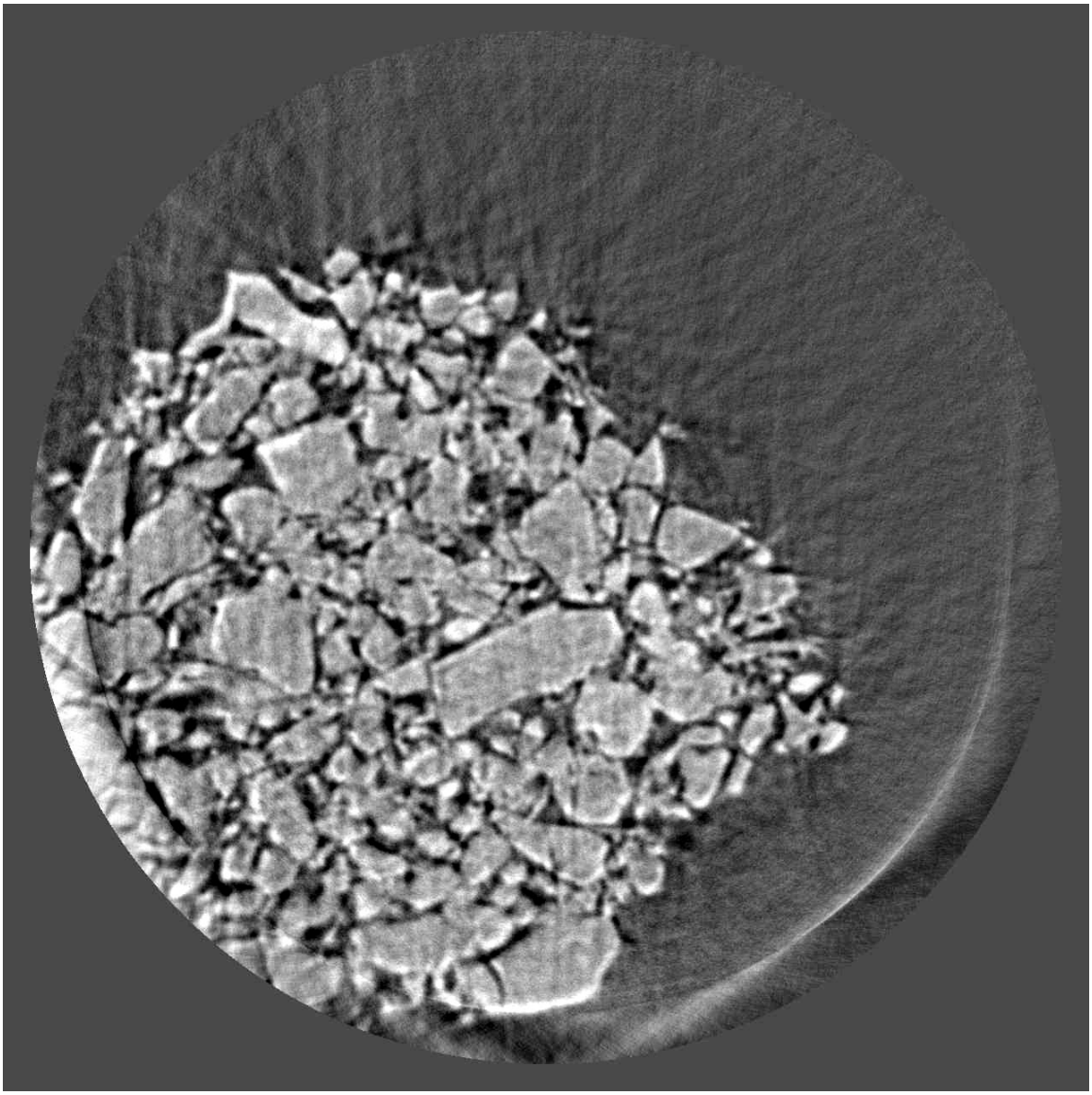

Fig. 4.11. X-ray CT reconstruction sample image of LTAP solid electrolyte.

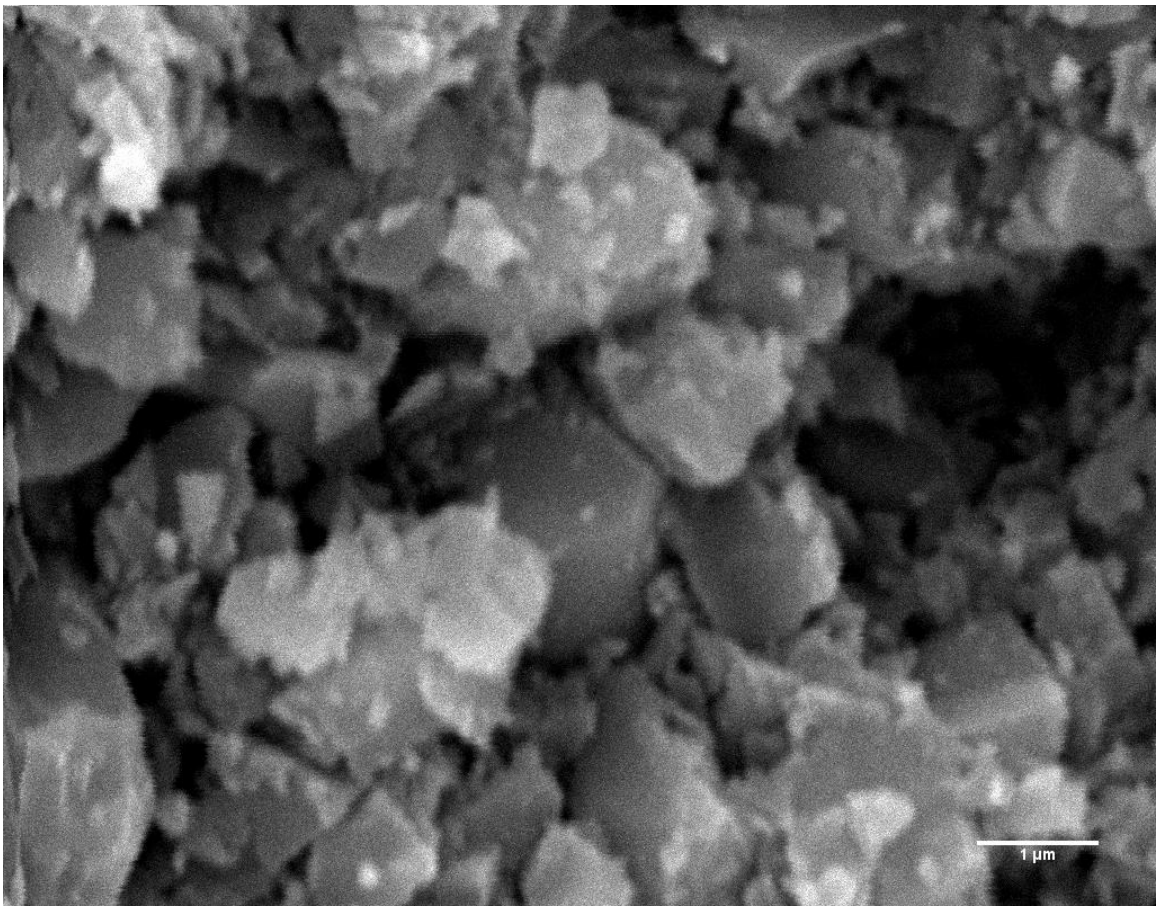

Fig. 4.12. SEM image of LTAP solid electrolyte.

5. SUMMARY

Geometric and electrochemical characteristics of different calendering condition NMC cathode material and geometric characteristics of all solid LTAP-NMC mix electrode was studied in the thesis.

The second and third chapter focus on NMC cathode electrodes correlation between the geometric characteristics and electrochemical performance with different calendering conditions. Electrochemical performance is studied in chapter two by charging/discharging four different packing density electrodes under different C rate and by doing EIS experiments. In chapter three, the 3D microstructure of NMC electrode was obtained by using the synchrotron TXM tomography with voxel size of $58.2 \times 58.2 \times 58.2$ nm^3 at beamline 32-ID-C at the APS of ANL. X-ray CT reconstruction method is illustrated. Python based Tomopy and ASTRA toolbox are used to filter the original HDF5 data and reconstruction. ImageJ is used to help remove noise, adjust contrast and cropping. Iso2mesh and image processing tool box are used in MATLAB to generate meshed 3D structure of CT data. The meshed 3D data is used for further analysis such as calculate porosity, tortuosity, specic surface area etc.

The geometric and electrochemical analysis of different NMC electrodes show that more calendering can help to achieve smaller pore size and relatively uniform pore size distribution, thereby increasing the electrochemically active area. However, calendering also can cause crushing of NMC particles and deactivate the internal nanometer-sized particles at high C rates. At high calendering condition, the capacity drops significantly because many NMC particles are crushed. This study shows that the NMC electrode with the NMC density 3.0 g/cm^3 after calendering is the optimum when the weight ratio of NMC:binder:carbon is 94:3:3.

In the forth chapter, solid electrolyte LTAP and active material NMC mixed electrode was manufactured. To study their geometric characteristics, X-ray CT

images were generated for LTAP, 700psi LTAP-NMC and 1300psi LTAP-NMC electrodes. The results shows that by using one X-ray energy level, we could distinguish both NMC active material and LTAP solid electrolyte at 8kev X-ray energy level.Meanwhile, the result shows that even high pressures as 700psi and 1300psi are applied to fabricate the none-binder NMC-LTAP electrode, the connection between active material and solid electrolyte still have a high room to improve. What's more, the connection of LTAP electrolyte particle have a significant influence on ionic diffusion inside of the battery. Therefore, the geometric parameter such as tortuosity, diffusion length and effective diffusivity are calculated from the reconstruct data to illustrate lithium ion transportation.

REFERENCES

REFERENCES

[1] Linden, David, and Thomas B. Reddy. "Handbook of Batteries." *McGraw-Hill Companies*,(2002) 1e42 4.

[2] Huang, Peifeng, Qingsong Wang, Ke Li, Ping Ping, and Jinhua Sun. "The Combustion Behavior of Large Scale Lithium Titanate Battery." *Scientific Reports*, 5 (2015): 7788.

[3] Lowe, Marcy, Saori Tokuoka, Tali Trigg, and Gary Gereffi. "Lithium-ion Batteries for Electric Vehicles." *Center of Glob.* (2010).

[4] Lim, Cheolwoong, Bo Yan, Leilei Yin, and Likun Zhu. "Geometric Characteristics of Three Dimensional Reconstructed Anode Electrodes of Lithium Ion Batteries." *Energies* 7, no. 4 (2014): 2558-2572.

[5] Smekens, Jelle, Rahul Gopalakrishnan, Nils Van den Steen, Noshin Omar, Omar Hegazy, Annick Hubin, and Joeri Van Mierlo. "Influence of Electrode Density on the Performance of Li-ion Batteries: Experimental and Simulation Results." *Energies*, 9, no. 2 (2016): 104.

[6] Zheng, Honghe, Li Tan, Gao Liu, Xiangyun Song, and Vincent S. Battaglia. "Calendering Effects on the Physical and Electrochemical Properties of Li [Ni 1/3 Mn 1/3 Co 1/3] O 2 cathode." *Journal of Power Sources, 208 (2012): 52-57.*,.

[7] van Bommel, Andrew, and Ranjith Divigalpitiya. "Effect of Calendering LiFePO4 Electrodes." *Journal of The Electrochemical Society*, 159, no. 11 (2012): A1791-A1795.

[8] Yang, Gui-Fu, and Seung-Ki Joo. "Calendering Effect on the Electrochemical Performances of the Thick Li-ion Battery Electrodes Using a Three Dimensional Ni Alloy Foam Current Collector." *Electrochimica Acta*, 170 (2015): 263-268.

[9] Liu, Gao, Honghe Zheng, Xiangyun Song, and Vincent S. Battaglia. "Particles and Polymer Binder Interaction: a Controlling Factor in Lithium-Ion Electrode Performance." *Journal of The Electrochemical Society*, 159, no. 3 (2012): A214-A221.

[10] Zheng, Honghe, Gao Liu, Xiangyun Song, Paul Ridgway, Shidi Xun, and Vincent S. Battaglia. "Cathode Performance as a Function of Inactive Material and Void Fractions." *Journal of The Electrochemical Society*, 157, no. 10 (2010): A1060-A1066.

[11] Haselrieder, Wolfgang, Stoyan Ivanov, Daniel Klaus Christen, Henrike Bockholt, and Arno Kwade. "Impact of the Calendering Process on the Interfacial Structure and the related Electrochemical Performance of Secondary Lithium-Ion Batteries." *ECS Transactions*, 50, no. 26 (2013): 59-70.

[12] Marks, Thomas, Simon Trussler, A. J. Smith, Deijun Xiong, and J. R. Dahn. "A Guide to Li-ion Coin-Cell Electrode Making for Academic Researchers." *Journal of The Electrochemical Society*, 158, no. 1 (2011): A51-A57.

[13] Ha, Seonbaek, Vijay K. Ramani, Wenquan Lu, and Jai Prakash. "Optimization of Inactive Material Content in Lithium Iron Phosphate Electrodes for High Power Applications." *Electrochimica Acta*, 191 (2016): 173-182.

[14] Hutzenlaub, Tobias, Simon Thiele, Roland Zengerle, and Christoph Ziegler. "Three-Dimensional Reconstruction of a LiCoO2 Li-ion Battery Cathode." *Electrochemical and Solid-State Letters*, 15, no. 3 (2011): A33-A36.

[15] Lim, Cheolwoong, Bo Yan, Leilei Yin, and Likun Zhu. "Geometric Characteristics of Three Dimensional Reconstructed Anode Electrodes of Lithium Ion Batteries." *Energies* 7, no. 4 (2014): 2558-2572.

[16] Fu Yongzhu. "EEN220 Fundamentals of Electrochemical Materials and Energy Engineering, Lecture1", *Purdue School of Technology*, (2015).

[17] Lim, Cheolwoong, Bo Yan, Huixiao Kang, Zhibin Song, Wen Chao Lee, Vincent De Andrade, Francesco De Carlo, Leilei Yin, Youngsik Kim, and Likun Zhu. "Analysis of Geometric and Electrochemical Characteristics of Lithium Cobalt Oxide Electrode with Different Packing Densities." *Journal of Power Sources* 328 (2016): 46-55.

[18] Peng, Lele, Yue Zhu, Umair Khakoo, Dahong Chen, and Guihua Yu. "Self-assembled LiNi 1/3 Co 1/3 Mn 1/3 O 2 Nanosheet Cathodes with Tunable Rate Capability." *Nano Energy* 17 (2015): 36-42.

[19] Ebner, Martin, Felix Geldmacher, Federica Marone, Marco Stampanoni, and Vanessa Wood. "Xray Tomography of Porous, Transition Metal Oxide Based Lithium Ion Battery Electrodes." *Advanced Energy Materials*, 3, no. 7 (2013): 845-850.

[20] Liu, Zhao, J. Scott Cronin, K. Yu-chen, James R. Wilson, Kyle J. Yakal-Kremski, Jun Wang, Katherine T. Faber, and Scott A. Barnett. "Three-dimensional Morphological Measurements of LiCoO 2 and LiCoO 2/Li (Ni 1/3 Mn 1/3 Co 1/3) O 2 Lithium-Ion Battery Cathodes." *Journal of Power Sources*, 227 (2013): 267-274.

[21] Mendoza, Hector, Scott A. Roberts, Victor E. Brunini, and Anne M. Grillet. "Mechanical and Electrochemical Response of a LiCoO 2 Cathode Using Reconstructed Microstructures." *Electrochimica Acta*,190 (2016): 1-15.

[22] Levi, M. D., G. Salitra, B. Markovsky, H. Teller, D. Aurbach, Udo Heider, and Lilia Heider. "SolidState Electrochemical Kinetics of LiIon Intercalation into Li1 x CoO2: Simultaneous Application of Electroanalytical Techniques SSCV, PITT, and EIS." *Journal of The Electrochemical Society*, 146, no. 4 (1999): 1279-1289.

[23] Thomas, M. G. S. R., P. G. Bruce, and J. B. Goodenough. "AC Impedance Analysis of Polycrystalline Insertion Electrodes: Application to Li1 x CoO2." *Journal of the Electrochemical Society*, 132, no. 7 (1985): 1521-1528.

[24] Huang, Jun, Zhe Li, Jianbo Zhang, Shaoling Song, Zhongliang Lou, and Ningning Wu. "An Analytical Three-Scale Impedance Model for Porous Electrode with Agglomerates in Lithium-Ion Batteries." *Journal of The Electrochemical Society*, 162, no. 4 (2015): A585-A595.

[25] Grillet, Anne M., Thomas Humplik, Emily K. Stirrup, Scott A. Roberts, David A. Barringer, Chelsea M. Snyder, Madison R. Janvrin, and Christopher A. Apblett. "Conductivity Degradation of Polyvinylidene Fluoride Composite Binder During Cycling: Measurements and Simulations for Lithium-Ion Batteries." *Journal of The Electrochemical Society*, 163, no. 9 (2016): A1859-A1871.

[26] Shearing, P. R., L. E. Howard, Peter Stanley Jrgensen, N. P. Brandon, and S. J. Harris. "Characterization of the 3-Dimensional Microstructure of a Graphite Negative Electrode from a Li-ion Battery." *Electrochemistry Communications* 12, no. 3 (2010): 374-377.

[27] Thiedmann, Ralf, Ole Stenzel, Aaron Spettl, Paul R. Shearing, Stephen J. Harris, Nigel P. Brandon, and Volker Schmidt. "Stochastic Simulation Model for the 3D Morphology of Composite Materials in Liion Batteries." *Computational Materials Science* 50, no. 12 (2011): 3365-3376.

[28] Lim, Cheolwoong, Bo Yan, Leilei Yin, and Likun Zhu. "Simulation of Diffusion-Induced Stress Using Reconstructed Electrodes Particle Structures Generated By Micro/Nano-CT." *Electrochimica Acta*, 75 (2012): 279-287.

[29] Chen-Wiegart, Yu-chen Karen, Paul Shearing, Qingxi Yuan, Andrei Tkachuk, and Jun Wang. "3D Morphological Evolution of Li-ion Battery Negative Electrode LiVO 2 During Oxidation Using X-Ray Nano-Tomography." *Electrochemistry Communications*, 21 (2012): 58-61.

[30] Chen-Wiegart, Yu-chen Karen, Zhao Liu, Katherine T. Faber, Scott A. Barnett, and Jun Wang. "3D Analysis of a LiCoO 2Li (Ni 1/3 Mn 1/3 Co 1/3) O 2 Li-ion Battery Positive Electrode Using X-ray Nano-Tomography." *Electrochemistry Communications*, 28 (2013): 127-130.

[31] Cooper, S. J., D. S. Eastwood, J. Gelb, G. Damblanc, D. J. L. Brett, R. S. Bradley, P. J. Withers et al. "Image Based Modelling of Microstructural Heterogeneity in LiFePO 4 Electrodes for Li-ion Batteries." *Journal of Power Sources*, 247 (2014): 1033-1039.

[32] Babu, Siddharth Komini, Alexander I. Mohamed, Jay F. Whitacre, and Shawn Litster. "Multiple Imaging Mode X-Ray Computed Tomography for Distinguishing Active and Inactive Phases in Lithium-Ion Battery Cathodes." *Journal of Power Sources*, 283 (2015): 314-319.

[33] Yan, Bo, Cheolwoong Lim, Leilei Yin, and Likun Zhu. "Three Dimensional Simulation of Galvanostatic Discharge of LiCoO2 Cathode Based on X-ray Nano-CT Images." *Journal of The Electrochemical Society*, 159, no. 10 (2012): A1604-A1614.

[34] Yan, Bo, Cheolwoong Lim, Zhibin Song, and Likun Zhu. "Analysis of Polarization in Realistic Li Ion Battery Electrode Microstructure Using Numerical Simulation." *Electrochimica Acta*, 185 (2015): 125-141.

[35] Wilson, James R., J. Scott Cronin, Scott A. Barnett, and Stephen J. Harris. "Measurement of Three-Dimensional Microstructure in a LiCoO2 Positive Electrode." *Journal of Power Sources*, 196, no. 7 (2011): 3443-3447.

[36] Liu, Zhao, J. Scott Cronin, K. Yu-chen, James R. Wilson, Kyle J. Yakal-Kremski, Jun Wang, Katherine T. Faber, and Scott A. Barnett. "Three-dimensional Morphological Measurements of LiCoO 2 and LiCoO 2/Li (Ni 1/3 Mn 1/3 Co 1/3) O 2 Lithium-Ion Battery Cathodes." *Journal of Power Sources*, 227 (2013): 267-274.

[37] Chen-Wiegart, Yu-chen Karen, Zhao Liu, Katherine T. Faber, Scott A. Barnett, and Jun Wang. "3D Analysis of a LiCoO 2Li (Ni 1/3 Mn 1/3 Co 1/3) O 2 Li-ion Battery Positive Electrode Using X-ray Nano-Tomography." *Electrochemistry Communications*, 28 (2013): 127-130.

[38] Fang, Qianqian, and David A. Boas. "Tetrahedral Mesh Generation from Volumetric Binary and Grayscale Images." *In Biomedical Imaging: From Nano to Macro*, 2009. ISBI'09. IEEE International Symposium on, pp. 1142-1145. IEEE, 2009.

[39] Endo, M., T. Maeda, T. Takeda, Y. J. Kim, K. Koshiba, H. Hara, and M. S. Dresselhaus. "Capacitance and Pore-Size Distribution in Aqueous and Nonaqueous Electrolytes Using Various Activated Carbon Electrodes." *Journal of the Electrochemical Society*, 148, no. 8 (2001): A910-A914.

[40] Kehrwald, Dirk, Paul R. Shearing, Nigel P. Brandon, Puneet K. Sinha, and Stephen J. Harris. "Local Tortuosity Inhomogeneities in a Lithium Battery Composite Electrode." *Journal of The Electrochemical Society*, 158, no. 12 (2011): A1393-A1399.

[41] Thorat, Indrajeet V., David E. Stephenson, Nathan A. Zacharias, Karim Zaghib, John N. Harb, and Dean R. Wheeler. "Quantifying Tortuosity in Porous Li-Ion Battery Materials." *Journal of Power Sources*, 188, no. 2 (2009): 592-600.

[42] Penumaka, Rani Vijaya. "Synthesis of Lithium Manganese Phosphate by Controlled Sol-Gel Method and Design of All Solid State Lithium Ion Batteries." *PhD diss., Purdue University*, 2015.

[43] Lim, Cheolwoong, Rani V. Penumaka, Sho Murakami, Zhibin Song, Vincent De Andrade, Francesco De Carlo, Youngsik Kim, and Likun Zhu. "Geometric Characteristics of Three-Phase Porous Microstructures for All Solid-State Lithium Ion Batteries." *In Meeting Abstracts*, no. 2, pp. 545-545. The Electrochemical Society, 2015.

[44] Liu, Wei. "Multilayer Composite Solid Electrolytes For Lithium Ion Batteries." *PhD diss., Syracuse University*, (2016).

[45] Fenton, D. E., J. M. Parker, and P. V. Wright. "Complexes of Alkali Metal Ions with Poly (Ethylene Oxide)." *Polymer*, 14, no. 11 (1973): 589.

[46] Agrawal, R. C., and G. P. Pandey. "Solid Polymer Electrolytes: Materials Designing and All-Solid-State Battery Applications: an Overview." *Journal of Physics D: Applied Physics*, 41, no. 22 (2008): 223001.

[47] Wright, Peter V. "Electrical Conductivity in Ionic Complexes of Poly (Ethylene Oxide)." *Polymer Internationa*,l 7, no. 5 (1975): 319-327.

[48] Armand, Michel. "The History of Polymer Electrolytes." *Solid State Ionics*, 69, no. 3-4 (1994): 309-319.

[49] Knauth, Philippe. "Inorganic Solid Li ion Conductors: An Overview." *Solid State Ionics*, 180, no. 14 (2009): 911-916.

[50] Trevey, James E., Jeremy R. Gilsdorf, Sean W. Miller, and Se-Hee Lee. "Li 2 SLi 2 OP 2 S 5 Solid Electrolyte for All-Solid-State Lithium Batteries." *Solid State Ionics*, 214 (2012): 25-30.

[51] O'Callaghan, Michael P., Danny R. Lynham, Edmund J. Cussen, and George Z. Chen. "Structure and Ionic-Transport Properties of Lithium-Containing Garnets Li3Ln3Te2O12 (Ln= Y, Pr, Nd, Sm Lu)." *Chemistry of Materials*, 18, no. 19 (2006): 4681-4689.

[52] Monchak, Mykhailo, Thomas Hupfer, Anatoliy Senyshyn, Hans Boysen, Dmitry Chernyshov, Thomas Hansen, Karl G. Schell, Ethel C. Bucharsky, Michael J. Hoffmann, and Helmut Ehrenberg. "Lithium Diffusion Pathway in Li1. 3Al0. 3Ti1. 7 (PO4) 3 (LATP) Superionic Conductor." *Inorganic Chemistry*, 55, no. 6 (2016): 2941-2945.

[53] Arbi, K., J. M. Rojo, and J. Sanz. "Lithium Mobility in Titanium Based Nasicon Li 1+ x Ti 2 x Al x (PO 4) 3 and LiTi 2 x Zr x (PO 4) 3 Materials Followed by NMR and Impedance Spectroscopy." *Journal of the European Ceramic Society*, 27, no. 13 (2007): 4215-4218.

[54] Goodenough, John B., and Youngsik Kim. "Challenges for Rechargeable Batteries." *Journal of Power Sources*, 196, no. 16 (2011): 6688-6694.

[55] Velikokhatnyi, Oleg I., Jeffrey P. Maranchi, Il-Seok Kim, Moni K. Datta, and Prashant N. Kumta. "Ceramic Materials for Lithium-Ion Battery Applications." *In Chemical Processing of Ceramics, Second Edition, pp.*, 667-712. CRC Press, 2005.

[56] Jackman, Spencer D., and Raymond A. Cutler. "Stability of NaSICON-type Li 1.3 Al 0.3 Ti 1.7 P 3 O 12 in Aqueous Solutions." *Journal of Power Sources*, 230 (2013): 251-260.

[57] Rosenkiewitz, N., J. Schuhmacher, M. Bockmeyer, and J. Deubener. "Nitrogen-free SolGel Synthesis of Al-substituted Cubic Garnet Li 7 La 3 Zr 2 O 12 (LLZO)." *Journal of Power Sources*, 278 (2015): 104-108.

[58] Kotobuki, Masashi, Masaki Koishi, and Yoshiki Kato. "Preparation of Li1. 5Al0. 5Ti1. 5 (PO4) 3 Solid Electrolyte Via a Co-Precipitation Method." *Ionics*, 19, no. 12 (2013): 1945-1948.

[59] Schroeder, Melanie, Sven Glatthaar, and Joachim R. Binder. "Influence of Spray Granulation on the Properties of Wet Chemically Synthesized Li 1.3 Ti 1.7 Al 0.3 (PO 4) 3 (LATP) Powders." *Solid State Ionics*, 201, no. 1 (2011): 49-53.

[60] Duluard, Sandrine, Aude Paillassa, Laurent Puech, Philippe Vinatier, Viviane Turq, Patrick Rozier, Pascal Lenormand, Pierre-Louis Taberna, Patrice Simon, and Florence Ansart. "Lithium Conducting Solid Electrolyte Li 1.3 Al 0.3 Ti 1.7 (PO 4) 3 Obtained Via Solution Chemistry." *Journal of the European Ceramic Society*, 33, no. 6 (2013): 1145-1153.

[61] Huang, Lezhi, Zhaoyin Wen, Meifen Wu, Xiangwei Wu, Yu Liu, and Xiuyan Wang. "Electrochemical Properties of Li 1.4 Al 0.4 Ti 1.6 (PO 4) 3 Synthesized by a Co-Precipitation Method." *Journal of Power Sources*, 196, no. 16 (2011): 6943-6946.

[62] Jackman, Spencer D., and Raymond A. Cutler. "Effect of Microcracking on Ionic Conductivity in LATP." *Journal of Power Sources*, 218 (2012): 65-72.

[63] Kotobuki, Masashi, Kiyoshi Kanamura, Yosuke Sato, and Toshihiro Yoshida. "Fabrication of All-Solid-State Lithium Battery with Lithium Metal Anode Using Al 2 O 3-added Li 7 La 3 Zr 2 O 12 Solid Electrolyte." *Journal of Power Sources*, 196, no. 18 (2011): 7750-7754.

[64] Jadhav, Harsharaj S., Ramchandra S. Kalubarme, Seong-Yong Jang, Kyu-Nam Jung, Kyoung-Hee Shin, and Chan-Jin Park. "B 2 O 3-added lithium Aluminium Germanium Phosphate Solid Electrolyte for LiO 2 Rechargeable Batteries." *Dalton Transactions*, 43, no. 30 (2014): 11723-11727.

[65] Santosh, K. C., Roberto C. Longo, Ka Xiong, and Kyeongjae Cho. "Point Defects in Garnet-Type Solid Electrolyte (c-Li 7 La 3 Zr 2 O 12) for Li-ion Batteries." *Solid State Ionics*, 261 (2014): 100-105.

[66] Leo, C. J., GV Subba Rao, and B. V. R. Chowdari. "Effect of MgO Addition on the Ionic Conductivity of LiGe 2 (PO 4) 3 Ceramics." *Solid State Ionics*, 159, no. 3 (2003): 357-367.

[67] Mahmoud, Morsi M., Yuantao Cui, Magnus Rohde, Carlos Ziebert, Guido Link, and Hans Juergen Seifert. "Microwave Crystallization of Lithium Aluminum Germanium Phosphate Solid-State Electrolyte." *Materials*, 9, no. 7 (2016): 506.

[68] Yamamoto, Hiroshi, Mitsuharu Tabuchi, Tomonari Takeuchi, Hiroyuki Kageyama, and Osamu Nakamura. "Ionic Conductivity Enhancement in LiGe2 (PO4) 3 Solid Electrolyte." *Journal of Power Sources*, 68, no. 2 (1997): 397-401.

[69] Kotobuki, Masashi, Hirokazu Munakata, Kiyoshi Kanamura, Yosuke Sato, and Toshihiro Yoshida. "Compatibility of Li7La3Zr2O12 Solid Electrolyte to All-Solid-State Battery Using Li Metal Anode." *Journal of the Electrochemical Society*, 157, no. 10 (2010): A1076-A1079.

[70] Jin, Ying, and Paul J. McGinn. "Li 7 La 3 Zr 2 O 12 Electrolyte Stability in Air and Fabrication of a Li/Li 7 La 3 Zr 2 O 12/Cu 0.1 V 2 O 5 Solid-State Battery." *Journal of Power Sources*, 239 (2013): 326-331.

[71] Bohnke, Odile. "The Fast Lithium-Ion Conducting Oxides Li 3x La 2/3 x TiO 3 From Fundamentals to Application." *Solid State Ionics*, 179, no. 1 (2008): 9-15.

[72] Inaguma, Yoshiyuki, Chen Liquan, Mitsuru Itoh, Tetsur Nakamura, Takashi Uchida, Hiromasa Ikuta, and Masataka Wakihara. "High Ionic Conductivity in Lithium Lanthanum Titanate." *Solid State Communications*, 86, no. 10 (1993): 689-693.

[73] Deng, Yuan, Sui-Jun Shang, Ao Mei, Yuan-Hua Lin, Li-Yu Liu, and Ce-Wen Nan. "The Preparation and Conductivity Properties of Li 0.5 La 0.5 TiO 3/inactive Second Phase Composites." *Journal of Alloys and Compounds*, 472, no. 1 (2009): 456-460.

[74] Mei, Ao, Xiao-Liang Wang, Jin-Le Lan, Yu-Chuan Feng, Hong-Xia Geng, Yuan-Hua Lin, and Ce-Wen Nan. "Role of Amorphous Boundary Layer in Enhancing Ionic Conductivity of LithiumLanthanumTitanate Electrolyte." *Electrochimica Acta*, 55, no. 8 (2010): 2958-2963.

[75] Liao, Cheng-Lung, Chung-Han Wen, and Kuan-Zong Fung. "The Stability Between Perovskite La 2/3 x Li 3x 1/3 2x TiO 3 (3x= 0.3) Electrolyte and LiM m O n (M= Mn, Ni and Co) Cathodes." *Journal of Alloys and Compounds*, 432, no. 1 (2007): L22-L25.

[76] Ohtomo, Takamasa, Akitoshi Hayashi, Masahiro Tatsumisago, and Koji Kawamoto. "All-Solid-State Batteries with Li2O-Li2S-P2S5 Glass Electrolytes Synthesized by Two-Step Mechanical Milling." *Journal of Solid State Electrochemistry*, 17, no. 10 (2013): 2551-2557.

[77] Jiang, Z., B. Carroll, and K. M. Abraham. "Studies of Some Poly (Vinylidene Fluoride) Electrolytes." *Electrochimica Acta*, 42, no. 17 (1997): 2667-2677.

[78] Deepa, M., N. Sharma, S. A. Agnihotry, S. Singh, T. Lal, and R. Chandra. "Conductivity and Viscosity of Liquid and Gel Electrolytes based on LiClO 4, LiN (CF 3 SO 2) 2 and PMMA." *Solid State Ionics*, 152 (2002): 253-258.

[79] Kim, Chi S., and Seung M. Oh. "Spectroscopic and Electrochemical Studies of PMMA-based Gel Polymer Electrolytes Modified with Interpenetrating Networks." *Journal of Power Sources*, 109, no. 1 (2002): 98-104.

[80] Passerini, Stefano, Jose Mauricio Rosolen, and Bruno Scrosati. "Plasticized Carbon Electrodes of Interest for Lithium Rocking Chair Batteries." *Journal of Power Sources, 45, no. 3 (1993): 333-341.*,.

[81] Stephan, A. Manuel, Kee Suk Nahm, M. Anbu Kulandainathan, G. Ravi, and J. Wilson. "Poly (Vinylidene Fluoride-Hexafluoropropylene)(PVdF-HFP) Based Composite Electrolytes for Lithium Batteries." *European Polymer Journal*, 42, no. 8 (2006): 1728-1734.

[82] Cao, Jian-Hua, Bao-Ku Zhu, and You-Yi Xu. "Structure and Ionic Conductivity of Porous Polymer Electrolytes Based on PVDF-HFP Copolymer Membranes." *Journal of Membrane Science*, 281, no. 1 (2006): 446-453.

[83] Choe, H. S., J. Giaccai, M. Alamgir, and K. M. Abraham. "Preparation and Characterization of Poly (Vinyl Sulfone)-and Poly (Vinylidene Fluoride)-Based Electrolytes." *Electrochimica Acta*, 40, no. 13-14 (1995): 2289-2293.

[84] Muniyandi, N., N. Kalaiselvi, P. Periyasamy, R. Thirunakaran, S. Gopukumar, T. Premkumar, N. G. Renganathan, and M. Raghavan. "Optimisation of PVdF-based Polymer Electrolytes." *Journal of Power Sources*, 96, no. 1 (2001): 14-19.

[85] Stephan, A. Manuel, S. Gopu Kumar, N. G. Renganathan, and M. Anbu Kulandainathan. "Characterization of Poly (Vinylidene FluorideHexafluoropropylene)(PVdFHFP) Electrolytes Complexed with Different Lithium Salts." *European Polymer Journal*, 41, no. 1 (2005): 15-21.

[86] Deepa, M., N. Sharma, S. A. Agnihotry, R. Chandra, and S. S. Sekhon. "Effect of Mixed Salts on the Properties of Gel Polymeric Electrolytes." *Solid State Ionics*, 148, no. 3 (2002): 451-455.

[87] Xu, Wu, and C. Austen Angell. "Polymer Electrolytes from Plasticized Poly-MOBs and Their Gel Forms." *Electrochimica Acta*, 48, no. 14 (2003): 2029-2035.

[88] Periasamy, P., K. Tatsumi, M. Shikano, T. Fujieda, T. Sakai, Y. Saito, M. Mizuhata, A. Kajinami, and S. Deki. "An Electrochemical Investigation on polyvinylidene Fluoride-Based Gel Polymer Electrolytes." *Solid State Ionics*, 126, no. 3 (1999): 285-292.

[89] Stephan, A. Manuel, and K. S. Nahm. "Review on Composite Polymer Electrolytes for lithium Batteries." *Polymer*, 47, no. 16 (2006): 5952-5964.

[90] Wang, Hongpeng, Haitao Huang, and Stephanie L. Wunder. "Novel Microporous Poly (Vinylidene Fluoride) Blend Electrolytes for LithiumIon Batteries." *Journal of the Electrochemical Society*, 147, no. 8 (2000): 2853-2861.

[91] Ferrari, S., E. Quartarone, P. Mustarelli, A. Magistris, M. Fagnoni, S. Protti, Claudio Gerbaldi, and A. Spinella. "Lithium Ion Conducting PVdF-HFP Composite Gel Electrolytes Based on N-Methoxyethyl-N-Methylpyrrolidinium Bis (Trifluoromethanesulfonyl)-Imide Ionic Liquid." *Journal of Power Sources*, 195, no. 2 (2010): 559-566.

[92] Aono, Hiromichi, Eisuke Sugimoto, Yoshihiko Sadaoka, Nobuhito Imanaka, and Ginya Adachi. "Ionic Conductivity of Solid Electrolytes Based on Lithium Titanium Phosphate." *Journal of the Electrochemical Society*, 137, no. 4 (1990): 1023-1027.

[93] Asl, Nina Mahootcheian, Joshua Keith, Cheolwoong Lim, Likun Zhu, and Youngsik Kim. "Inorganic Solid/Organic Liquid Hybrid Electrolyte for Use in Li-ion Battery." *Electrochimica Acta*, 79 (2012): 8-16.